Multi-Nucleon Pion Absorption on Helium in the Delta Resonance Region

by

Arthur O. Mateos

A.B., Physics
Princeton University
June 1991

Submitted to the Department of Physics
in partial fulfillment of the requirements for the degree of

Doctor of Philosophy

at the

MASSACHUSETTS INSTITUTE OF TECHNOLOGY

September 1995

Signature of Author .....
Department of Physics
July 28, 1995

Certified by .....
Professor Robert P. Redwine
Professor of Physics
Thesis Supervisor

Accepted by .....
Professor George F. Koster
Chairman of the Graduate Committee

Multi-Nucleon Pion Absorption on Helium in the Delta Resonance Region

by

Arthur O. Mateos

Submitted to the Department of Physics
on July 28, 1995, in partial fulfillment of the
requirements for the degree of
Doctor of Philosophy

Abstract

Measurements of the π^+ total absorption cross section on ^{4}He and its decomposition into competing channels were performed in the Δ resonance region using the Large Acceptance Detector System (LADS), at the Paul Scherrer Institute in Villigen, Switzerland. The LADS detector covers 98% of 4π solid angle, has a low detection threshold for protons (< 20 MeV), and can discriminate between γs and neutrons. Monte Carlo simulations were used to extrapolate over unmeasured regions of phase space. The total absorption cross section was measured to be 33.1 ± 7.0, 49.5 ± 6.6, 46.2 ± 6.4, and 23.8 ± 2.8 mb at incident pion kinetic energies of 70, 118, 163, and 239 MeV. Undisturbed quasideuteron absorption (QDA) accounts for the largest fraction of the total absorption cross section. Its contribution falls steadily as a function of energy from 66% at 70 MeV to 44% at 239 MeV. Contributions from non-QDA (*ppd*) final states fall as a function of energy from roughly 14% at 70 MeV to roughly 8% at 239 MeV. Two processes contribute to the *ppd* non-QDA absorption cross section, a (*pd*)*p* process which appears to be consistent with the pickup of a neutron following QDA, and a (*ppd*) process which shows significant deviations from phase space. Non-QDA *pppn* final states contribute substantially to the total absorption cross section. Their contribution rises with incident energy from 18% at 70 MeV to 44% at 239 MeV. The three nucleon (*ppn*)*p* process is favored over the (*ppp*)*n* process. The energy dependence of both processes exhibit a resonance-like behavior, with (*ppn*)*p* peaking slightly higher than (*ppp*)*n*. The energy dependence of the cross section for the four-nucleon absorption process is flat, its contribution being roughly 2.1 mb at the three higher energies. The flat energy dependence suggests that it is not an important pion absorption mechanism. Comparison with classical models indicates that contributions from hard FSI are important, particularly at lower incident pion energies. Indications of contributions from initial state interactions (ISI) are seen at the two higher incident pion energies.

Thesis Supervisor: Professor Robert P. Redwine
Title: Professor of Physics

Acknowledgements

This thesis represents the culmination of several years of work and would not have been possible without the assistance and encouragement of my advisor, colleagues in the LADS collaboration, friends, and family. I would like to take this opportunity to thank them for their support through these years.

My advisor, Bob Redwine, provided invaluable guidance throughout my graduate studies. His insight, advice, and encouraging words during difficult times provided direction when I may have otherwise floundered. Other members of our research group at MIT were also instrumental in providing guidance. Neven Simicevic, with his unparalleled exuberance for physics, helped introduce me to the physics of pion absorption and the LADS collaboration. When I joined the group, Kevin Wilson and David Rowntree were extremely helpful in showing the new graduate student the ropes. They started me on the way to understanding the intricacies and "features" of the LADYBIRD analysis code and continued to provide advice and assistance for data analysis as my research progressed. Thanks also go to Nik Gregory for his constant willingness to lend a helping hand and to Bryan Tipton for assistance with Monte Carlo simulations.

I am also grateful to all the members of the LADS collaboration from other institutions for the many man-years of effort spent on this endeavor. In particular, I would like to thank Quentin Ingram, Heinz Weyer, Danek Kotlinski, and the many graduate students who I have had the pleasure of meeting and working with through the course of the analysis. A special thanks goes to those I worked most closely with on the ^{4}He analysis, Ralf Trezeciak and Albert Lehmann. They were always quick to reply to my queries and to offer assistance.

I would like to thank Tim Chow and Dave Reiley for their friendship over the last few years. I learned much from them during our dinners together as they were always ready to engage in discussions on almost any topic be it mathematics, quantum mechanics, religion, or politics. I would also like to thank the gang on the fifth floor (Wilson Fong, Marla Dowell, Matt Osborn, and Christian Kunz), who made life as a graduate student at MIT much more livable.

I would like to thank Grace for the love, support and happiness we have shared. Finally, I would like to thank Mom, Dad, and Linda who have always been there for me, and were always behind me in whatever I chose to pursue.

Contents

List of Figures

List of Tables

Chapter 1

Background and Preliminaries

1.1 Introduction

The study of the interaction of pions with nuclei has been an area of intense interest for almost half a century. During the last two decades, high intensity pion beams have been available at three meson factories: LAMPF in the United States, TRIUMF in Canada, and PSI in Switzerland. There now exists an extensive body of data on the elastic scattering of pions on nuclei, and there has been much success in describing these data through the framework of multiple scattering theory. The pion absorption channel, however, remains somewhat of an enigma. Although understanding of absorption on the deuteron has reached a quantitative level, the mechanism behind pion absorption on heavier nuclei remains a mystery. It is now clear that the quasideuteron absorption mechanism (QDA) accounts for between 50% and 80% of the total absorption cross section. As the number of nucleons, A, increases and the incident energy of the incoming pion increases, the strength which is unaccounted for increases. The source of this remaining strength is still not well understood. To make progress toward understanding absorption in heavy nuclei, it is instructive to look at absorption in the helium isotopes ^{3}He and ^{4}He. These nuclei bear more of a resemblance to heavy nuclei than does the deuteron. In addition, multi-nucleon absorption modes which are unavailable on the deuteron are possible on these nuclei. The simplicity of these systems allows the possibility of making kinematically complete measurements of several different reaction channels. While there have been kinematically complete measurements in the past, they all have suffered from limited statistics and phase space coverage, particularly in the out of plane regions. The use of the

LADS detector allows one to sample a larger part of the phase space of these reactions than any previous experiment. It is hoped that this experiment will shed some light on the reaction mechanisms behind pion absorption. This thesis presents a measurement of the pion absorption cross section on ^{4}He at incident pion kinetic energies of 70, 118, 164, and 239 MeV with the LADS detector. The total absorption cross section is deduced from the sum of competing reaction channels and the differential distributions of various final states are examined.

1.2 Outline

The first chapter presents a brief introduction to pion-nucleus interactions. Pion absorption on the deuteron is discussed, followed by a review of what is known about pion absorption on heavier nuclei. The second chapter focuses on past work in pion absorption on the helium isotopes. In the third chapter, the characteristics and capabilities of the LADS detector are described. In the fourth chapter software and simulation tools are discussed. The fifth discusses the extraction of absorption events from the data sample and beam normalization. The sixth and seventh chapters are devoted to the decomposition of the total absorption cross section into competing channels and the presentation of differential results. Conclusions are presented in the final chapter.

1.3 The Pion Nucleon Interaction

In the quark picture of matter, the pion is the lightest of the mesons. It is the bound state of a quark-antiquark pair composed of up and down quarks. It is a spin-zero, pseudoscalar meson with isospin one, coming in three charge states. Important characteristics of the pion are listed in Table 1.1.

The pion was originally postulated by Yukawa as the fundamental massive particle responsible for the strong interaction [1]. From the range of the force, he deduced that the pion should have a mass of roughly 150 MeV. In 1947, the pion was discovered, and attempts were made to describe the strong force in terms of pion exchange. Difficulties were encountered in explaining strong interactions with pions as the fundamental field quantum, and the interactions of pions

Properties of the Pion					
	J^p	T	Mass	Mean Life	Decay Mode
$\pi^{\pm}$	0^-	1	139.567 MeV	2.6×10^{-8}s	$\mu\nu_\mu$ 99.9%
π^0	0^-	1	134.974 MeV	8.4×10^{-17}s	2γ 98.8%
Properties of the Delta					
	J^p	T	Mass	Width	Decay Mode
Δ	$\frac{3}{2}^+$	$\frac{3}{2}$	1232 MeV	120 MeV	$N\pi$ 99.3-99.5%

Table 1.1: Important properties of the pion and of the Δ.

with each other were particularly problematic due to parity considerations [2]. Upon the discovery of the heavier mesons, the pion lost its privileged role as the fundamental field quantum responsible for the mediation of the strong force. Although not the final answer, the meson exchange picture is still useful in describing the forces between nucleons. The long and medium ranges of the nuclear force are well described in terms of pion exchange [3, 4].

The most prominent feature of the pion-nucleon interaction in the intermediate energy region (80-300 MeV) is the Δ resonance. In the simplest picture, the Δ can be thought of as the first excited state of the proton, which is formed when the spin of one of the up quarks is flipped, resulting in a $T = \frac{3}{2}, J = \frac{3}{2}$ state [6]. The Δ resonance is centered around 1232 MeV and has a width of roughly 120 MeV. Its fundamental properties are summarized in Table 1.1.

The isospin of the Δ can be deduced by comparing the ratios of the following cross sections:

$$\sigma(\pi^+ p \to \pi^+ p) : \sigma(\pi^- p \to \pi^- p) : \sigma(\pi^- p \to \pi^0 n) \tag{1.1}$$

By applying the relevant Clebsch-Gordonry, one deduces that in terms of isospin channels, the cross sections can be written as:

$$\sigma(\pi^+ p \to \pi^+ p) = f_{3/2}^2 \tag{1.2}$$

$$\sigma(\pi^- p \to \pi^- p) = \frac{4}{9} f_{1/2}^2 + \frac{1}{9} f_{3/2}^2 \tag{1.3}$$

$$\sigma(\pi^- p \to \pi^0 n) = \frac{2}{9} f_{1/2}^2 + \frac{2}{9} f_{3/2}^2 \tag{1.4}$$

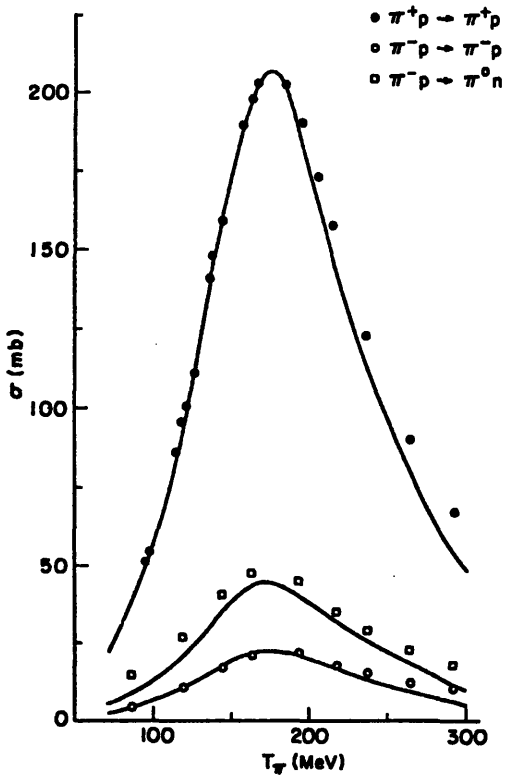

Figure 1-1: Energy dependence of pion-nucleon cross sections. From Reference [5].

where f_T is the scattering amplitude for a state with isospin T. Dropping the contributions from the $T = \frac{1}{2}$ amplitudes, one obtains the observed ratios at resonance, 9:1:2. Thus one concludes that the Δ is indeed a $T = \frac{3}{2}$ resonance.

The spin of the Δ can be deduced from the total cross section for $\pi^+ p$ scattering. If one assumes that there is no inelasticity in the channel, the cross section should be equal to

$$\sigma = \frac{2\pi}{k_{cm}^2(2J+1)}, \tag{1.5}$$

where k_{cm}^2 is the center-of-mass energy of the pion [7]. At resonance, if one assumes a value of $J = \frac{3}{2}$, one obtains a cross section of 190 mb. This is very close to the experimentally observed value. The fact that the Δ is a $J = \frac{3}{2}$ particle means that the pion which is scattered has an angular momentum $l = 1$ with respect to the proton. From this result, one is able to correctly predict the angular distributions for pion-nucleon scattering.

1.4 Pion Nucleus Interactions

There are several channels available for a pion to interact with a nucleus. The total pion-nucleus reaction cross section can be decomposed as follows:

$$\sigma_{total} = \sigma_{el} + \sigma_{inel} + \sigma_{abs} + \sigma_{CEX} + \sigma_{rad} \tag{1.6}$$

Elastic scattering, σ_{el}, refers to the process in which the pion scatters from the entire nucleus. Inelastic scattering, σ_{inel}, represents the portion of the cross section in which the pion loses some energy in the interaction, usually by knocking out one or more nucleons from the nucleus. Above an incident pion kinetic energy of about 200 MeV, pion induced pion production begins to make a contribution to the inelastic channel. Absorption, σ_{abs}, occurs when there is no pion in the final state. In a charge exchange reaction, σ_{SCX}, there is a pion in the final state which has a different charge from the intial state pion. There are two types of charge exchange reaction which are possible, single charge exchange reaction, when the charge of the initial and final state pions differs by one, and double charge exchange, when it differs by two. The last term represents radiative reactions σ_{rad}, which are reactions in which there is a γ in the final state. The radiative channels are important for stopped pion absorption on very light nuclei [8], but are ignorable for pion reactions in flight. As can be seen from Figure 1-2, σ_{el}, σ_{inel}, and

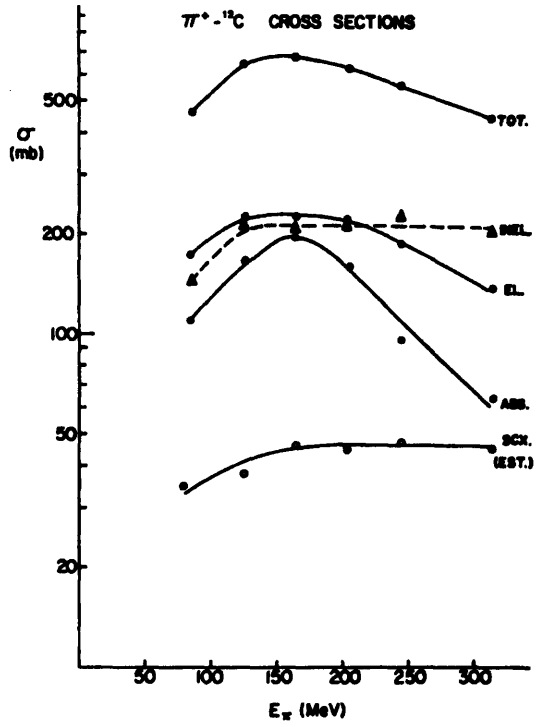

Figure 1-2: The energy dependence of pion-nucleus cross sections on ^{12}C [9].

σ_{abs} are of roughly equal importance at resonance, and account for most of the pion-nucleus reaction strength. The charge exchange reactions are an order of magnitude lower in strength.

Traditionally there have been two major motivations for studying pion-nucleus reactions. The first is that as an isospin one, spin zero particle, the pion is a useful tool for probing nuclear structure, complementary to other probes such as the electron. The second is that because of its strong coupling to the Δ the pion-nucleus interaction provides a unique opportunity to study a strong resonance in the presence of the nuclear field. Furthermore, the study of absorption is motivated by the hope that it will provide a better understanding of the NN interaction, as the pion is the mediator of the strong force over long ranges [10].

Much above and below the resonance, multiple scattering approaches to the pion nucleus interaction appear to be successful in describing the data. Multiple scattering treatments are traditionally employed at high energies, but also seem to be justified at low pion energies (< 80

MeV) because of the weakness of the interaction [11]. In the resonance region, complications arise due to the strength of the interaction and the length scales involved. In this regime, pion and Δ interactions in the nucleus are strongly coupled. Because of the resonance strength, the mean free path of a pion in the nuclear medium should be short ($\simeq$ 1 fm). The finite width of the Δ resonance means that it has time to interact with the nuclear environment. A theoretical approach called the Δ-hole model has been developed to deal with these issues and to treat pion nucleus interactions in this regime. This theory will be discussed in more detail in a later section.

1.5 Pion Absorption on the Deuteron

The absorption of a pion by a free nucleon is forbidden kinematically, but is possible by a nucleon in a nucleus. One nucleon pion absorption in a nucleus, however, is highly suppressed because of the large momentum mismatch between the incident pion and the momentum of the nucleon within the nucleus. The next higher order process possible is two-nucleon absorption. This process has been studied extensively through the reaction $\pi^+ d \rightarrow pp$. Many theoretical models have been developed which are in good agreement with experiment, matching the experimental differential cross sections and spin observables at the 10% level [12].

Absorption on the deuteron serves as the prototype for understanding pion absorption in nuclei. Theoretical approaches to absorption in nuclei are guided by what has been learned about pion absorption on the deuteron. In this section, the current experimental situation involving pion absorption on the deuteron is discussed along with the phenomenological basis for the understanding of the process. Theoretical approaches which are used to study the problem are then briefly reviewed. This section draws heavily from the treatments of pion absorption on the deuteron by Gell-Mann and Watson [7], Ericson and Wiese [13] (particularly the more theoretical aspects), and Weyer [12]. The phenomenology presented here, although first introduced by Gell-Mann and Watson over thirty years ago, still continues to guide our present physical understanding of the process.

Pion production cross sections	
Reaction	Isospin Cross Section
$pp \rightarrow d\pi^+$	$\sigma(1,0)_d$
$pp \rightarrow np\pi^-$	$\sigma(1,0)_{pn} + \sigma(1,1)$
$pp \rightarrow pp\pi^0$	$\sigma(1,1)$
$np \rightarrow d\pi^0$	$\frac{1}{2}\sigma(1,0)_d$
$np \rightarrow np\pi^0$	$\frac{1}{2}(\sigma(1,0)_{pn} + \sigma(1,1))$
$np \rightarrow nn\pi^+$	$\frac{1}{2}(\sigma(1,1) + \sigma(0,1))$
$np \rightarrow pp\pi^-$	$\frac{1}{2}(\sigma(1,1) + \sigma(0,1))$

Table 1.2: This table shows the decomposition of pion production cross sections as a function of isospin. For the $T = 0$ final state, the cross section has been divided into the cases in which a bound deuteron and an np pair have been produced (i.e. $\sigma(1,0) = \sigma(1,0)_d + \sigma(1,0)_{pn}$)

1.5.1 Pion Production and Absorption

Much has been learned about pion nucleon interactions through the study of pion production and absorption. The two processes are related to each other by the principle of detailed balance,

$$\sigma(\pi^+ d \rightarrow pp) = \frac{2}{3}\frac{p^2}{q^2}\sigma(pp \rightarrow \pi^+ d), \tag{1.7}$$

where q is the pion momentum and p is the nucleon's momentum in the center-of-mass system [13]. The cross sections for pion production can be written as the sum of four isospin cross sections. They are defined as $\sigma(\mathrm{T_1},\mathrm{T_2})$ where $\mathrm{T_1}$ is the isospin of the nucleon pair in the initial state and $\mathrm{T_2}$ is the final state isospin of the pair. The decomposition of pion production cross sections is summarized in Table 1.2.

By examining the differential distributions of these processes, the isospin cross sections can be decomposed into partial waves to give information on the underlying dynamics of the mechanism. The best studied of these isospin cross sections is $\sigma(1,0)_d$. Very accurate measurements of the total absorption cross section on deuterium have been made, and the total cross sections are known to 2-3% [14].

1.5.2 Data and Phenomenology of the Total Absorption Cross Section

The reaction $\pi d \rightarrow pp$ is well measured experimentally. A 1985 compilation of experimental results for the reaction below 1 GeV lists almost 200 published measurements [15]. Two main features characterize the total pion absorption cross section on the deuteron. The first is the rise near threshold, and the second is the peak at an incident pion kinetic energy of roughly 130 MeV due to the Δ resonance. Indeed, one can obtain excellent agreement with the data by just incorporating these two gross features and including a small offset to the overall normalization as Ritchie has done [16]:

$$\sigma(pp \rightarrow \pi^+ d) = (\frac{3.5}{T_\pi^{1/2}}\mathrm{MeV}^{1/2} + \frac{3.3\Gamma_0^2}{(E - E_R)^2 + \Gamma_0^2/4} - 1.2)\mathrm{mb}, \tag{1.8}$$

where

$$E_R = 2136\,\mathrm{MeV}, \Gamma_0 = 150\,\mathrm{MeV}, \tag{1.9}$$

and

$$E = [(m_\pi + M_d)^2 + 2T_\pi M_d]^{1/2} \tag{1.10}$$

is the πd invariant energy. The resonance energy is slightly smaller than the sum of the free masses of a nucleon and a Δ.

To understand the rise in the cross section near zero energy, it is useful to examine the inverse reaction, pion production. One can write the pion production cross section as a decomposition in partial waves, l_π, with the total cross section being a sum of these partial waves:

$$\sigma(pp \rightarrow \pi^+ d) = \sum_{l=0} \sigma_l(pp \rightarrow \pi^+ d) \tag{1.11}$$

The threshold behavior of the cross section for each of these waves is the barrier penetration factor, which varies as a function of pion momentum as [17]

$$\sigma(pp \rightarrow \pi^+ d) = \mathrm{const.} \times \eta^{2l_\pi+1}, \tag{1.12}$$

where $\eta = q/m_\pi$. From the principle of detailed balance, it follows that the cross section for s-wave absorption at threshold is an inverse square law relation in momentum. This behavior dominates for pion kinetic energies below roughly 10 MeV.

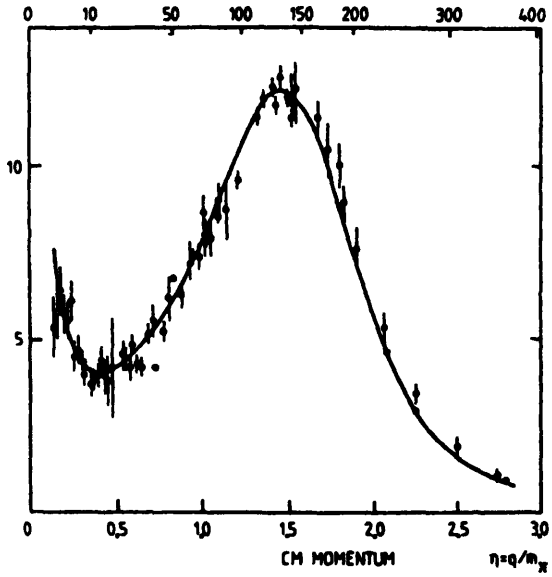

Figure 1-3: Energy dependence of pion absorption on the deuteron. From Reference [13].

For s-wave absorption, the pion brings in no angular momentum so that the final NN pair must have $J = 1$, the angular momentum coming from the original spin of the deuteron. The final state must also have negative parity and an isospin of one. This uniquely specifies the final state nucleons as being in a $^3P_1$ state.

At higher energies, the p-wave πd interaction begins to become important. The final state nucleons have isospin of one as in the case of s-wave absorption, but because of the angular momentum brought in by the pion, the parity of the final state is now positive. The allowable total angular momentum states for the two nucleons are now $J = 0, 1, 2$. This means that they must be in a singlet state, the only possibilities being $^1S_0$ and $^1D_2$. For a ΔN pair in a relative s-state, the possible spin and isospin states are $J = 1, 2$ and $I = 1, 2$ with positive parity. Hence, assuming Δ dominance, the $^1D_2$ state should be much larger than $^1S_0$ [7].

In Table 1.3 the possible NN final states following pion absorption on the deuteron are listed along with their corresponding amplitudes. The main amplitudes are directly determinable from measurements of the differential and total cross sections and polarization measurements.

The s-wave contribution to the total cross section is proportional to the amplitude $|a_1|^2$. As the energy increases, the p-wave amplitudes $|a_0|^2$ and $|a_2|^2$ start to contribute. Assuming

Partial waves for pion absorption on the deuteron			
l_π	NN	L	Amplitude
0	$^3P_1$	1	a_1
1	$^1S_0$	0	a_0
1	$^1D_2$	2	a_2
2	$^3P_1$	1	a_3
2	$^3P_2$	1	a_4
2	$^3F_2$	3	a_5
2	$^3F_3$	3	a_6

Table 1.3: This table lists the possible final state configurations of protons following pion absorption on the deuteron. The first column is the angular momentum of the incident pion, the second the quantum numbers of the final state. The third column is the orbital angular momentum of the NN pair, and the fourth column lists the corresponding amplitudes in the notation scheme of Gell-Mann and Watson [7].

that only the first two partial waves contribute, one can represent the total cross-section for s- and p-wave pion production as:

$$\sigma(pp \rightarrow \pi^+ d) = \frac{1}{4}[|a_1|^2 + |a_0|^2 + |a_2|^2] \tag{1.13}$$

Since the a_2 term is the one which contains the Δ, it is the one which is most important. For $T_\pi \leq 100$ MeV, the amplitudes $|a_1|^2$ and $|a_2|^2$ can be phenomenologically expressed as

$$|a_1|^2 \simeq 0.11\eta(1 - 0.25\eta + ...)^2 \,\mathrm{fm}^2 \tag{1.14}$$

$$|a_2|^2 \simeq 0.42\eta^3 \,\mathrm{fm}^2 \tag{1.15}$$

Because of its weakness, the amplitude $|a_0|^2$ is very poorly measured experimentally. It has been determined to be about two orders of magnitude smaller than $|a_2|^2$ [13].

1.5.3 Differential Cross Section

A convenient way of representing the differential cross section following the absorption of a pion by a deuteron is as a Legendre polynomial expansion as a function of the polar angle θ of an

outgoing proton:

$$2\pi\frac{\mathrm{d}\sigma}{\mathrm{d}\Omega}\sigma(\pi^+d\rightarrow pp)=\sum_j\alpha_{2j}P_{2j}(\cos\theta)\simeq\alpha_0+\alpha_2P_2(\cos\theta). \tag{1.16}$$

The total cross section is given by:

$$\sigma(\pi^+d\rightarrow pp)=\frac{1}{2}\int\mathrm{d}\Omega\frac{\mathrm{d}\sigma}{\mathrm{d}\Omega}\sigma(\pi^+d\rightarrow pp)=\alpha_0 \tag{1.17}$$

where the factor of $1/2$ comes from the fact that there are two particles in the final state. The Legendre coefficients can be related to the production amplitudes discussed earlier:

$$\alpha_0=\frac{p^2}{6q^2}\sum_i|a_i|^2\simeq\frac{p^2}{6q^2}[|a_1|^2+|a_0|^2+|a_2|^2] \tag{1.18}$$

$$\alpha_2=\frac{p^2}{6q^2}[|a_2|^2-2\sqrt{2}\mathrm{Re}(a_0a_2^*)] \tag{1.19}$$

It is interesting to note that the ratio of α_0 to α_2 is within 10% of unity throughout the Δ resonance region ($30\mathrm{MeV} < T_\pi < 165\mathrm{MeV}$) showing that $|a_0|^2$ and $|a_1|^2$ are indeed negligible. Deviations occur at energies above and below this energy range. Small values of α_4 have been observed above 140 MeV, indicating contributions from d-waves [12]. The measured values of the Legendre coefficients for pion absorption on the deuteron are shown in Figure 1-4.

1.5.4 Theory

Many theoretical approaches to pion absorption on the deuteron have been developed. While they differ conceptually, their predictions are consistent and agree with the data for both differential and spin observables at the 10% level.

The problem of pion absorption can be formulated in terms of a multiple scattering approach. The major problem one encounters is the optimization of the momentum exchange between nucleons immediately before or after the pion is absorbed. The differential cross section in the laboratory may be represented as,

$$\frac{\mathrm{d}\sigma}{\mathrm{d}\Omega_{lab}}(\pi^+d\rightarrow pp)=\frac{1}{32\pi^2}\left(\frac{pE}{q}\right)\frac{1}{3}\sum_{fi}|M_{fi}|^2 \tag{1.20}$$

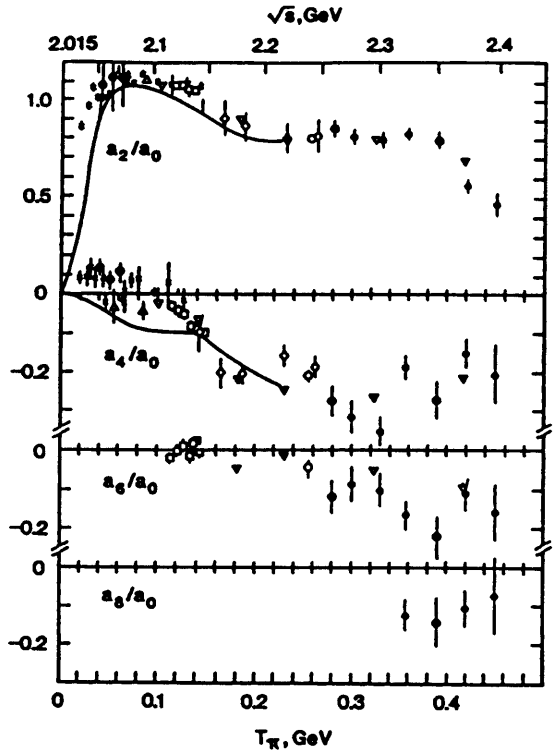

Figure 1-4: Energy dependence of Legendre coefficients for pion absorption on deuterium. From Reference [12].

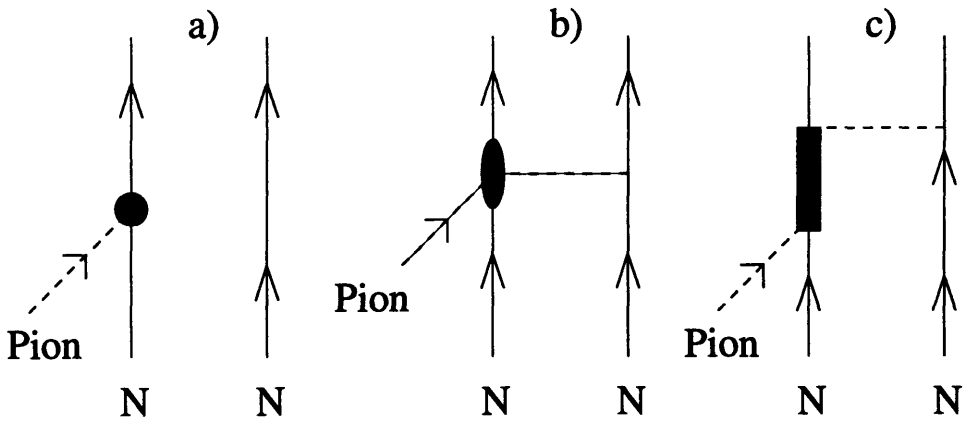

Figure 1-5: Diagram (a) represents the impulse approximation contribution to pion absorption on the deuteron. Diagrams (b) and (c) show the s- and p-wave rescattering contributions.

where p and q are the relative momenta of the outgoing proton pair and the incident pion. E is the laboratory energy of the πd system, and M_{fi} is the matrix element connecting the initial πd state to the final pp state [13].

In the impulse approximation (see Figure 1-5), the pion is absorbed on only one nucleon. The impulse approximation matrix element is given by:

$$M_{IA} = \langle f|H_{\pi NN}(1) + H_{\pi NN}(2)|i\rangle \tag{1.21}$$

where $|i\rangle$ and $|f\rangle$ represent the wavefunctions of the initial πNN and final NN systems. The basic πNN Hamiltonian from pseudovector coupling, including non-static corrections, is given by:

$$H_{\pi NN} = -\frac{f}{m_\pi}\sigma\cdot(\vec{\nabla}_\pi - \frac{\omega}{\mathbf{2M}}(\vec{\nabla}_\mathbf{N} - \overleftarrow{\nabla}_\mathbf{N}))\tau\cdot\phi(\mathbf{r}) \tag{1.22}$$

Evaluating this matrix element, with an initial deuteron state and a final state of $^3P_1$ protons, gives a contribution to the cross section which is only a few percent of that observed. The contribution is small because of the momentum mismatch and because contributions from the s- and d-wave states of the deuteron cancel each other out. The contribution from p-wave pions is larger than that of s-wave pions and contributes a non-resonant background to the cross section.

The next higher order contributions come from diagrams in which the pion initially scatters off a nucleon and then is absorbed (see Figure 1-5). The initial scatter can be divided into the case when an s-wave pion is scattered and then absorbed, and the case when a p-wave pion is scattered before being absorbed. The first is known as the s-wave rescattering mechanism, and the second the p-wave rescattering mechanism.

The s-wave rescattering mechanism involves an s-wave pion, which initially scatters from a proton and then is absorbed in a p-wave state relative to the second nucleon. The effective two-body operator for this process can be expressed as the operator representing the scattering from one nucleon multiplied by the propagator for the offshell pion and the basic πNN Hamiltonian described above:

$$H_{RS}(1,2) = H_S(1)\overline{D}(q_0', \mathbf{r})H_{\pi NN}(2) + (1 \leftrightarrow 2). \tag{1.23}$$

In the case of p-wave rescattering, the incoming pion interacts as a p-wave with the first nucleon before being absorbed. To first order, the following pieces must be included in the operator describing this process: a Hamiltonian representing the πNΔ transition, an energy denominator which describes the propagation of the Δ, and a transition operator for ΔN $\rightarrow$ NN. The Hamiltonian can be written as:

$$H_\Delta(1,2) = \frac{H_{\pi N\Delta}(1)V_{12}(\Delta N \rightarrow NN)}{\omega_\Delta - \omega - \frac{1}{2}i\Gamma_\Delta(\omega)} + (1 \leftrightarrow 2) \tag{1.24}$$

Using realistic wave functions for the deuteron and the proton pair, the matrix element for the two rescattering processes can be calculated. There are other effects such as the fact that the absorbing nucleons are moving which must be included in a correct treatment. Including these effects, the sum of contributions from the impulse approximation, and s- and p-wave rescattering mechanisms, one can reproduce the total pion absorption correction quite well.

There are some limitations, however, to the rescattering model. A detailed description of p-wave rescattering requires knowledge of the intermediate to short range dynamics of ΔN $\leftrightarrow$ NN, and currently this is poorly known. There is also the question of the convergence of the perturbation expansion [13].

Another approach which is pursued in the study of pion absorption on the deuteron is through coupled channel theory. Difficulties in calculation result in approximations as to which are the relevant degrees of freedom: pions, nucleons, Δ and other isobars, other mesons, and quarks. The choice of which approximations are made is the essential difference between these calculations. For example, the Helsinki group [18] includes the NN, NΔ, $\Delta\Delta$ channels. It treats

the Δ as a particle and includes both π and ρ exchange. A more phenomenological approach is adopted by Betz and Lee and co-workers [19]. Resonance dominance allows one to treat pion absorption as an inelastic ΔN transition. The coupled channel model of Betz and Lee includes production and absorption only through the Δ resonance. A phenomenological Hamiltonian is produced which is fit to NN phase shifts to get relative contributions of partial waves. Coupling to pion production and absorption is achieved through the inclusion of a πNΔ vertex. Good agreement is obtained for Δ dominated reactions but problems occur for reactions in which Δ intermediate states are inhibited. An attractive feature of the Betz and Lee calculation is that it is readily applicable for treating absorption in heavy nuclei.

A Faddeev-type approach is taken by Afnan and Blankleider *et al.* In their calculations they include the πd, NN , and NΔ channels, and also include background from the P_{11} channel [20]. Because of the complexity of the calculations, only three particles may be treated at once. Furthermore, in the Faddeev approach, mechanisms for pion absorption and production must be included explicitly. This introduces overcounting problems because these mechanisms are in a sense already partially included in the microscopic πN and NN amplitudes. The technical difficulties involved in performing these calculations make it difficult to gain physical insight from them.

1.6 Pion Absorption in Nuclei

In this section the experimental situation of pion absorption on nuclei is discussed, with primary emphasis on results from the last decade. Theoretical methods used to study absorption on nuclei are then presented. The next chapter focuses more closely on multi-nucleon pion absorption and experimental results on the helium isotopes.

From the early days of particle physics, when pion absorption was first studied on the deuteron, it was widely believed that pion absorption on nuclei took place in the same manner as on the deuteron, with the energy of the absorbed pion being shared between two of the nucleons in the nucleus. A pioneering measurement of pion absorption was conducted by Favier *et al.* at CERN in 1971 [21]. This experiment was a coincidence measurement of $(\pi^+, 2p)$ performed at one angular setting at an incident pion kinetic energy of 76 MeV on 16 different nuclei from the deuteron to Pb. They found that the two proton yield for low nuclear excitation of the final state was consistent with absorption on two nucleon clusters within the nucleus. They also pointed out that the majority of absorption appeared to take place through processes more

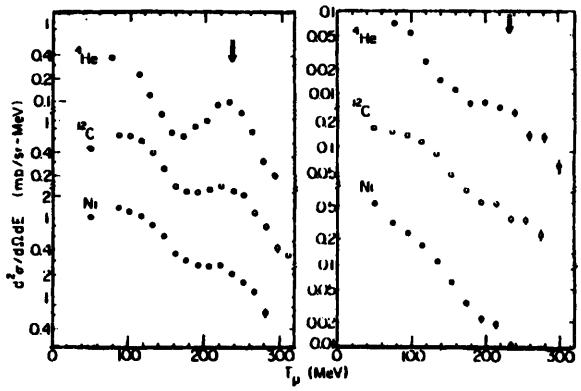

Figure 1-6: A (π, p) inclusive spectrum. From Reference [14].

complex than quasifree absorption alone. They argued that the degradation of missing mass distributions as a function of A could be indicative that the primary absorption mechanism is QDA and that the degradation is a result of distortion.

As the meson factories came into operation in the late seventies, the idea that pion absorption on nuclei proceeds primarily through QDA began to be tested. Most of the earlier experiments were one-arm measurements which examined the inclusive (π, p) yields [22, 23]. At forward angles larger than roughly $\theta_{LAB} > 45°$, high energy protons (with energies greater than 60 MeV) can come only from absorption processes. A surprising result which came from these measurements is that while in the lighter nuclei a high energy peak corresponding to two nucleon absorption was observed, for nuclei larger than ^{12}C, a strong peak is no longer visible. The question which arose was whether the absence of a prominent peak was due to nuclear distortion effects or due to an absorption mechanism involving clusters of more than two nucleons.

The primary impetus for the present day searches of multi-nucleon absorption modes can be traced to the early 1980s with the rapidity measurements of McKeown *et al.* [24]. Through an analysis of the rapidity of protons from a single arm measurement, the authors deduced the number of participating nucleons under the assumption that the absorption mechanism was forward-backward symmetric. They found that the average number of participating nucleons was greater than two for all nuclei studied. From their data, one might conclude that the number of participating nucleons in the absorption appears to rise as a power law in A. Although they were able to conclude that, on the average, several nucleons were involved in the absorption,

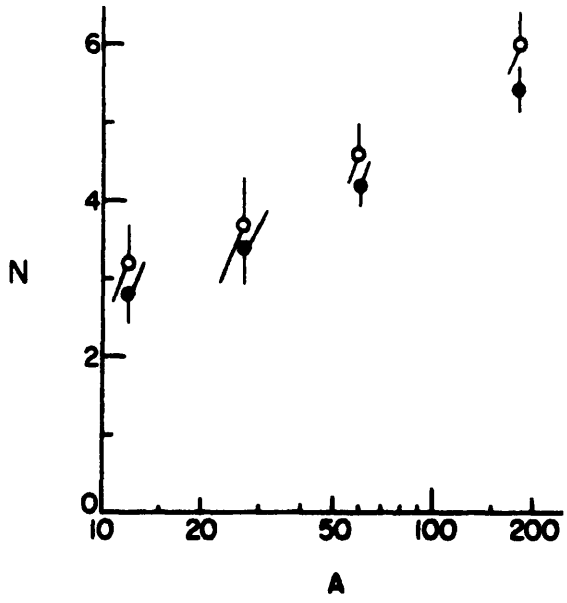

Figure 1-7: A dependence of number of participating nucleons in pion absorption. From Reference [24].

they were unable to establish whether or not the multi-nucleon events were the result of a QDA mechanism with initial or final state interaction or to a multi-nucleon mechanism.

Complementary measurements of the total absorption cross section were carried out throughout the resonance region on a large range of nuclei [9]. These measurements typically proceeded as follows: First a transmission experiment was conducted to determine the total pion reaction cross section. Next the inclusive pion angular distribution was measured, and the cross section for single charge exchange estimated. The absorption cross section was determined by subtraction of the cross section in which there was a pion in the final state from the total pion reaction cross section.

A new generation of coincidence (π, NN) experiments were performed. An important result of this work was the confirmation of the dominance of absorption on $T = 0$ pairs over absorption on $T = 1$ pairs. This was accomplished by comparing the ratio of (π^+, pp) to (π^-, np) on ^{3}He[28, 29, 30, 31]. Under the assumption of isospin symmetry, the ratio of these cross sections can be related to the isospin amplitudes [12]:

$$R_{^3He} = \frac{\sigma(\pi^+, pp)}{\sigma(\pi^-, pn)} = \frac{3/2\sigma_{01} + 1/4\sigma_{11}}{1/3\sigma_{10} + 1/2\sigma_{11}} \tag{1.25}$$

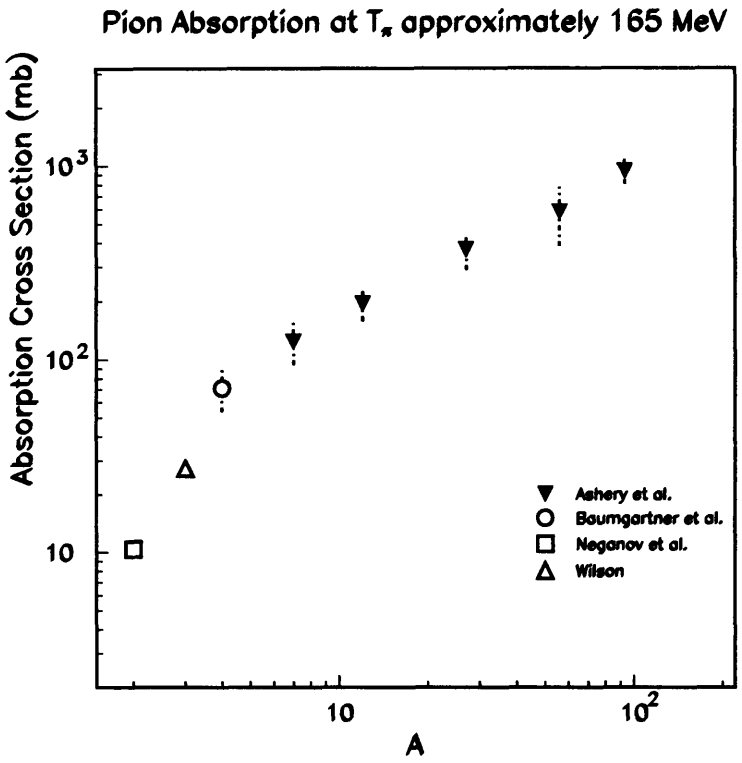

Figure 1-8: The A dependence of pion absorption on nuclei at 165 MeV. The inverted triangles are from the measurement of Ashery *et al.* [9], the circle is from the measurement by Baumgartner *et al.* [25], the triangle is from the measurement of Wilson [26], and the square is from the measurement of Neganov and Parfenov [27].

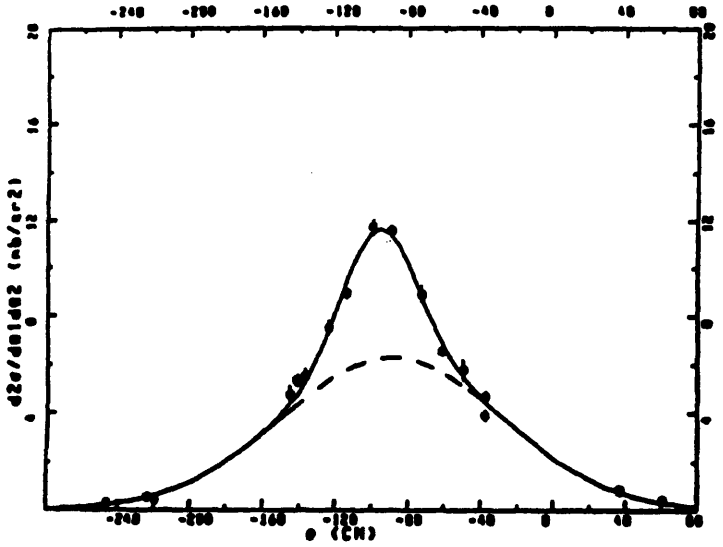

Figure 1-9: A double Gaussian decomposition of the angular correlation from the Burger *et al.* experiment. From Reference [34].

It was determined that in the Δ resonance region, that absorption on $T = 0$ pairs is an order of magnitude larger than the isovector $T = 1$ channel. The suppression is caused by constraints on the initial state due to the Pauli principle which causes different partial waves to be chosen for π^+ and π^- absorption.

Two-proton coincidence measurements on heavier nuclei can be divided into two classes. The first are inclusive measurements [32, 33] whose primary focus is the determination of the fraction of absorption which is quasi-deuteron. The second class involve high resolution measurements which are able to resolve final nuclear states. These measurements are particularly useful for studying the details of the quasifree absorption mechanism and the effects of nuclear structure on the mechanism.

A landmark inclusive measurement was performed by Burger *et al.* on ^{58}Ni at 160 MeV [35, 36]. In this experiment, the angular correlation was decomposed into two Gaussians. The thinner Gaussian was associated with contributions from an undisturbed two-nucleon mechanism, and the broader was associated with more complex processes. After corrections due to nuclear distortion effects such as ISI and FSI, only about 30% of the absorption cross could be explained in terms of a two-nucleon process.

More recent high resolution measurements on ^{16}O [37, 38, 39] also indicate that a large fraction of the absorption cross section cannot be explained by a two nucleon mechanism. The Maryland group reports that $\simeq$ 75% and $\simeq$ 50% of the total absorption cross sections at 115 and 165 MeV can be explained by the quasifree process.

At present, the focus of pion absorption measurements has shifted to large solid angle studies. The BGO collaboration has published measurements of the total absorption cross section for a large number of nuclei [40, 41]. Their results are systematically lower than those reported by Ashery *et al.* This discrepancy is not yet well understood but may be due to problems associated with corrections due to the energy detection threshold. As for the inclusive measurements, it is difficult to draw quantitative conclusions because serious simulations have not been performed. The qualitative conclusion which can be drawn from these measurements is that the probability of three proton emission following absorption is much smaller than the probability of two proton emission.

1.7 Theoretical Approaches to Pion Absorption

Many theoretical techniques have been developed to study pion absorption in nuclei. These include classical calculations such as intranuclear cascades (INCs) [42, 43, 44], semi-classical calculations such as those derived from kinetic theory and the Boltzmann equation [45, 46], and quantum mechanical calculations. The quantum mechanical calculations can be further subdivided into those which are based on the optical model [47] and those based on the Δ-hole model [48, 49]. Approaches which are particularly relevant are discussed. The INC calculations are described because they are the ones which can be most easily compared to data. The optical model approach and the Δ-hole model will be described along with a hybrid calculation of Ohta, Thies, and Lee [50] because the conclusions drawn from these three analyses show promise as a means for understanding the apparent anomalies between the total and two-nucleon results.

In performing an INC calculation, one propagates a pion through a nucleus classically and uses free πN and NN cross sections and a parameterization of the QDA process to simulate the absorption. This type of calculation is entirely classical and treats the individual processes incoherently. It enjoys wide popularity because it can be used relatively easily to produce variables which can be compared with experiment [51]. In the past, INC calculations have been criticized because in order to reproduce the data, they have adopted unrealistic nucleon mean-free-paths. In this thesis, two types of INCs will be used for comparison with the data.

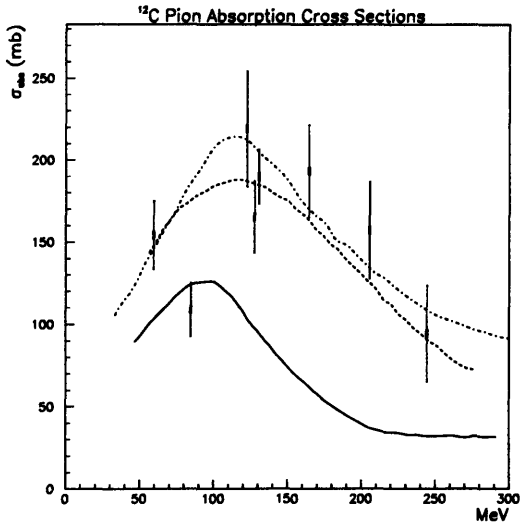

Figure 1-10: A comparison of theoretical calculations of the total absorption cross section on ^{12}C with experiment. The dashed line is the prediction of the optical model, the dotted-dashed line the prediction of the Δ-hole model, and the solid line is the calculation of OTL.

The first class is a set of simulations which have been created to model a specific process (i.e. an initial state interaction ISI). The distributions produced by these simulations are compared with the data to assess whether or not such a process is important in absorption. The other INC which is used is a full-blown cascade code, developed by Gibbs [52], which attempts to model all of the interactions which occur in the nucleus. In this INC, Gibbs has replaced the classical nucleon-nucleon scatters with quantum mechanical NN potentials and has included a realistic pion absorption vertex.

In the optical model approach to the problem, one uses the optical theorem and the strength of the elastic scattering cross section to predict the absorption cross section. According to the optical theorem,

$$\frac{4\pi}{k} Im f(0°) = \sigma_{el} + \sigma_{re} = \sigma_{tot} \tag{1.26}$$

and

$$\sigma_{re} = -\frac{2\omega}{k} \langle \Psi^{(+)} | ImU | \Psi^{(+)} \rangle \tag{1.27}$$

The reaction cross section must then be decomposed into contributions which come from absorption and from other contributions to the imaginary part of the potential (such as those

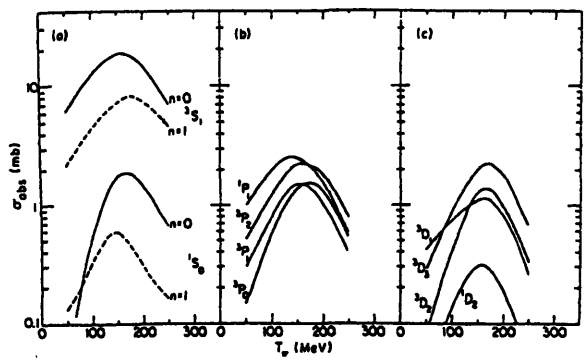

Figure 1-11: The relative contributions of pairs of nucleons in a nucleus to pion absorption as calculated by Ohta, Thies, and Lee [50].

arising from inelastic channels), $U = U_{sc} + U_{abs}$. After scattering due to the imaginary part of the scattering potential, the pion may be absorbed at a later stage. The total absorption cross section is a sum which includes contributions in which the pion scatters any number of times. The optical model approach works well at low energies but runs into difficulties at higher energies because of approximations which must be invoked to keep the calculations tractable when more and more scatterings occur [53].

The Δ-hole calculation also attempts to calculate the total absorption cross section from an analysis of elastic π-^{4}He scattering, but it explicitly introduces the Δ as a degree of freedom of the system. The main difference is that in the Δ-hole model, one includes a phenomenological Δ-nucleus "optical potential" with strength parameters which are determined from π-nucleus scattering data. The Δ-nucleus potential is characterized by two complex parameters, one representing a central potential, and the second a spin-orbit contribution. The predictions of the Δ-hole model agree well with the experimentally observed energy dependence of the cross section, but the agreement at high energies may be fortuitous because of the same problems which plague the optical model calculations [54].

In the calculation of Ohta, Thies, and Lee (OTL), an attempt is made to predict the strength of the absorption channel based on a quasi-deuteron model. OTL use the Δ-hole model and the phenomenological Hamiltonian of Betz and Lee, which connects the πNN, ΔN, and NN states as mentioned in a previous section. The calculation is performed by folding the πNN $\leftrightarrow$ ΔN $\leftrightarrow$ NN amplitude into the nuclear wavefunction. The principal result of this analysis is that the $^3S_1$ contribution (the one which is identical to the deuteron) is favored by an

order of magnitude over all other nucleon pairs (see Figure 1-11). While the OTL calculation has much success in explaining inclusive proton spectra, its predicted contribution to the total cross section is less than half of the observed value.

1.8 Summary

Pion absorption on nuclei and the mechanisms responsible for this process represent an open problem in nuclear physics today. Although there is now a quantitative understanding of absorption on the deuteron, the question still remains whether QDA alone can explain pion absorption in nuclei. Experiments thus far have not been able to determine the fraction of pion absorption due to a fundamental QDA process and the dependence of this fraction as a function of A and energy to a quantitative level. One can probably say, however, that a trend is emerging which indicates that there are higher numbers of participating nucleons as a function of energy and A and that a substantial amount of the absorption yield cannot be explained by the QDA mechanism. Experiments and theory both point to the privileged role of pairs with deuteron-like quantum numbers, but whether processes involving more than two nucleons coherently are important for absorption has not been settled.

Is the emission of many nucleons during absorption due to a two-nucleon absorption which is modified by nuclear medium effects such as pion scattering before absorption or nucleon-nucleon collisions? Or is it due to some sort of process in which more than two nucleons participate directly in the absorption? It is through the study of absorption on the helium nuclei, the subject of the next chapter, that one may make progress toward answering these questions.

Chapter 2

Multi-Nucleon Absorption on ^{3}He and ^{4}He

2.1 Introduction

A significant motivation for studying pion absorption on ^{4}He is that previous experiments have reported a dramatic rise in the cross section from ^{3}He to ^{4}He. The power law dependence which characterizes the rise in the cross section as a function of A near resonance appears to begin with ^{4}He (see Figure 1-8). This suggested to many people that between ^{3}He and ^{4}He, a new absorption mechanism which was important in all heavier nuclei opened up [55]. More recently published measurements, at slightly lower energies, are consistent with the total absorption cross section on ^{4}He being smaller than previously indicated [56, 57]. It is not currently known whether the absorption cross section on ^{4}He scales in the same manner as it does from deuterium to ^{3}He, or whether it follows the power law dependence characteristic of heavier nuclei. It is clear that in order to make an accurate determination of the fraction of absorption events attributable to the quasi-deuteron mechanism the total absorption cross section needs to be determined more accurately.

2.2 Classification of multi-nucleon absorption mechanisms

At first glance, it may appear that a useful way to classify absorption mechanisms is by the number of participating nucleons. If one takes this approach one must next define what one

means by participating nucleon. The conventional explanation of multi-nucleon pion absorption is that it is a multi-step process consisting of a QDA mechanism, pion interactions with nucleons prior to absorption (initial state interactions ISI), and NN final state interactions (FSI) after the primary two-body mechanism. This is, of course, a classical simplification in which one envisions the processes to be occurring sequentially and incoherently. This is the starting point for the classical INCs, which have been used over the years in an attempt to understand pion absorption.

It is important to note that in this scheme there is no clear distinction between a sequential process and a one-step process. Both represent limiting cases of the same phenomenon. In the limit that the sequential processes occur closer and closer together in time and space, this distinction becomes meaningless, and one begins to call the process a genuine multi-nucleon process. The sequential process picture represents the case when the propagators are on the mass shell, while the one-step process is appropriate if the exchange particle is far off the mass shell. Such a nomenclature for defining two- and multi-nucleon absorption suffers from ambiguity stemming from the fact that the dividing line between these two processes is inherently ill-defined. Nevertheless, this is the framework in which multi-nucleon processes have traditionally been discussed.

To avoid the ambiguity inherent in the above classification scheme, Thies proposed an alternative scheme for classifying absorption processes, and this is the classification which will be adopted here for discussion [55]. In the Thies system, one divides the Hilbert space of available states into subspaces which are ordered by the number of holes n which they contain. The subspaces which are important are the following:

- Pion Channels (P_n)
- Delta Channels (D_n)
- Absorption Channels (A_n)

The Hamiltonian is assumed to be composed of only two-body interactions, in the form of a $\pi N\Delta$-vertex and two-baryon potentials. The relevant diagrams are shown in Figure 2-1. The Δ states serve as doorways between the pion and the absorption channels. The possible mechanisms for absorption can be represented in a tree diagram scheme as in Figure 2-1. Each separate path through the tree diagram represents a different absorption mechanism. The final absorption channel represents the number of emitted nucleons. For any given absorption channel

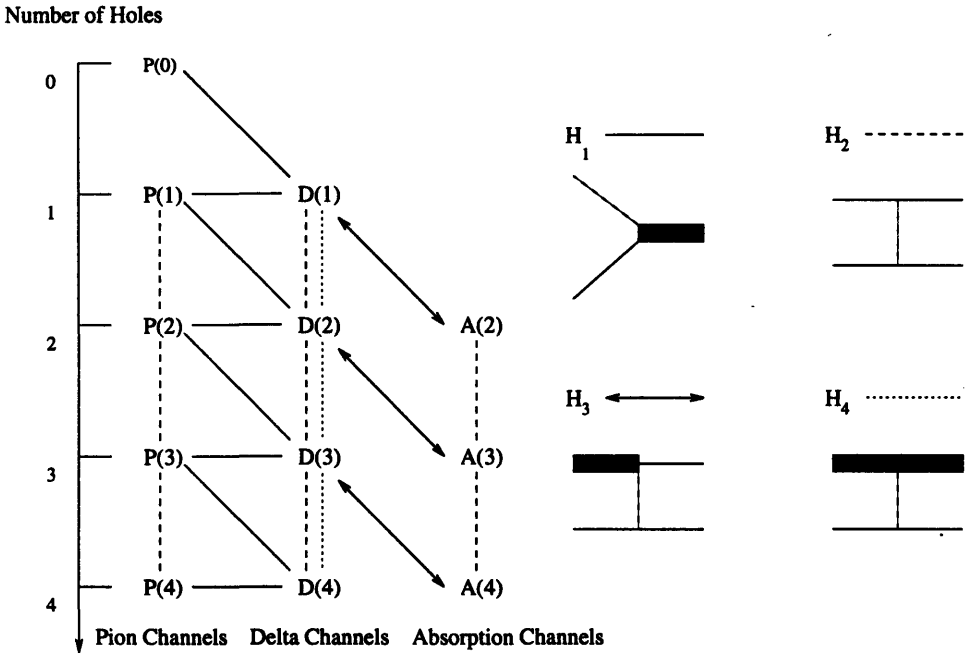

Figure 2-1: Thies's classification of pion absorption mechanisms. Adapted from Reference [53]

A_n, there is only one genuine path through the tree diagram which cannot be decomposed into ISI or FSI type processes.

For the case of A_2, there is only one path from P_0 to A_2, $P_0 \rightarrow D_1 \rightarrow A_2$. This path corresponds to quasi-deuteron absorption. For the case of A_3, or three nucleon emission, there are three distinct possibilities. One is an ISI-type process, ($P_0 \rightarrow D_1 \rightarrow P_1 \rightarrow D_2 \rightarrow A_3$), and another is an FSI-type process ($P_0 \rightarrow D_1 \rightarrow A_2 \rightarrow A_3$). The final possibility, ($P_0 \rightarrow D_1 \rightarrow D_2 \rightarrow A_3$), is not decomposable into intial or final state interactions, and may be identified as a "genuine" three-nucleon process. This process would be the result of Δ interactions inside the nucleus, which are possible because of the Δ's finite lifetime. For the case of four nucleon emission, there are five paths built up from quasi-deuteron absorption, two paths built from the genuine three-nucleon process, and one path corresponding to genuine four-nucleon absorption.

2.3 Classical Signatures of Sequential Absorption Mechanisms

Sequential absorption processes may retain some of the physical characteristics of the individual steps, and thus be identifiable experimentally. In this section kinematical signatures which have been used to identify these sequential processes are reviewed.

For the case of ISI followed by two-nucleon absorption, one expects the collinear kinematics which are characteristic of two-body absorption. One also expects that one of the protons in the final state should bear a kinematical resemblance to free πp scattering. These signatures could possibly be smeared by the initial momentum of the struck nucleon, but this effect can be taken into account in simulation [51]. Salcedo *et al.* have proposed another method for determining whether ISI contributions are important [58]. They have suggested that if an initial state interaction occurs before a genuine two-body absorption, one should see a peak in the pseudo-invariant mass squared distribution corresponding to the mass of the boson exchanged. The pseudo-invariant mass is defined as:

$$M^2{}_{ij} = (T_i + T_j)^2 - (\mathbf{p}_i + \mathbf{p}_j)^2, i = 1, 2, 3, \tag{2.1}$$

where $T_i, \mathbf{p_i}$ are the kinetic energy and momenta of the outgoing nucleons. Another predicted effect of ISI before absorption is that *ppp* final states would be enhanced over *ppn* and *pnn* final states. This is a consequence of the isospin dependence of πN scattering [59].

Hard FSI following two-nucleon absorption should also be identifiable. It is likely that only one of the nucleons which participated in the absorption will be involved in a nucleon-nucleon hard scatter. The other nucleon's energy should remain unaffected. This should result in bands in the Dalitz plot connecting the quasifree 2NA regions. Another telltale sign of the hard FSI process is the observation of two nucleons at right angles to one another. Lee suggests that FSI would also manifest itself in a high energy peak in the energy distribution of a proton measured in coincidence in such reactions as $^3\mathrm{He}(\pi^{\pm}, pn)$ [60].

Soft final state interaction (soft FSI) is a phenomenon which has been observed in a wide variety of reactions with hadrons in the final state. It is characterized by a preference of final states in which nucleons undergoing soft FSI having small relative momentum between them. Soft FSI can be clearly seen as enhancements in certain areas of Dalitz plots, and appears to be particularly strong at lower incident pion energies, and in π^- absorption (See Figure 2-2).

2.4 Experimental Results on ^{3}He

The ^{3}He nucleus has been studied in much greater detail than the ^{4}He nucleus in kinematically complete measurements. This is the case because a kinematically complete measurement of pion absorption on ^{3}He requires only a two-fold coincidence, while such a measurement on ^{4}He requires a three-fold coincidence.

Before proceeding to pion absorption on ^{3}He in flight, an important kinematically complete stopped pion absorption measurement made in the early 1980s at PSI is discussed [28]. In this experiment, stopped π^-s were absorbed by ^{3}He. Almost 70% of the yield was due to absorption on a deuteron-like $T = 0$ pair, with the yield from the $T = 1$ pair an order of magnitude lower. Soft FSI appeared to be responsible for the remainder of the yield. The conclusion from this experiment is that the entire ^{3}He absorption yield could be attributable to 2N-absorption mechanisms and soft FSI, without the need for invoking 3N processes. This is a very different situation from what is observed for pion absorption on ^{3}He in flight.

Unlike in heavier nuclei, the total cross section for ^{3}He has not been measured by inference from transmission experiments. Before the LADS measurement, all total absorption cross sections on ^{3}He were made by measuring the angular distribution of the 2NA component and extrapolating this measurement over all angles. The 3NA component was measured at several

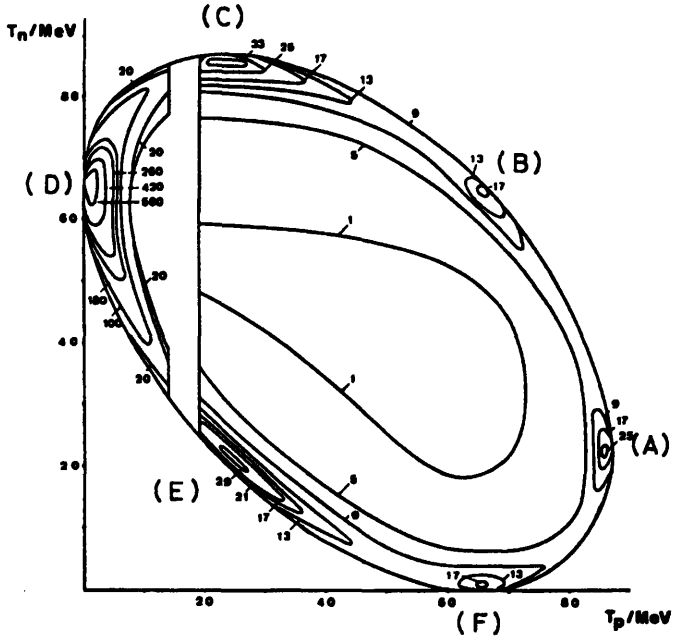

Figure 2-2: A Dalitz diagram of the final state particles following stopped pion absorption on ^{3}He. From Reference [28].

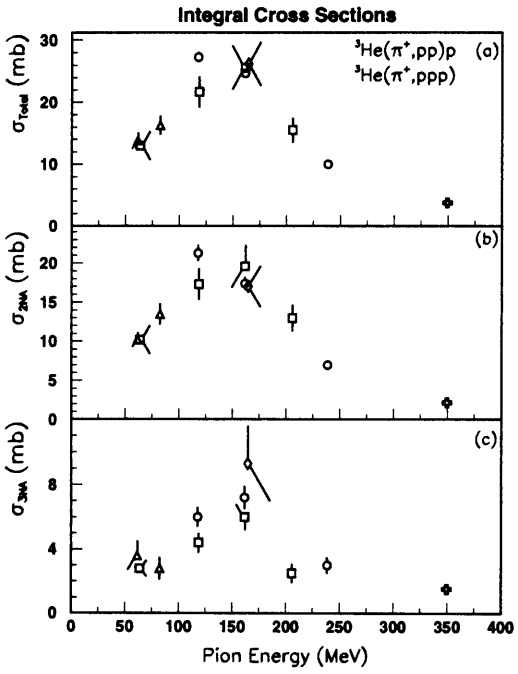

Figure 2-3: Total absorption cross sections on ^{3}He. From Reference [61].

angles in plane and then extrapolated with a phase space like assumption. Measurements of the total, 2NA, and 3NA pion absorption on ^{3}He are shown in Figure 2-3.

Kinematically complete total cross section measurements of pion absorption on ^{3}He have been conducted at LAMPF at energies 165, 350, and 500 MeV [62, 63]; at TRIUMF at energies 62.5 and 82.8 MeV [64]; and at PSI at energies 64, 119, 162, and 206 MeV [65]. Although these experiments on ^{3}He differ in their particulars, they all were basically two arm coincidence measurements consisting of a spectrometer and a time of flight (TOF) array detecting nucleons from the absorption in coincidence. The angle between the spectrometer and TOF-arm was varied so as to obtain configurations which were believed to favor either 2N-absorption kinematics or 3N-absorption kinematics. Placing the detectors colinearly allowed one to favor events in which two nucleons participated in the absorption, while non-conjugate angles favored 3N processes.

These two-arm experiments established that the 2N quasi-deuteron type process gave the largest contribution to the total absorption cross section. For energies at or below resonance, it was reported that the contribution of the 2N process was roughly 1.5 times that of pion absorption on the deuteron. It is interesting to note that there are 1.5 quasi-deuteron pairs in ^{3}He. Some authors have suggested that since the observed 2N cross section in ^{3}He is roughly 1.5 times that of the deuteron at the corresponding energy, FSI and ISI are unimportant [59]. Others claim that this equality could be the result of a fortuitous cancellation of an increase in cross section due to increased nucleon density, and a decrease in observed 2N cross section from losses due to ISI and FSI. For pion energies above the resonance, the quasi-deuteron absorption cross section is 30% larger than 1.5 times the deuteron absorption cross section. Smith *et al.* [62] attribute this enhancement in the cross section to the binding of the quasi-deuteron in the nucleus.

No deviation from phase space like behavior was reported for the energy sharing of final state nucleons for 3NA. There were however some indications of deviations from phase space flat behavior in polar angle. Although there was no conclusive evidence, some authors mentioned the possibility of ISI in their data [62, 63]. Soft-FSI was identified in some of these experiments, particularly those at lower energies and with an incident π^- beam [64, 65]. None of the experiments reported finding any evidence of hard FSI.

The recent LADS measurements of pion absorption on ^{3}He at energies of 118, 162 and 239 MeV were the first large solid angle measurements of the cross section [61, 26]. These measurements show that the peaking of the total and 2NA cross sections occurs at a lower energy than previously indicated. An examination of the 3NA yield showed that the energy

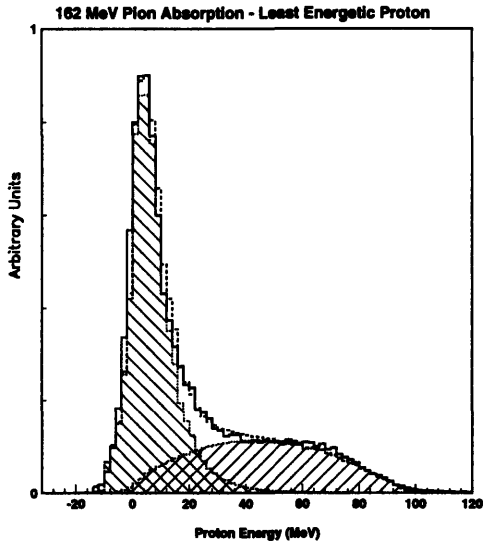

Figure 2-4: Energy distribution of the least energetic proton following pion absorption in flight on ^{3}He. From Reference [61].

sharing between nucleons was to a very good approximation phase space like (see Figure 2-4). It was also found that angular deviations, particularly those occurring out-of-plane, lead to systematic errors in the determination of the magnitude of the three nucleon cross section on the order of 25-30% for measurements which are performed solely in plane. Furthermore, for the first time, indications of an ISI type process were identified for absorption, most strikingly at the highest measured energy (see Figure 2-5).

2.5 Experimental Results on ^{4}He

Three experiments performed in the 1950s and 1960s identified events which were possibly attributable to pion absorption on ^{4}He by Fowler *et al.* at 60 and 105 MeV [66] by Budagov *et al.* at 153 MeV [67], and by Kozodaev *et al.* at 273 MeV [68]. These experiments were unable, however, to distinguish between absorption and SCX. The total pion absorption cross section on ^{4}He was measured in the early 1980s by Baumgartner *et al.* [25] using the subtraction method commonly used for analysis of heavy nuclei (see Figure 2-6). These measurements provide the

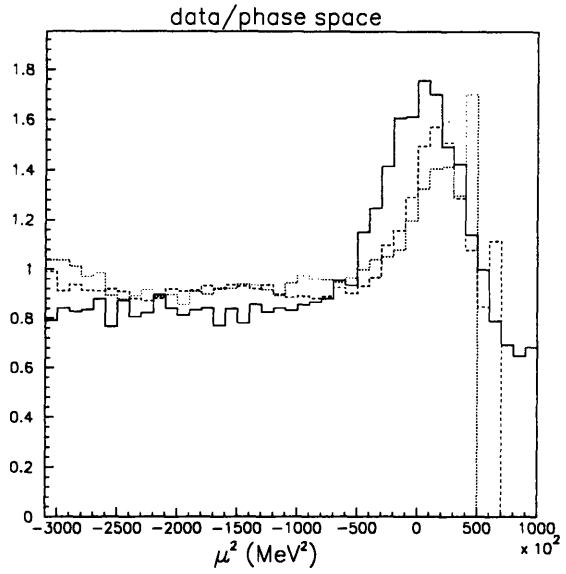

Figure 2-5: Distributions of the pseudo-invariant mass of the data divided by phase space for three nucleon absorption on ^{3}He. From Reference [26].

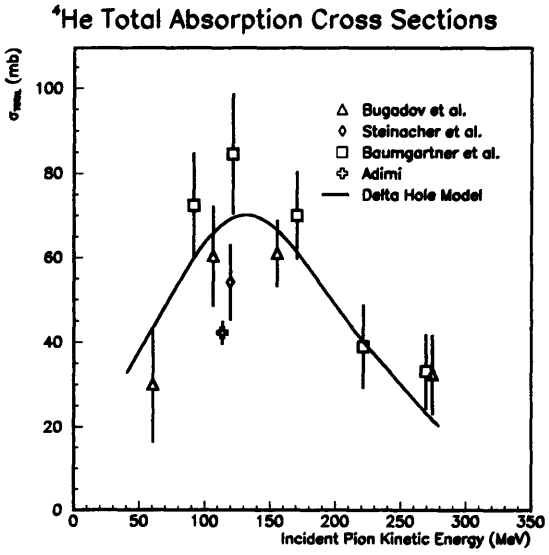

Figure 2-6: Total absorption cross sections on ^{4}He.

only systematic study of the total absorption cross section throughout the resonance region. The Baumgartner *et al.* experiment measured the inelastic pion cross section at six energies from 90 to 320 MeV. By combining their measurement with the total pion cross sections of Binon *et al.* [69] and an estimate of the SCX cross section, they were able to make a determination of the total absorption cross section. The results of the experiments from the 1950s and 1960s have since been reanalyzed in the same manner as Baumgartner *et al.*, using the Binon *et al.* results and yield slightly lower total cross sections than Baumgartner *et al.*.

The total absorption cross section has been measured by summing competing channels at 120 MeV by Steinacher *et al.* [56] and at 114 MeV by Adimi [57]. These measurements are systematically lower than those obtained by the subtraction method. Steinacher reports 52.7 $\pm$ 9.0 mb, while Adimi reports 42.23 $\pm$ 2.71 mb.

At present the total absorption cross section on ^{4}He is not known with very much quantitative precision. Therefore it is unclear whether it falls on the $A^{0.7}$ dependence line which characterizes absorption on heavy nuclei or behaves more like deuterium and ^{3}He.

Small angle coincidence measurements of pion absorption on ^{4}He have been conducted at PSI at 65, 120, and 165 MeV [56]; at TRIUMF at 165 MeV [70]; and at LAMPF at 500 MeV [71]. A large solid angle measurement, covering roughly 55% of 4π at energies 64, 87, 114, 162, 217, 278, and 327 was also performed at PSI by Breuer *et al.* [72, 73].

The earlier PSI experiment focused mainly on absorption at 120 MeV, with measurements at 65 and 165 MeV restricted to determination of the cross sections for the quasifree *pp* and *pd* channels. By performing both π^+ and π^- measurements at 120 MeV and by using isospin symmetry arguments, the Steinacher group was able to decompose the absorption cross section into various contributing channels. A summary of their results is listed in Table 2.1. They reported that the 2NA ($T = 0$) cross section appears to be a factor of three larger than absorption on the deuteron, consistent with the number of ($T = 0$) pairs in a ^{4}He nucleus. They also reported that ($T = 1$) absorption is suppressed in ^{4}He but is a factor of two larger than that observed in ^{3}He.

The Steinacher group also reported that most of the multi-nucleon absorption is of the 3NA type, and not of the 4NA type. They also found that, as was the case for ^{3}He, no signatures of ISI or FSI were visible in the data. The *ppp* channel appeared to be smaller than the *ppn* channel, which is what one would expect if ISI were unimportant.

The TRIUMF measurement concentrated on the determination of the contribution of 3NA to the absorption cross section. It reported a *ppp* cross section of 4.8 ± 1.0 mb at 165 MeV and estimated the contribution from a 4NA process to be less than 2 mb. The energy sharing of the protons appeared to agree partially with what one would expect for 3-body phase space, but there was some incompatibility between their models and the data. They suggested that the data were consistent with the 3NA being a mix of a genuine 3NA absorption process and an ISI+2NA process. They found no indication that FSI processes are important.

The LAMPF measurement at 500 MeV reported a 2NA contribution of 1.14 ± 0.11 mb and a 4NA cross section of 2.5 ± 0.6 mb. It was reported that because of angular deviations for three nucleon absorption, a phase space extrapolation over the unmeasured regions could not be made. It was suggested that part of the 3NA strength is due to 2NA+pd FSI, causing the non-phase space behavior of the polar angle.

Results published to date by Breuer *et al.* at PSI have concentrated mainly on 2NA absorption. Unlike the other experiments, Breuer *et al.* correct their QDA cross sections for the amount of FSI which they expect to have occurred. They compared the results obtained from a distorted wave impulse approximation code (DWIA) with the distortions turned on and off to estimate the effect of FSI. They claim that the correction factor for these events is about 30%. In order to make a direct comparison with other measurements, which do not apply an FSI correction, their uncorrected 2NA cross sections are shown in Figure 2-7.

The 2NA results of Breuer *et al.* appear to be lower than the result obtained by Steinacher *et al.* [56]. The Steinacher group reports a cross section of 36.9 ± 8.9mb at 120 MeV while the Breuer group reports a value of 24.5 ± 2.5mb at 114 MeV. The difference in beam energy should correspond to only about a 3% difference, while the difference between the 2 measurements is roughly 1/3. Steinacher *et al.* use a Legendre polynomial fit to determine the integrated cross section, while Breuer *et al.* use a Monte Carlo to determine the total 2N cross section. Differences in the two results may be due to the method used for extrapolation. The exclusion of an A_4 term in the Steinacher results is a possible source of error although the magnitude of the A_4 is expected to be small at this energy. This omission should also increase the disagreement as leaving out the A_4 in the parameterization tends to result in a larger measured cross section. Another possible source of error in these measurements is the reliance on the form of spectator distribution used for the extrapolation over unmeasured phase space.

A breakup of absorption on ^4He into channels is reported by Adimi [57] at 114 MeV. The magnitudes for the competing channels, aside from the discrepancy on the magnitude of the 2N total cross section, shows general agreement with the Steinacher results (see Table 2.1).

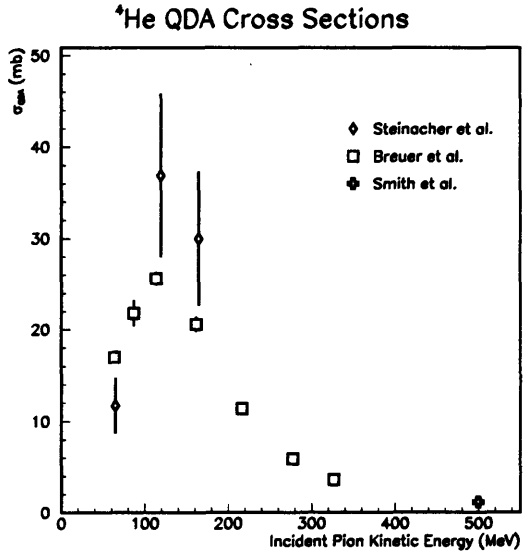

Figure 2-7: Quasi-deuteron absorption cross sections on ^{4}He.

Absorption Channel	Steinacher (120 MeV) (mb)	Adimi (114 MeV) (mb)
(pp) pn or d	36.9 ± 8.9	23.61 ± 1.93
(ppp)n	2.1 ± 0.4	2.35 ± 0.40
(ppn)n	4.4 ± 1.1	2.38 ± 1.57
(pppn)	0.5 ± 0.13	0.0
(ppd)	3.2 ± 0.5	3.24 ± 0.51
(pd)p	1.49 ± 0.22	1.56 ± 0.14
other	≤ 4.2	9.1
Total	52.7 ± 9.0	42.23 ± 2.71

Table 2.1: Previous measurements of the breakup of the absorption cross section. The other channels in Steinacher include contributions from T=1 absorption, soft-FSI final states, and the ^{3}He p final state. The other channel results of Adimi come primarily from events attributed to soft-FSI.

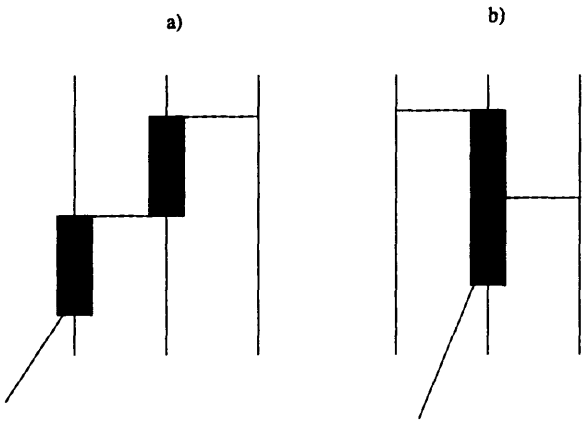

Figure 2-8: Diagrams of multi-nucleon absorption processes calculated by Oset *et al.*

The present state of experimental knowledge of pion absorption on ^{4}He is far from complete. The energy dependence of the total absorption cross section is not known with great quantitative precision and there is some controversy as to the magnitude of the 2NA contribution to the total cross section. The importance of multi-nucleon absorption on ^{4}He cannot be determined unless good measurements of the total absorption cross section are made. Furthermore, large solid angle studies with measurements out of plane are needed to better understand the characteristics of the 3NA mechanism. The magnitude of the contribution of four-nucleon processes to the total cross section is still uncertain. A substantial contribution could explain the observed rise in the cross section from ^{3}He to ^{4}He. With the exception of the Adimi results, previous searches for multi-nucleon absorption have covered a very small amount of phase space. Furthermore, there have been no out-of-plane measurements to date.

2.6 Theoretical Approaches to Multi-Nucleon Absorption

The theoretical description of multi-nucleon pion absorption is currently in the very early stages, and the efforts to date have concentrated almost exclusively on the prediction of the magnitude of the cross section. Most of the current approaches to the problem treat pion absorption as a sequential process. In the model of Oset, Futami and Toki, which is conducted in the Δ-hole framework, the graphs presented in Figure 2-8 are considered [74]. While the cross section

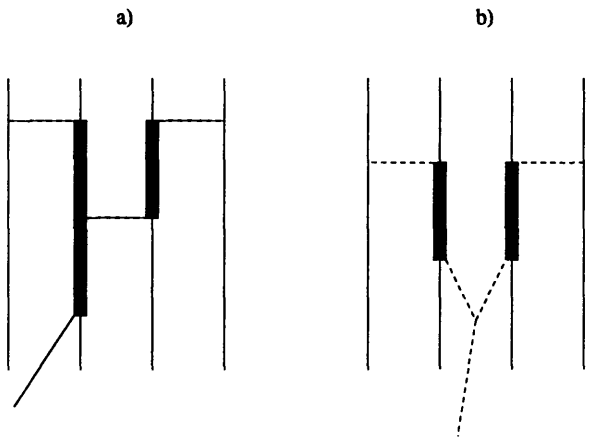

Figure 2-9: Diagrams of possible double-Δ mechanisms.

has the correct order of magnitude, the predicted energy dependence does not appear to be consistent with the data.

Brown *et al.* have proposed another type of sequential absorption process: double-Δ formation which results in the emission of four nucleons [75]. In this picture, the incident pion excites a Δ, which excites another Δ. Each of these Δs then de-excites in the same manner as the single Δ in conventional Δ-hole calculations (Figure 2-9). The cross section for this process is predicted to be of the same order of magnitude as the 2N process. Because the Δs would be far off mass shell it has been suggested that double-Δ absorption would result in phase-space flat distributions [12]. An alternative explanation is that pion absorption can occur as an entirely new "one-step" process in which more than two nucleons are involved in a coherent manner. Ashery for example, proposes that three-nucleon pion absorption is a "one-step" process which proceeds through a (πNN) resonance. Such a resonance has been looked for, but has not been found.

Some recent phenomenological work on pion absorption in light nuclei lends support to the idea that three-nucleon absorption is a coherent one-step process [76, 77, 78]. Beginning with the simple assumption that the three nucleons participate coherently in the absorption, the authors obtain good agreement with the observed branching ratios for the various multi-nucleon channels in terms of isospin. The ratios predicted by this model agree with the measured values of the various reaction channels in ^{3}He and ^{4}He (see Table 2.2) as well as in the lithium isotopes. Using the same assumptions, the observed energy dependence of the 3NA cross sections on ^{3}He and ^{3}H are correctly predicted (see Figure 2-10).

Ratio	Model	Experiment
$\frac{\sigma(\pi^+ {}^4\text{He}\to(\text{dp})\text{p})}{\sigma(\pi^- {}^4\text{He}\to(\text{dn})\text{n})}$	$\frac{\lvert F_{1/2}\rvert^2}{\lvert F_{1/2}\rvert^2} = 1.0$	120 MeV $\Rightarrow 0.99 \pm 0.22$
$\frac{\sigma(\pi^+ {}^4\text{He}\to(\text{ppp})\text{n})}{\sigma(\pi^+ {}^4\text{He}\to(\text{ppn})\text{p})}$	$\frac{\frac{3}{4}\lvert F_{3/2}\rvert^2}{\frac{1}{4}\lvert F_{3/2}\rvert^2+\lvert F_{1/2}\rvert^2} = 0.60$	120 MeV $\Rightarrow 0.48 \pm 0.15$
$\frac{\sigma(\pi^+ {}^3\text{He}\to\text{ppp})}{\sigma(\pi^+ {}^4\text{He}\to(\text{ppp})\text{n})}$	$\frac{\lvert F_{3/2}\rvert^2}{\frac{3}{4}\lvert F_{3/2}\rvert^2} = 1.33$	120 MeV $\Rightarrow 2.1 \pm 0.5$ 165 MeV $\Rightarrow 1.3 \pm 0.3$
$\frac{\sigma(\pi^- {}^3\text{He}\to\text{dn})}{\sigma(\pi^- {}^4\text{He}\to(\text{dn})\text{n})}$	$\frac{\frac{2}{3}\lvert F_{1/2}\rvert^2}{\lvert F_{1/2}\rvert^2} = 0.67$	120 MeV $\Rightarrow 0.5 \pm 0.2$

Table 2.2: Comparison of Model with Experiment for ^{3}He and ^{4}He. From Reference [76].

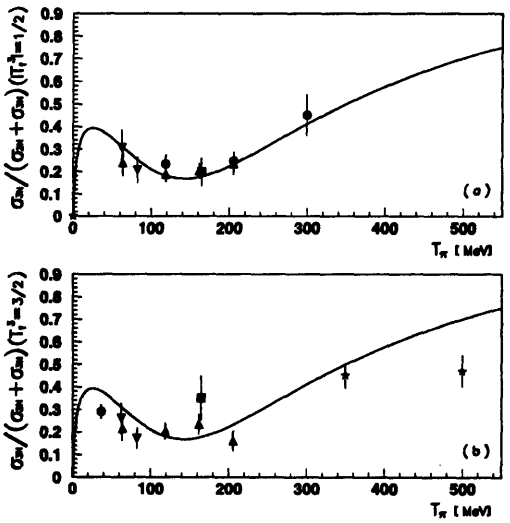

Figure 2-10: Ratio of three nucleon absorption to total as calculated by the statistical model of pion absorption. From Reference [77].

2.7 Conclusion

Although the main contribution to pion absorption in ^{3}He and ^{4}He may be attributed to two-nucleon absorption of the quasi-deuteron type, there appears to be a significant contribution from multi-nucleon processes. Experiments to date have not found evidence for hard-FSI. There are, however, signs that ISI may be an important effect in absorption on the helium nuclei, particularly above the resonance.

The application of the Δ-hole model to predict the total absorption cross section from an analysis of elastic π-^{4}He scattering agrees with the data to the level at which the data are believable. This agreement suggests that the most important source of inelasticity in the ΔN interaction arises from the coupling to the pion absorption channel. Although the OTL calculation has some difficulties in describing the data, it is clear from its results that the total pion absorption cross section on ^{4}He cannot arise solely from a π-2N absorption process. The OTL calculation has success in matching the high energy single-arm inclusive proton spectra. This success, coupled with the underestimation of the total absorption cross section, are only compatible if there is a mechanism of significant strength which does not populate the high energy region.

The total absorption cross section appears to change drastically from ^{3}He to ^{4}He, while the 2N component of absorption on ^{3}He seems to scale to first order by the isospin ratio of 1.5 to the deuterium number. One might argue that the reason for this near agreement with isospin scaling results from the cancellation of competing density and shadowing effects. Density and shadowing effects on ^{4}He should be comparable in magnitude to those on ^{3}He. Hence, one might expect that the cross section for the 2N component of ^{4}He should roughly scale by a factor of 3 over the deuterium cross section. If one believes the existing measurements of the total absorption cross section, this leaves a substantial fraction of the total absorption cross section unexplained.

The results of Mazutani and Yazaki point to the possibility that the missing cross section is due to processes in which there is an initial scatter before absorption. This would explain the missing cross section in terms of an initial state interaction. This interpretation is consistent with the fact that at higher energies the inelastic cross section is rising while that of absorption is falling. It is, however, in apparent contradiction with the agreement of the Δ-hole calculation with the total which implies that the major source of the inelasticity from the elastic channel is in the absorption channel.

Microscopic theoretical models based of multi-nucleon absorption have not yet shown great promise in providing a better understanding of the absorption mechanism. They have concentrated on predicting total cross sections and have not provided any guidance as to what one should expect in differential distributions. The agreement of recent phenomenological attempts to describe three nucleon pion absorption based on the assumption that the absorption occurs as a one step process may be indicating that the processes we are dealing with are coherent in nature, and not simply the sum of several sequential incoherent steps.

Chapter 3

Experimental Apparatus and Data Acquisition

3.1 Introduction

The Large Acceptance Detector System (LADS) was built and operated at the Paul Scherrer Institute (PSI), Villigen, Switzerland. The LADS detector was constructed in order to study multi-nucleon pion absorption in the Δ resonance region. In order to study multi-nucleon final states, it is imperative that one covers a large amount of solid angle at high granularity, has a low threshold for the detection of protons, and has the ability to separate pions from heavier charged particles. The LADS detector was designed with these requirements in mind. The detector consists of a 28 sector ΔE-E-E cylindrical plastic scintillator array concentric about the beam axis, with cylindrical wire chambers for particle tracking. Both ends of the cylinder are closed off by annular 14 sector endcaps which have holes to allow the pion beam to enter and exit the detector.

Experiments were conducted using the LADS detector in 1991 and in 1993. Data were taken on ^{2}H, ^{3}He, ^{4}He, nitrogen, argon, and xenon at several energies in the Δ resonance region. Table 3.1 summarizes the data taken with the LADS detector.

The characteristics of the LADS detector are summarized below in Table 3.2. The LADS detector has been described elsewhere in great detail [79, 26, 80]. This thesis briefly describes the major components of the detector.

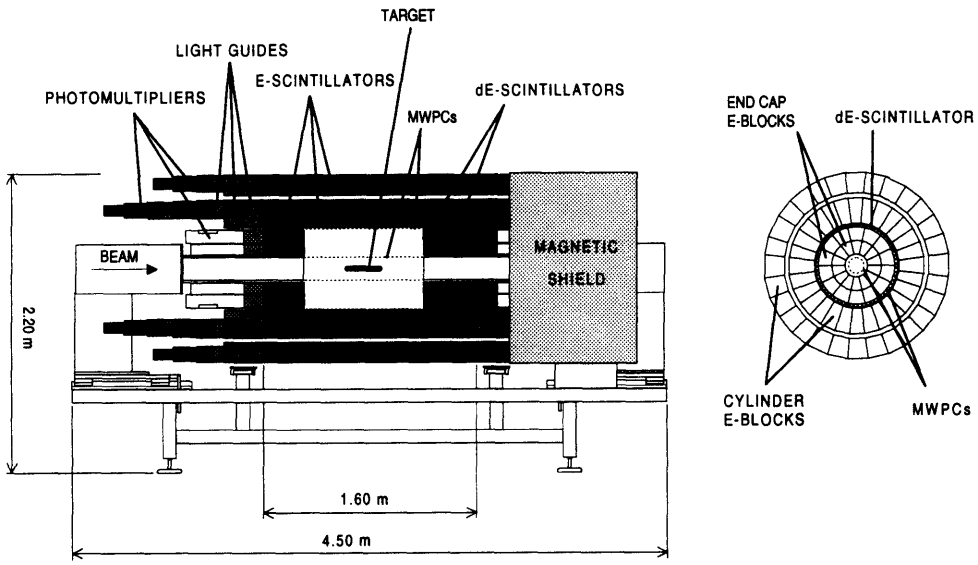

Figure 3-1: A scale drawing of the LADS detector. From Reference [61].

Target	70 MeV	118 MeV	164 MeV	239 MeV	330 MeV
^{2}H	1993	1991	1991,1993	1991	1993
^{3}He	1993	1991	1991	1991	1993
^{4}He	1993	1991	1991,1993	1991	1993
N	1993	1991	1991,1993	1991	1993
Ar	1993	1991	1991,1993	1991	1993
Xe	-	1993	1993	1993	-

Table 3.1: Summary of data on pion absorption taken with the LADS detector.

Solid Angle Acceptance	98 % of 4 π
Proton Energy Threshold	$<$ 20 MeV
Proton Energy Resolution	3 %
Angular Resolution for Charged Particles	10 mr
Angular Resolution for Neutrons	250 mr
Neutron Detection Efficiency	40 %

Table 3.2: Performance Capabilities of the LADS detector.

3.2 The πM1 channel

The LADS experiments were performed in PSI's high precision pion channel πM1. The πM1 channel has a momentum acceptance of $\Delta p/p$ of roughly 5%. It produces a pencil beam with a beam spot of 1.5 cm^2. The pion source for the πM1 channel is a beam of 590 MeV protons of intensity 600-1000 μA incident on a rotating beryllium production target, which is inclined at an angle of 22.5° to the primary beam, creating pions. After leaving the production target, particles pass through a two meter long electrostatic separator which removes protons from the beam. The beam line consists of 9 quadrupole magnets for steering, an array of slits, and two identical dipole bending magnets for momentum selection. The desired beam momentum is selected by applying the proper voltages to the bending magnets. A hodoscope, consisting of a 64 element plastic scintillator array, is placed at the intermediate focus to measure the pion momentum. The hodoscope also serves to eliminate events in which more than one pion comes down the beam pipe by allowing one to veto on events with double hits. The beam line is pictured in Figure 3-2. A more detailed discussion of the performance characteristics of the πM1 channel may be found elsewhere [81, 82].

3.3 Beam Monitoring and Definition

Signals from several detector elements are used to define the beam, the objective being a pencil beam focused on the center of the target axis (see Figure 3-3). After leaving the beam pipe, the pions pass through a beam profile monitor which measures the location and size of the beam. They then must pass through a small hole in a lead veto wall. The veto wall consists of 200 mm of lead and four overlapping 10 mm plastic scintillators, two upstream of the lead (VWU_1 and VWU_2), and two downstream of the lead (VWD_1 and VWD_2). Signals from these counters are used to veto events. The lead wall is useful for reducing background from protons and from the μ-halo resulting from pion decay. A thin plastic scintillator called the S_{time} counter is located directly downstream of the hole in the veto wall. The S_{time} counter is used to eliminate events in which there are multiple pions in the beam burst. Low and high discriminator levels, $S_{timelow}$ and $S_{timehigh}$, are set around the single pion band in order to eliminate events with protons, electrons, and multiple pions. The S_{time} counter signal is also used as the reference point for timing in LADS.

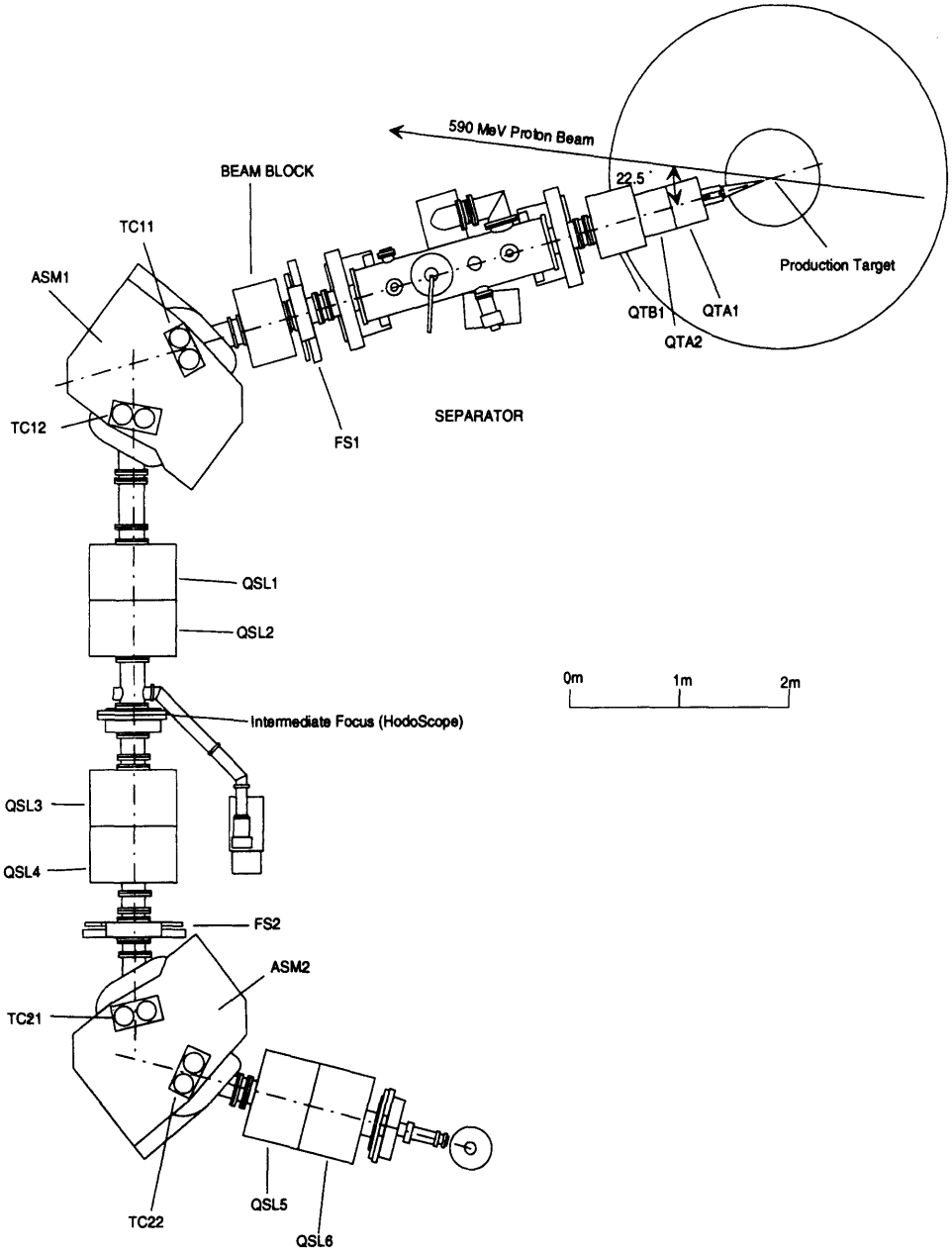

Figure 3-2: A scale drawing of the πM1 channel.

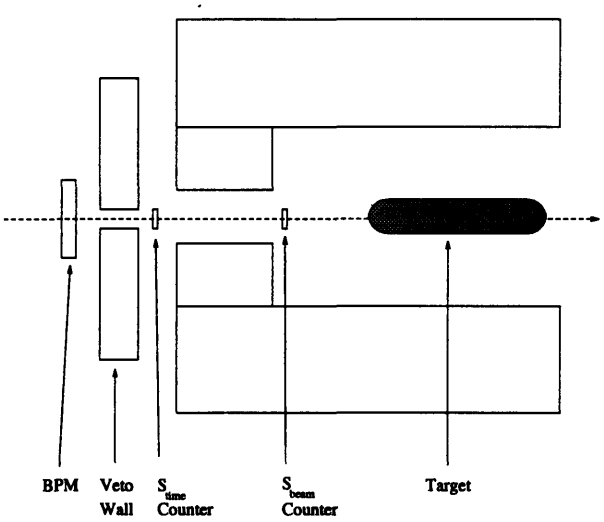

Figure 3-3: Schematic representation of beam counter detector elements.

After passing through the S_{time} counter, pions enter the LADS detector through the hole in the upstream endcap. They then pass through another scintillating counter S_{beam} located 40 cm upstream of the target. This counter has a diameter of 20 mm, which is much smaller than the 40 mm diameter of the target cell to help ensure that pions passing through it would hit the target. There are additional veto counters on the sides of the upstream and downstream endcaps which are closest to the beam axis.

The signals used to define the beam are the 50 MHz accelerator RF which signals the proton beam bursts, the hodoscope, S_{time} and S_{beam}, and the veto wall. There is an additional requirement that no pion beam burst occurs 60 ns before or after the beam burst under consideration because the lifetime of an event in the LADS detector with a slow neutron can be as long as 50 ns. The logical beam consists of the coincidence of the RF signal, the hodoscope, the S_{time}counter, the $\overline{S_{tbig}}$ signal, the S_{beam} signal, and non-vetos by the early-late electronics, and the veto wall. Typical beam rates during the experiment were 10 kHz.

3.4 Target

A gas target system was chosen for the LADS detector because of the desire to perform experiments on the helium isotopes. A cryogenic system for liquid helium would be awkward to

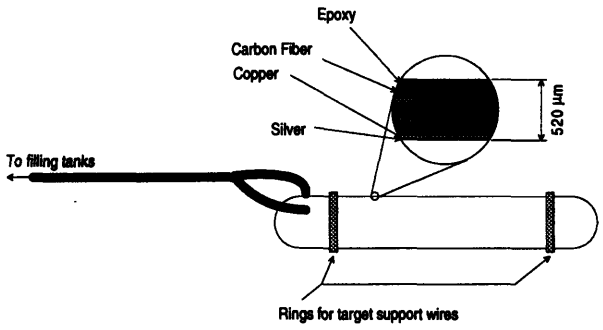

Figure 3-4: A schematic diagram of the target. From Reference [84].

accommodate under the geometrical constraints set by the geometry of the rest of the LADS detector. The gases are maintained at a high pressure to increase the density of target scatterers in the target to a range comparable to liquid helium targets. The containing walls of the target are made thin to minimize energy loss and multiple scattering effects. Two gas targets were manufactured for the LADS collaboration by Dornier [83]. The targets are 25.7 cm long cylinders with a 4 cm diameter and closed off by rounded endcaps. They are made of three layers of carbon epoxy fiber sandwiches with a total thickness of 50 microns, and lined on the inside by a 20 micron layer of copper and a 10 micron layer of silver. The targets can withstand pressures of over 100 bar.

3.5 Plastic Scintillators

The cylinder portion of the LADS detector is formed out of 3 concentric layers of plastic detector telescope. The plastic scintillator chosen for the detector is Bicron BC-408 [85]. It was chosen for its relatively low cost and good detection efficiency for neutrons. It also has a much faster response time than organic scintillator, with a decay time of 2.4 ns. The scintillator layers are the ΔE counters (CD), the inner E blocks (CI), and the outer E blocks (CO). Each cylindrical layer is formed out of 28 identical trapezoidal counters, each of which is 160 cm in length, and wrapped by aluminum foil to prevent light leakage. The scintillator blocks are packed tightly together to minimize losses which could occur by particles passing through gaps.

Each counter is connected to photomultipliers via light guides at each end. The light guides are designed to give uniform light collection independent of the position at which the particle

entered the scintillator. By reading out the signal at both ends, one is able to determine both the amount of energy deposited in the scintillator and the position at which the energy deposit occurred along the cylinder. The CD counters are 5 mm thick and allow one to discriminate between neutral particles and charged particles as the likelihood of a neutral particle triggering the CD counter is very small. The CD counters also allow one to identify charged particles through the Bethe-Bloch equation by the dE/dX *vs.* E method. The CI counters and the CO counters have thicknesses of 200 mm and 150 mm respectively. They are separated by a 30 mm wide radial gap which was left so that other devices could be inserted in the future. The cylinder counters are thick enough to stop perpendicularly incident protons with a kinetic energy of 250 MeV.

Endcap detectors are used to cover as much of the solid angle missed by the cylinder counters as possible. The endcap detectors are inserted on moveable rails into the holes at the upstream and downstream ends of the detector. The endcaps have holes in them to allow the beam to pass through and for the insertion of the inner chamber. The endcap detectors consist of 14 inner block counters (EI) and 14 outer block counters (EO), whose front faces are covered by thin ΔE counters (ED). The ED counters are 5 mm thick, and rotated half a sector from the thick counters to effectively double the achievable granularity. The ED counters serve the same particle identification functions as the CD counters. The downstream endcaps are thicker than the upstream endcaps because more stopping power is needed for forward going particles than backward going particles. There are also thin 5 mm veto counters mounted on the faces of the EI counters to reject pion beam background. Unlike the cylinder counters, the endcap detectors are read out only from one end. Thus the timing information from these counters is less accurate than that achievable with the cylinder counters.

3.6 Multi-Wire Proportional Chambers (MWPCs)

The purpose of the multi-wire proportional chambers is to track final state charged particles passing through the LADS detector. During the 1991 run, two wire chambers were used, an outer wire chamber, whose anode plane radius was 27.5 cm, and a small inner chamber, with an anode plane radius of 6.4 cm. In 1993 the inner chamber was replaced with a double chamber which had anode planes of 6.4 and 5.3 cm diameters respectively. The design of each of the chambers is similar.

	Outer Chamber	1991 Inner Chamber	1993 Inner Chamber
Anode Diameter (mm)	560	128	128/112
Number of Wires	832	192	176/144
Wire Separation (mm)	2.115	2.094	2.285/2.444
Number of Cathode Channels	560	384	384/384
Width of Cathode Strips (mm) (including .6 mm gap)	4.40	3.30	3.81,3.98/3.83,3.10
Strip angle inner/outer (deg.)	45.86/44.21	34.25/41.19	23.96,19.74/14.50,24.61
Anode Cathode Gap (mm)	4	3	3/3
Chamber Thickness (mg/cm^2)	57.2	47.2	74.2
Anode HV (+V)	2800	2350	2300/2200

Table 3.3: Summary of chamber characteristics.

The anode planes consist of gold plated 20 micron diameter tungsten-rhenium wires which are stretched with a tension of 0.6 N. The distance between the wires on each chamber is a little more than 2 mm, and each wire is positioned to an accuracy of 50 microns.

Each chamber has two cathode planes which are made from mylar sputtered with aluminum. These foils are etched with .6 mm diagonals to form individual cathode strips. For the first two chambers this was done using a dental drill mounted on a computer driven plotter. For the new inner chambers the cathode strips were etched using a thin thread soaked in a base. The mylar films are glued with araldit to sheets of rohacell which are formed into cylinders and glued together. The rohacell skeleton provides support and strength for the cathode planes. The external surfaces of the chambers are covered with aluminized Kapton which served as grounding planes. Important chamber characteristics are listed in Table 3.3.

The anode wires are read out using the CAMAC LeCroy PCOS III system [86]. The anode signals are individually amplified and discriminated to produce a logical signal, delayed until a trigger decision has been made, and then read in using a LeCroy 4299 data bus interface.

The cathode readout is accomplished with current sensitive preamplifiers which are mounted near the detector, 50 m of twisted pair cable to provide delay, PSI built postamplifiers, and CAMAC ADCs. For the 1993 run the CAMAC ADC modules were replaced by FASTBUS ADCs.

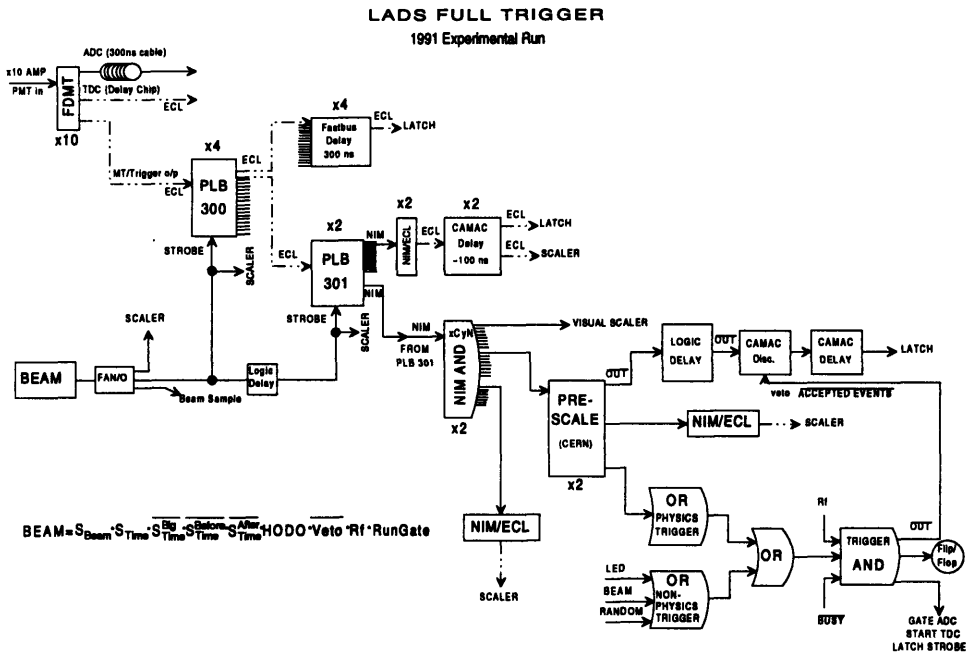

Figure 3-5: A schematic of the trigger. From Reference [84].

3.7 Trigger

The electronics for the experiment perform two distinct functions. The first is to provide the ADCs and the TDCs with stable, good resolution signals over a dynamic range of 400. The second is to provide a fast and flexible trigger. Signals from the photomultipliers are passed through fast $\times 10$ amplifiers so that the anode voltage on the tubes can be kept low to maintain gain stability. These signals are then passed into special FASTBUS modules constructed at PSI (FDMTs). Low frequency noise $\simeq$ 1 kHz is filtered out by a feedback circuit at the input of the FDMTs. The FDMTs contain both a logical and an analog section. The threshold for the logical section is set at 15 mV with $\pm$ 3 mV channel to channel variation. The logic signals from the FDMTs are fed into the trigger electronics, and after a 300 ns delay, to the TDCs and pattern units. The analog output of the FDMTs are amplified to match the ADC range, delayed by 300 ns, and then AC-coupled at the input to the ADCs to remove ground loop noise.

The trigger decision is based on a determination of the charged and neutral particle multiplicity of an event. The logical outputs from the FDMTs are fed into PLB 300s which contain hard wired Programmable Array Logic (PAL) chips. The PLB 300s determine which sectors

are hit and whether the particle which hit are charged or neutral. The charge/neutral determination is made on the basis of whether or not a ΔE counter fires. Charged and neutral particles in the cylinder are defined as follows:

$$C(i) = \Delta E(i) \tag{3.1}$$

$$N(i) = \overline{\Delta E(i)} \cdot (E_{in}(i).\mathrm{OR}.E_{out}(i)) \tag{3.2}$$

The identification of neutral particles is more complicated in the endcap because of the half sector staggering of the ΔE counters with respect to the E blocks. Charged and neutral events in the endcap are defined as follows:

$$C(j) = \Delta E(j) \tag{3.3}$$

$$N(j) = [\overline{(\Delta E(j).\mathrm{OR}.\Delta E(j+1))}.\mathrm{OR}.(E_{in}(j{+}1).\mathrm{OR}.E_{out}(j{+}1))]\cdot(E_{in}(j).\mathrm{OR}.E_{out}(j{+}1)) \tag{3.4}$$

where $\Delta E(j)$ is the counter which covers the E block counters j and $j+1$.

The outputs from the PLB 300s are fed into PLB 301s which have memory look up tables to determine the multiplicities of charged and neutral hits. The PLB 300s and 301s are strobed by the logical beam. From the PLB 301s, the following exclusive trigger types are created using NIM electronics:

- $0C1N$
- $0C \geq 2N$
- $1C0N$
- $1C1N$
- $1C \geq 2N$
- $2C0N$
- $2C \geq 1N$
- $\geq 3C$

These trigger types are pre-scaled to desired values to emphasize trigger types of physics interest and to suppress the large background from uninteresting channels. For example, the $\geq 3C$ trigger is not prescaled down, as this channel has a high contribution from absorption events relative to background. The $1CON$ trigger, on the other hand, consists primarily of elastic pion scattering events, so this trigger is heavily prescaled down. These eight event types comprise the "physics" triggers. Non-physics triggers, such as LED events, ring counter events, RF events, and random BEAM events are ORed with the physics triggers to gate the event readout.

3.8 Data Acquisition

Data acquisition for LADS is accomplished with various FASTBUS, CAMAC, and VME modules, DEC workstations, and EXABYTE tape drives. A schematic of the DAQ system during the 1991 run is shown in Figure 3-6. During the 1991 run, the analog signals were read into CAMAC ADCs which were then converted into the FASTBUS standard. The signals were bundled into an event format and then sent to the data memory of a μVAX 3200, from which it was written to tape. For the 1993 run, the CAMAC ADCs were largely replaced by FASTBUS ADCs, with CAMAC being retained only for the PCOS MWPC anode readout. The μVAX 3200 was replaced by a VaxStation 4000-90. Other VaxStations were attached to the data stream for monitoring and online analysis purposes.

The average event size was 600 bytes. The typical rate at which events were written to tape was around 200 events/s during the 1991 run and 500 events/s during the 1993 run. Approximately 200 2.5-Gbyte tapes of data were taken in 1991, and 200 5.0-Gbyte tapes in 1993.

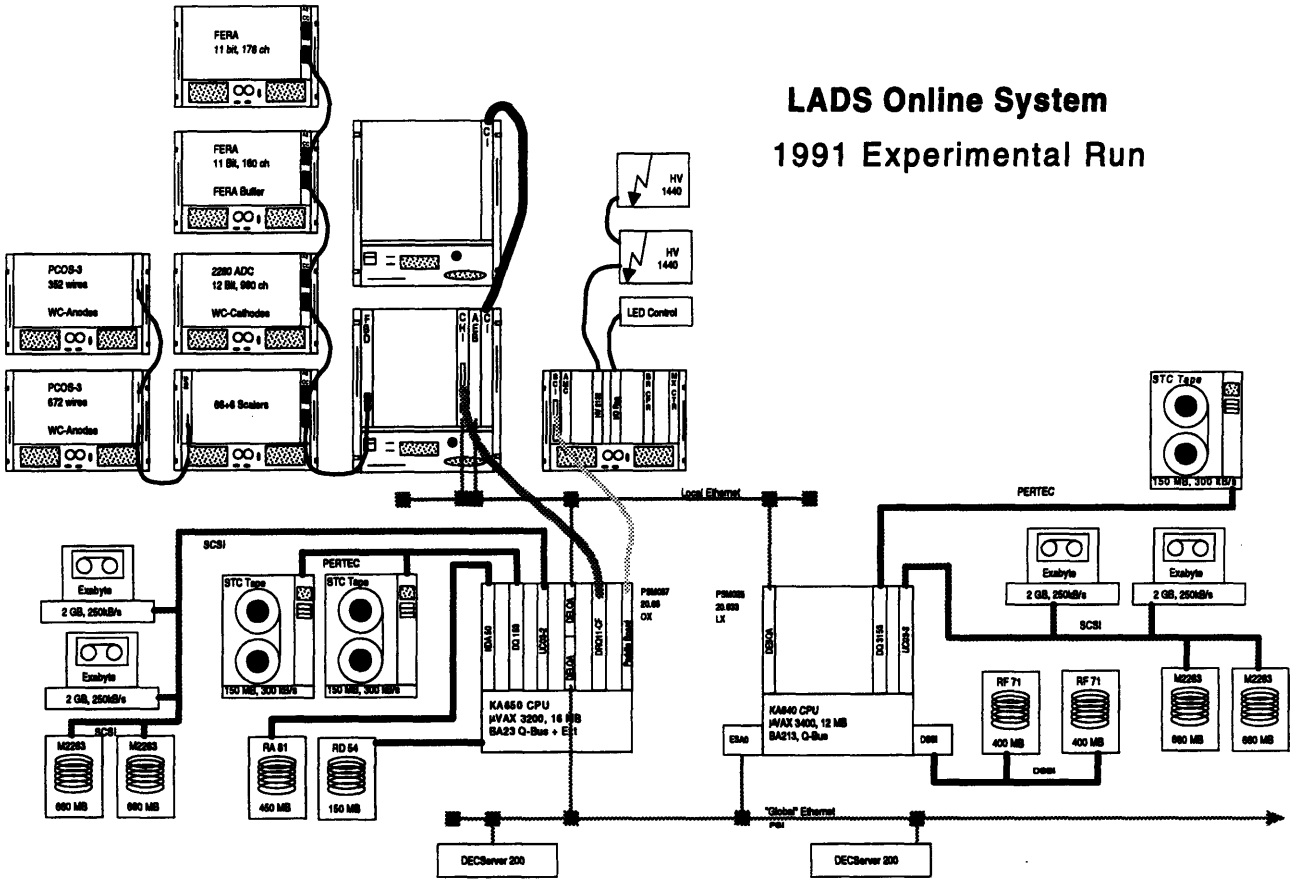

Figure 3-6: A schematic representation of the 1991 data acquisition setup.

Chapter 4

LADS Analysis Tools and Calibration

4.1 Introduction

In this chapter the LADS software analysis package is briefly described. The calibration procedure is outlined and the detector performance is discussed. The GEANT based LADS Monte Carlo is also described [87].

4.2 LADYBIRD and LARK

The LADS analysis system was developed as a versatile software tool capable of handling both online and offline analysis requirements. It runs in a VMS environment on both the VAX and ALPHA architectures. Its functionality includes the processing of raw counter information, the construction of particles, the tracking of the particles through the detector, the identification and energy determination for particles, and the calculation of kinematical quantities. It is a system with much built-in flexibility and the behavior of the analyzer can be changed during runtime by setting various switches. The system also allows one to write tests and histogram various quantities of interest interactively.

The analyzing package consists of two main components, LADYBIRD, which performs the actual calculations, and LARK, which serves as an interface between the user and LADYBIRD.

During online processing, LADYBIRD samples the data stream being written to tape and allows one to monitor the performance of the various counters which make up the LADS detector. Offline, LADYBIRD reads the data event by event from the 8mm tapes. Another standalone program called FINDER also samples the data stream during the run, and allows one to detect changes in the performance of the various counters. A third program, HYSTORIAN, monitors the stability of the counters over time, and keeps a continuous log of various quantities of interest during the run.

There is a large body of code which forms the infrastructure of the analyzer. These routines handle such tasks as the communication between the various processes involved and the transfer of data between global memory locations. This portion of the analyzer is not discussed. Instead, the focus here is on the portions of the analyzer which are directly related to the production of physics results. The steps which are taken in processing an event is described in the next sections and shown in Figure 4-1.

4.2.1 Preparation of Raw Data

The data which are written to tape are first copied into a common memory location which is accessible to the various routines. Any cabling mistakes which were made during the run are corrected, and consistency checks are made to verify that the various pieces of hardware were performing properly. The consistency checks include such things as the comparison of scintillator latches with the actual multiplicity of counters that fired and verification that the trigger is functioning properly.

In the next step, raw scintillator signals are converted into calibrated values. Before proceeding further, full information is required from the counter in question. Full information means that each ADC and TDC which should have fired did indeed register a signal. For example, in the case of a cylinder counter, four separate signals must fire, (the upstream and downstream ADCs and TDCs). If full information is unavailable, the counter is ignored.

The raw TDC signals are converted into nanosecond values. For the cylinder counters, a mean time is calculated for the later determination of the time of flight of the particle. This is not necessary for the endcaps, which have only one TDC per counter. The raw ADC values are converted into calibrated values via a linear transformation, and in the case of cylinder counters, the geometric mean of the upstream and downstream counters is used to determine

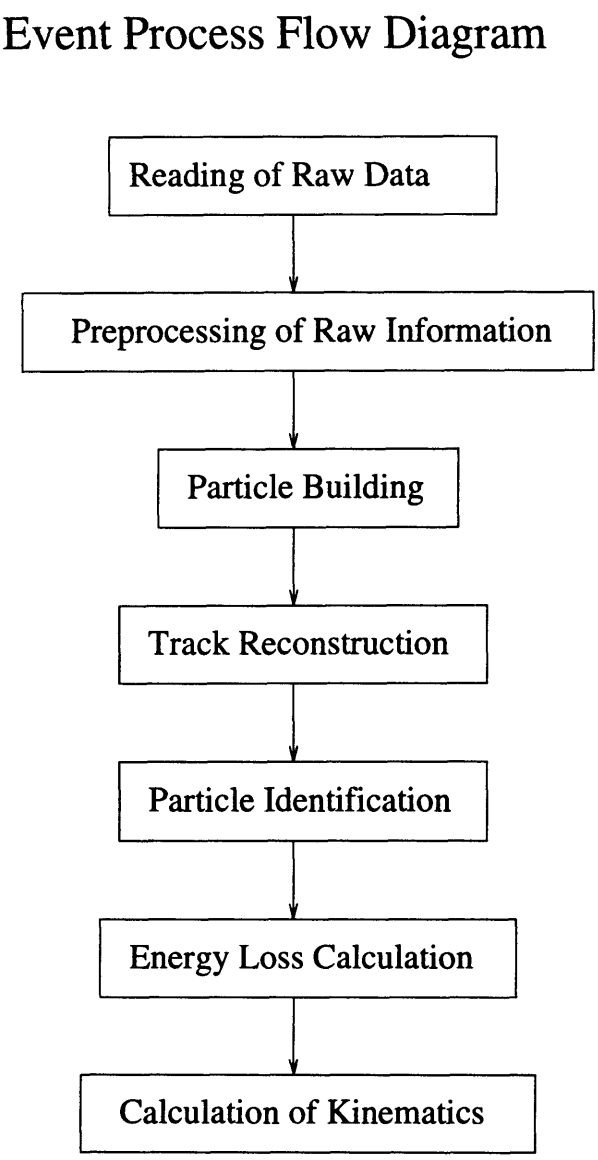

Figure 4-1: A schematic depicting the steps taken in analyzing an event.

the light deposited by the particle. At this point the plastic information has been aggregated to the counter level, and one can begin to combine the counter information into particles.

The raw chamber information which is used to determine the trajectories of the particles are the ADC values of cathode strips on each of the cathode planes and the wire numbers of the anodes which fired for a given event. In the first step, the dead cathode strips are filled by interpolating from the values registered in neighboring strips. After dead regions have been filled, the code iterates through each of the cathode planes looking for peaks which correspond to charge left by the ionizing particle that are above a certain threshold. If too many peaks are found (greater than 4) on a given cathode plane, the threshold is increased and the peak search process is repeated.

Once the peaks have been identified on the cathode planes, the possible permutations of matches between the inner and outer cathode planes are compared to determine which permutation is optimal. Peaks on cathode planes are matched and the corresponding ϕ and z positions are calculated. An added complication is that on the outer chamber and the old inner chambers there are two possible crossings for each cathode pair. The ϕ positions of the cathode pair are compared to the ϕ positions of the wires. If a wire has fired, the pairing is chosen as a correct match. If both possibilities match a wire fire, both positions are retained as possible chamber hit locations. The permutation which results in the largest number of associated wires is chosen as the correct permutation. If there is more than one permutation which has the largest number of wire associations, the optimal permutation is chosen by a least squares fit of the integrated strengths of the peak pairings. The assumption is that peaks formed by the same particle will have roughly the same strengths. The optimal permutations on each chamber are the locations which must be matched to particles in the track reconstruction portion of the code.

4.2.2 Building Particles

As a particle traverses the scintillator volume, it deposits energy in several counters. In a simple case, a particle may pass through a cylinder ΔE counter and then stop in the inner cylinder E block. In a more complex case, a particle may undergo a nuclear reaction in the cylinder, and as a result, its energy become spread over several counters. Particle building involves the determination of the proper association of counters with the particles responsible for the energy deposit.

In the first step, the code loops through the cylinder ΔE counters and counts each one that fires as a charged particle. It also associates the light from cylinder E block counters directly behind a ΔE counter with the same charged particle. E blocks which fire without the delta counter in front of them firing are assigned to neutral particles.

Reconstruction of particles in the endcap is somewhat more difficult because of the overlapping geometry. Charged particles are associated with each ΔE counter which fires. Endcap E blocks behind a particular ΔE are also associated with that particle. Endcap E blocks which fire without the ΔE counter firing are identified as neutral particles.

The next step in building particles is the removal of adjacent neutral particles. Particles tend to scatter when reacting in the detector and counters adjacent to the ΔE counter which the particle originally entered. This association has the deleterious effect of excluding real neutrons which come out at small opening angles with respect to a charged particle.

Particles may travel through a portion of the endcap and then stop in the cylinder counters. These particles are called punchthrough particles. They are identified by the fact that the signals which they leave in the cylinder and endcap have similar timing characteristics.

4.2.3 Track Reconstruction

Track reconstruction involves matching particles to wire chamber hits and determining the vertex position when possible. Chamber hits may be assigned to one and only one particle. Track reconstruction begins by associating the outer chamber with particles. Positions of hits in the outer wire chamber are compared with particles which have a cylinder ΔE hit. Cases in which there is only one possible match of the cylinder ΔE with a chamber hit within a certain ϕ and z tolerances are assigned first. After the unambiguous assignments are done, particles with one or more associations are assigned to particles, giving preference to those chamber hits which have a wire hit associated with them. Finally, associations between remaining outer chamber hits and particles which have not fired a cylinder Δ counter are attempted. At this point, outer chamber associations are complete.

Possible associations between inner chamber hits and particles which have an outer chamber hit are determined next. In the case of the 1993 run, associations are attempted with both inner chambers.

Tracks formed by the possible associations of the inner chamber are calculated. If the distance of closest approach between two possible tracks pass within 1 cm of each other, then the distance of closest approach is assigned as the vertex, and the two inner hits are associated to the particles. Using this vertex, the remaining inner hits are assigned by minimizing the track distances and the ϕ differences between the inner and outer hits of these associations.

If it is not possible to form a vertex, matches between inner and outer chamber hits which are one-to-one are assigned. If there is more than one match, preference is given to the non-punchthrough match. The intersection of this track with the z-axis is taken as the vertex. The correct pairing for the remaining inner chamber hits is determined by minimizing the ϕ differences between inner and outer chambers.

Next, associations between plastic hits with no assigned outer chamber hit and the inner chamber are attempted. Unambiguous matches are made first. For the 1993 wire chambers, in the case of ambiguous matches, preference is given to associations for which both inner chambers have fired. Remaining ambiguous matches are assigned by an optimization which minimizes ϕ differences.

4.2.4 Particle Identification

Both time-of-flight information and dE/dX information are considered in the determination of particle type. Particle velocities are calculated for each counter which a particle hits. In order to determine the velocity, β, of a particle accurately, the vertex of the event must be known as well as the polar angle, θ, of the particle of interest. The velocity of neutral particles is determined using the θ determined from the plastic and from the vertex of the event. The major causes of error in determination of β, assuming that the wire chamber and plastics are well calibrated, comes from corrections due to interactions occurring before the particle encounters the ΔE counter and the intrinsic timing resolution of the photomultiplier tubes. For neutral particles, the inability to determine θ to better than roughly 10 ° is the limiting factor.

The dE/dX for charged particles is calculated by dividing the light deposited in each counter by the path length traversed by the particle through the counter. The best values of β and dE/dX are chosen from all of the counters in which such a measurement is made. For the selection of β, the first counter which is hit is chosen preferentially over successive counters as this should provide the most accurate determination of the velocity. For dE/dX, precedence

is given to the endcap value over the cylinder value because of the longer flight path to the counter.

Four separate particle identification tests are used to determine particle type:

- dE/dX *vs.* E in the cylinder counters: For this test, the dE/dX of the particle in the cylinder is plotted against the total light deposited in the cylinder counters for that particle.
- TOF *vs.* E in the cylinder counters: For this test, the reduced time of flight as calculated using the cylinder ΔE is plotted versus the total amount of light deposited by that particle.
- dE/dX *vs.* E in the endcap counters: The dE/dX for this particle in the endcap ΔE is plotted against the total light deposited by that particle.
- TOF *vs.* E in the endcap counters: The reduced time of flight of the particle as calculated using the endcap ΔE is plotted against the total light deposited by that particle.

Particles which are purely in the cylinder and have deposited more than 10 MeV of light use the dE/dX *vs.* E measurement in the cylinder if this quantity is calculable. Otherwise, the cylinder TOF is used. For particles purely in the endcap, the dE/dX in the endcap method is used if more than 10 MeV of light was deposited by that particle. Otherwise, the TOF method is used. For punchthrough particles, the hierarchy is a bit more complicated. For clean punchthroughs, which have not reacted in the E block, resulting in more than one cylinder ΔE firing, the following hierarchy is used:

- If the particle has deposited more than 10 MeV of light in the cylinder and dE/dX is calculated, then this method is used.
- Otherwise, if the particle has deposited more than 10 MeV of light in all of the counters except the endcap ΔEs and the dE/dX was calculated, then this method is used.
- Next, the routine checks whether the time of flight in the endcap was calculable. If so, this method is used for particle identification
- Otherwise, the TOF in the cylinder is used.

For non-clean punchthroughs, the endcap dE/dX *vs.* E is the test with the most precedence, followed by the time of flight in the endcap, dE/dX in the cylinder, and TOF in the cylinder.

4.2.5 Determination of Energy Loss

Once the charged particle types have been determined, the vertex energy of the particle may be calculated by taking into account energy losses on the way to the scintillators. As the particles travel from the reaction point in the target gas to the plastic counters, they lose energy by ionizing the medium which they are traversing. The most important sources of energy loss are the target walls and the wire chambers. The energy loss for each particle is calculated by tracing the path of the particle through the layers of the detector which it should have traversed *en route* to the plastics. Starting from the point at which the particle hit the detector, its route is back-tracked, and the energy which it should have lost is successively calculated by looking up the energy loss from an exponential fit to the energy loss and range tables. The energy loss and range tables are different for each particle type. For particles with less than 20 MeV, more accurate determination of the energy loss is done by an interpolation from tables.

4.2.6 Calculation of Kinematic Quantities

Once the particles have been identified and their trajectories and energies determined, kinematic quantities such as invariant masses and missing momenta may be calculated. The relevant kinematic quantities to calculate are dictated largely by the number and type of particles in the final state. Specialized routines have been developed to handle the various final state configurations.

4.3 Calibration

There are two main detector families which need to be calibrated before data analysis can proceed. These are the plastic counters and the wire chambers. The calibration process is an iterative process as the calibration of wire chambers is dependent on a rough plastic calibration, and accurate plastic calibration requires particle track information.

4.3.1 Plastic Calibration

There are two major steps involved in the calibration of the plastic counters. These are known as the absolute calibration and the fine calibration. In the absolute calibration step linear

transformations of ADC values to energy are determined for each of the individual counters. The offsets for each TDC counter is also determined. The absolute calibration is done using reactions which could be kinematically determined using only wire chamber information. For deuterium, the absolute calibration is done with the reaction $\pi^+ d \rightarrow pp$. On ^{3}He, the reaction $\pi^+ {}^3\mathrm{He} \rightarrow ppp$ is used, and on ^{4}He, $\pi^+ {}^4\mathrm{He} \rightarrow ppd$. These systems are kinematically determined if one knows the particle types so a very rough initial plastic calibration is needed to proceed.

Using the polar and azimuthal angles of the particles, the vertex energy of the particles can be calculated. The particles are traced from the interaction point to the scintillator counters, with the energy losses calculated along the way. The light output at the scintillator must be corrected for saturation effects in the scintillator. The absolute gain is the ratio of the expected to measured light in the counter.

The TDC calibration of the ΔE cylinder counters is accomplished in the same way as the ADC calibration using the kinematically determined systems. The calculated time is compared to the measured time to determine the TDC offset using the formula

$$b^t_{abs} = t_{calc}/a^t_{abs} - t_{raw}. \tag{4.1}$$

Since the signals are measured on both ends of the counters, one must correct for the propagation of light in the scintillator. The calculated time is given by

$$t_{calc} = t^{up,dn}_{calc} \pm z/c_{scint} \tag{4.2}$$

where z is the point at which the particle strikes the scintillator. The TDC offsets of the E block counters are not calibrated with charged particles because of problems associated with the deceleration of the particles as they traverse the E counter and because the penetration depth of the particle is not precisely known. If charged particles are used for the TDC calibration of the E blocks, this results in a systematic offset in the energy determination for the neutrons. Instead, the kinematically complete reaction $\pi^+ {}^4\mathrm{He} \rightarrow pppn$ is used. Since the ADCs are already calibrated it is possible to use the energy information for the charged particles as well as the MWPC calculated angles to determine the energy and direction of the neutron. The neutron is assumed to interact at the center point of the counter because the neutron reaction point is distributed roughly uniformly over its flight path.

In the fine calibration step, the ADC signals are corrected for non-linearities due to geometrical and electronics effects. The light output for each counter group is calculated from

a kinematically complete measurement and compared to the measured value. A second order polynomial is fit to this correlation, greatly improving the achieved resolution. The energy resolutions achieved through the fine calibration equal the design goals specified when the LADS detector was proposed. The summed energy of the two outgoing protons following absorption on deuterium has a FWHM peak width of 2.5%, and the width of the summed energy of the three protons after absorption on ^{3}He is 3.0%.

4.3.2 Wire Chamber Calibration

There are two major steps involved in the calibration of the wire chambers. The first involves adjusting the relative positions of components within individual chambers, and the second involves the positioning of the chambers with respect to LADS. The intra-chamber positions which must be adjusted are the relative positions of the cathode strips with respect to each other and with respect to the anode wires. The origin of the chamber coordinate system (0° and $z = 0$) is defined in the software as the point where the first wire ends on the upstream edge of the chamber. It also assumes that the first inner and outer cathode strips intersect at this origin. The positions of the first physical cathode strips do not intersect with the origin so they must be moved. The correct position for the cathode strips are determined by moving them until the correct active length for the chamber is achieved.

Once the intra-chamber calibration is complete, the relative positions with respect to the rest of the chamber must be determined. This is done by exploiting the back-to-back kinematics of pion absorption on the deuteron. The chamber ϕ and z orientations are varied until the protons are 180° degrees apart in θ and ϕ. The angular resolution which has been achieved is on the order of 1° in both ϕ and θ. The resolution of the chambers is primarily determined by the number and angle of the cathode strips and the number of anode wires. The vertex resolution can be measured by measuring the distance of closest approach between two tracks. Vertex determination is done to better than 1 mm.

4.4 LADS Monte Carlo

Despite the fact that measurements using the LADS detector cover a large amount of phase space, extrapolations over unmeasured regions must still be made in order to determine total

cross sections. Particularly important in this respect are extrapolations due to the energy thresholds of the detector. The detector response to the various reaction products must be well modelled. Furthermore, event generators which reproduce the kinematical features of the data are necessary for making extrapolations over the unmeasured phase space. The models may also be useful as guides to the underlying physics behind the processes.

4.4.1 Detector Simulation

The Monte Carlo simulation of the LADS detector uses the GEANT package developed at CERN to simulate the detector response to the events thrown by the generator. The Monte Carlo simulation includes our best knowledge of the materials which comprise the detector and their spatial position. The simulation iterates each particle which was produced in the reaction through space and the various elements of the detector. Energy losses through electromagnetic and hadronic processes are included in the simulation. Positions at which particles pass through the MWPC are recorded, as is the light which is deposited in each of the scintillator counters. This information is stored in a pseudo-raw data file which is read in by LADYBIRD.

4.4.2 LADYBIRD interface

The raw Monte Carlo data are passed through the analyzer so that any software inefficiencies which affect the data will also be reflected in the Monte Carlo. The light and position information which was stored in the raw data file is converted into ADC and TDC signals which are smeared to model the detector resolution. Latch and trigger patterns are reconstructed from the pseudo-raw data. The positions of tracks through the wire chambers are smeared by a resolution and converted into hits on the anode and cathode planes. Once this is done the data are passed through the identical analysis chain which the real raw data pass through, and identical sets of histograms can be produced of any kinematic quantity of interest.

Chapter 5

Extraction of Absorption Events and Beam Normalization

The purpose of this thesis is two-fold, an accurate determination of the total pion absorption cross section, and a decomposition into the various reaction channels. This chapter describes the procedures used in the extraction of absorption events and in the determination of beam normalization. Once the absorption events have been extracted, the total absorption cross section can be determined by extrapolation over unmeasured regions of phase space.

The total absorption cross section is defined as:

$$\sigma_{abs} = \frac{N_{abs}}{N_\pi \times \rho_{target}} \times \frac{1}{\Omega} \tag{5.1}$$

where N_{abs} is the number of detected events in which there is no pion in the final state, N_π is the number of incident pions, ρ_{target} is the density of target scatterers, and Ω is the correction due to the missing acceptance and any inefficiencies in the detector. Determining the total absorption cross thus involves the accurate determination of these four quantities. This chapter addresses the determination of N_{abs}, N_π, and ρ_{target}. The determination of Ω will be the subject of the next two chapters. Several competing channels contribute to the absorption cross section. Each of these has with it an associated acceptance which is related to the kinematical distribution of the particular channel. Thus, the determination of the total absorption cross section requires a decomposition into the competing channels. The total absorption cross section

can be represented as a sum over all of the competing channels j:

$$\sigma_{abs} = \frac{1}{N_\pi \times \rho_{target}} \times \sum \frac{N^j_{abs}}{\Omega_j} \tag{5.2}$$

In order to determine N_{abs}, one must isolate the subset of events which come from the target gas, and eliminate those events in which there is a pion in the final state. The elimination of events with charged pions is relatively straightforward using the charged particle identification machinery described in the previous chapter, missing energy cuts, and invariant missing mass cuts. Events in which SCX occurred are also rejected by the missing energy and missing mass cuts. Additional suppression of SCX contamination can be accomplished by rejecting events in which a γ is detected. The predominant decay mode for neutral pions is into two γs. The detection probability for a γ passing through LADS is roughly 1/3.

5.1 Extraction of Events from the Target Region

The first step of the analysis involves the elimination of events in which the pion reaction occurs outside the target region (See Figure 5-1). Events whose z-position is not within the central 20 cm of the target are removed in this extraction. This cut eliminates background from the target endcaps, the air, and the beam defining counter. No restriction is made on the radial position of the vertex of the event because for some of the events included in the sample this quantity cannot be accurately determined.

An accurate determination of the z-position of the vertex can be made if at least one charged particle registers a hit in both the inner and outer wire chambers. In this extraction, events which do not have at least one charged particle with two wire chamber hits are excluded. Since the incident beam is π^+ in this experiment, all absorption final states must contain at least one energetic charged particle. The class of absorption events which are excluded by this cut are those in which all charged particles either travel through the beam pipe, or are stopped by the endcap after passing through only one wire chamber. The phase space for such processes is small, but must be corrected for by extrapolation.

This first extraction reduces the amount of data by roughly a factor of five. During the extraction, beam and LED events are also filtered out. The beam events are used to normalize

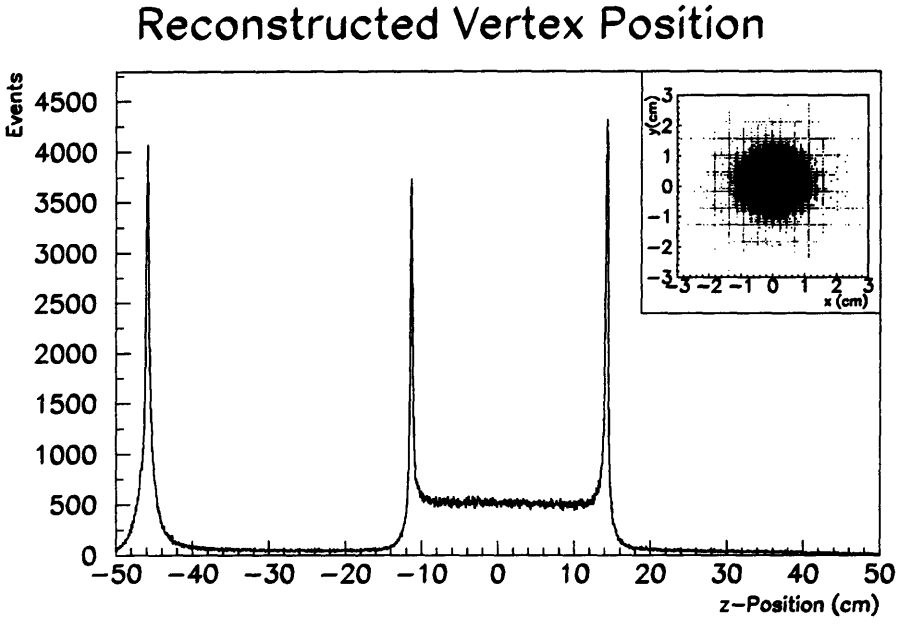

Figure 5-1: The vertex positions of events as reconstructed by the MWPCs.

the data. The LED events can be used to monitor the stability of the counters. Every twentieth event is also filtered out for normalization purposes.

5.2 Empty Target Subtraction

The contamination from events originating in the target's cylindrical wall is taken into account by an empty target subtraction. At several points during the runs, the target cylinder was evacuated, and data were taken under the same conditions as when the target was full. The contribution of events originating in the target walls is removed by subtracting the cross section measured with the target empty from the cross section measured with the target full. In the case of the 164 MeV data, the empty target cylinder was accidentally displaced slightly from its position when filled with gas. The uncertainty associated with the empty target subtraction for this case has been conservatively increased to half the size of the total correction. Since the empty target subtraction is small, this increased uncertainty does not significantly increase the overall uncertainty in the measurement at this energy.

A complication arises in making the empty target subtraction from differences in the amount of multiple scattering which occurs when the target is empty and when it is full. When the target is filled with a gas at high pressure, the incident pions have a greater probability of being deflected into the target wall than when they are traversing the evacuated target cylinder. To take this effect into account, the empty target subtraction is increased by a multiple scattering correction which has been determined to be roughly 15-20%. To determine the magnitude of the correction factor, one can analyze the beam profile upstream and downstream of the target and the amount of subtraction needed to zero the contribution from higher charged multiplicity channels arising from absorption on the higher A nuclei of the target walls [26].

To assess the uncertainty in the multiple scattering correction, other methods can be used to determine the correction factor. Events originating in the target walls are isolated by demanding that the radius of the reconstructed vertex lies between 1.9 and 2.1 cm from the z-axis. Since the target walls are much denser than the gas, events from the target gas contribute insignificantly to the counts in this region. The excess fraction in the ratio of scatters occurring between full and empty runs, across the length of the target, gives another estimate of the correction factor. The systematic uncertainty in the determination of the multiple scattering correction factor is taken to be half the size of the correction.

5.3 Density of Target Scatterers

The 20 cm target cut determines the active length of the target. Once the target length is known, the density of target scatterers is a function of the pressure of the gas and its temperature. The pressure of the gas was monitored by a high precision gas gauge, and the temperature was monitored at upstream and downstream positions and at the target by accurate thermocouple gauges. Heat produced by the photomultiplier bases caused the temperature inside the detector to be higher than the outside temperature, and the temperature registered by the three gauges varied by a few degrees. Because of these variations, the uncertainty in the measurement of the temperature is taken to be 1%. At the target pressures used in the experiment, the ideal gas law must be modified by the compressibility, which varies as a function of both the temperature and the pressure. The modified gas law has the form:

$$PV = Z(P,T)nRT \tag{5.3}$$

The compressibility factors for the gases used in the experiment are found by interpolation from tables in *Encyclopedie des Gaz* [88]. The total uncertainty in the determination of the density of target scatterers is 1%.

5.4 Beam Normalization

The number of incident pions was counted during the experiment by the beam scaler. Cuts are applied to the TDC and ADC values of the beam counter to ensure that only events in which there was a good pion on target are counted. The ADC cut removes events in which the ADC failed to fire and those in which the pion lost too much energy. The TDC cut is important for excluding events in which the pion did not pass through the beam counter. To determine the fraction of the beam excluded by the ADC and TDC cuts, events which were triggered solely by the beam counter are passed through the identical ADC and TDC gates that the real data are passed through. The uncertainty associated with this determination is statistical and depends on how much beam sample was taken during the run. During the 1991 runs, there were roughly 900 beam events taken per million physics triggers. In 1993 this was increased by a factor of ten.

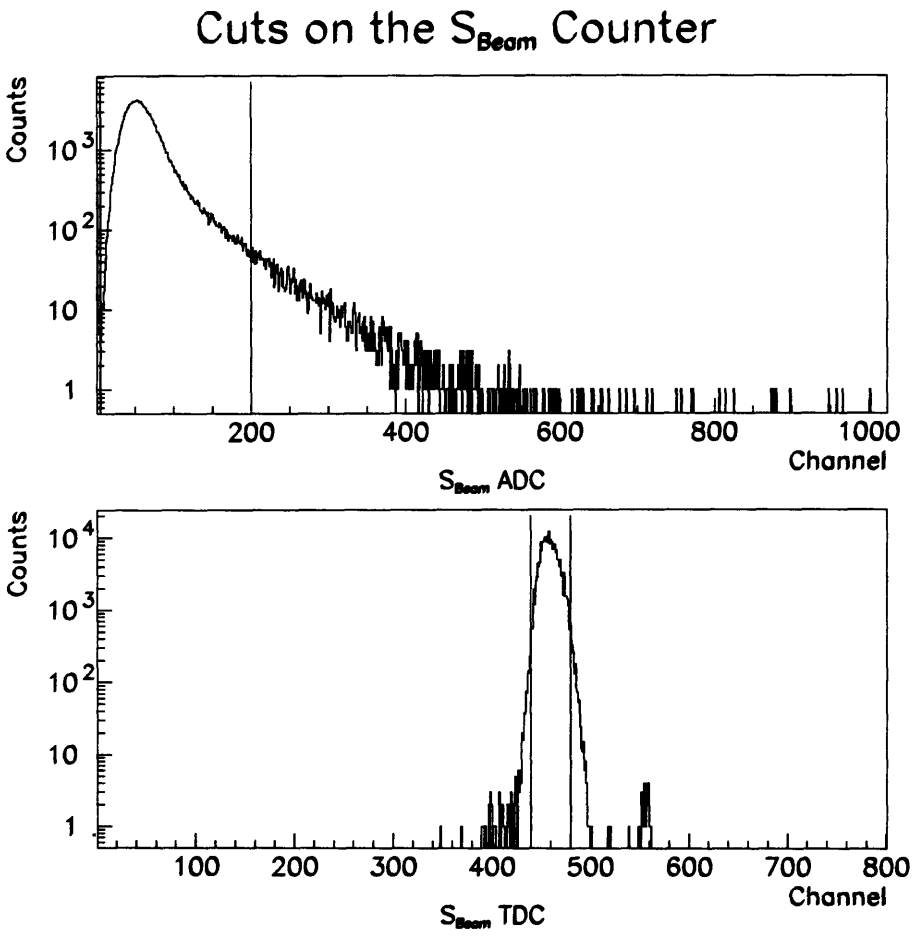

Figure 5-2: Typical cuts applied to the S_{beam} counter to ensure that only good pions were included in the sample.

The number of incident pions must be corrected for by the number which decay or react on their way from the beam counter to the target and for the number of pions which, because of their trajectory, miss the target entirely. A correction must also be made for the amount of contamination in the beam.

The percentage of the beam which decays can be calculated from the velocity of the pion, the distance it travels, and its mean lifetime by the equation:

$$N/N_0 = e^{-lm_\pi/\tau p} \tag{5.4}$$

The distance from the beam counter to the target is known to better than 5%, so that the uncertainty arising from the beam decay correction is ignorable.

The percentage of pions which react before reaching the target is calculated from the known total pion reaction cross sections for the materials which the pion passes through from the beam counter to the target gas. The uncertainties in the thickness of material from the beam counter to the target gas is known with an uncertainty of about 10%, and the total pion reaction cross sections are known to within 25%. The total error in the determination of the reaction correction is thus taken to be 30 % of the size of the correction. Since this correction is quite small the uncertainty resulting from it is also ignorable.

The percentage of muon contamination in the beam has been determined using the transport code TURTLE. The uncertainty in the determination of the muon contamination has been estimated to be about 1%.

The largest uncertainties in the beam normalization result from the correction due to the number of pions missing the target. To determine the number of events in which the pion misses the target completely due to multiple scattering and beam optics effects, pion reactions occurring in the air in front of and in back of the target are examined. Events in which a two-track vertex could be constructed and all charged particles had wire chamber information are considered. Events in which there was noise in the detector were excluded to reduce background from misreconstructions. The number of reconstructed vertices in the regions several centimeters upstream and downstream of the target are examined. The fraction of events missing the target was determined by averaging the upstream and downstream values for the ratio(see Figure 5-3):

$$R_{target} = \frac{\#\text{ Events within 2 cm of the z} - \text{axis}}{\#\text{ Events within 5 cm of the z} - \text{axis}} \tag{5.5}$$

Energy (MeV)	Beam Corrections					
	$R_{Sbeam\ cut}$	R_{contam}	R_{react}	R_{decay}	R_{miss}	R_{Total}
70	0.819	0.980	0.989	0.941	0.803	0.600 ± 0.078
118	0.925	0.980	0.982	0.961	0.949	0.812 ± 0.026
164	0.958	0.980	0.980	0.965	0.871	0.773 ± 0.047
239	0.975	0.982	0.983	0.976	0.960	0.882 ± 0.028

Table 5.1: Corrections to the S_{beam} scaler.

Events whose vertices are reconstructed farther than 5 cm from the beam axis are assumed to be misreconstructions. The assumption behind this correction is that the profile of the beam varies linearly from the upstream to the downstream ends of the target and that the level of misreconstruction of target vertices is small in comparison to the correct reconstruction probability in the air. Distortions in the ratio can be seen in the immediate neighborhood of the target endcaps. These distortions can be attributed to the higher probability of misreconstruction of events when particles traverse the thick endcap walls and are multiply scattered.

The systematic uncertainty associated with the beam missing target correction is taken to be half the value of the difference between the ratio measured at upstream and downstream air slices of the target. The beam corrections are generally larger for the 1993 data run than for the 1991 data run and result in a larger error in the overall determination of cross sections.

The various corrections and the total uncertainty in the beam normalization are summarized in Table 5.1.

5.5 Charged Particle Identification

Charged particles are identified as particles which deposited energy in one of the thin ΔE counters. In order to be considered a valid charged particle, the following additional conditions must be met:

- The particle must have registered a hit in at least one wire chamber to improve the resolution of quantities used for particle identification.

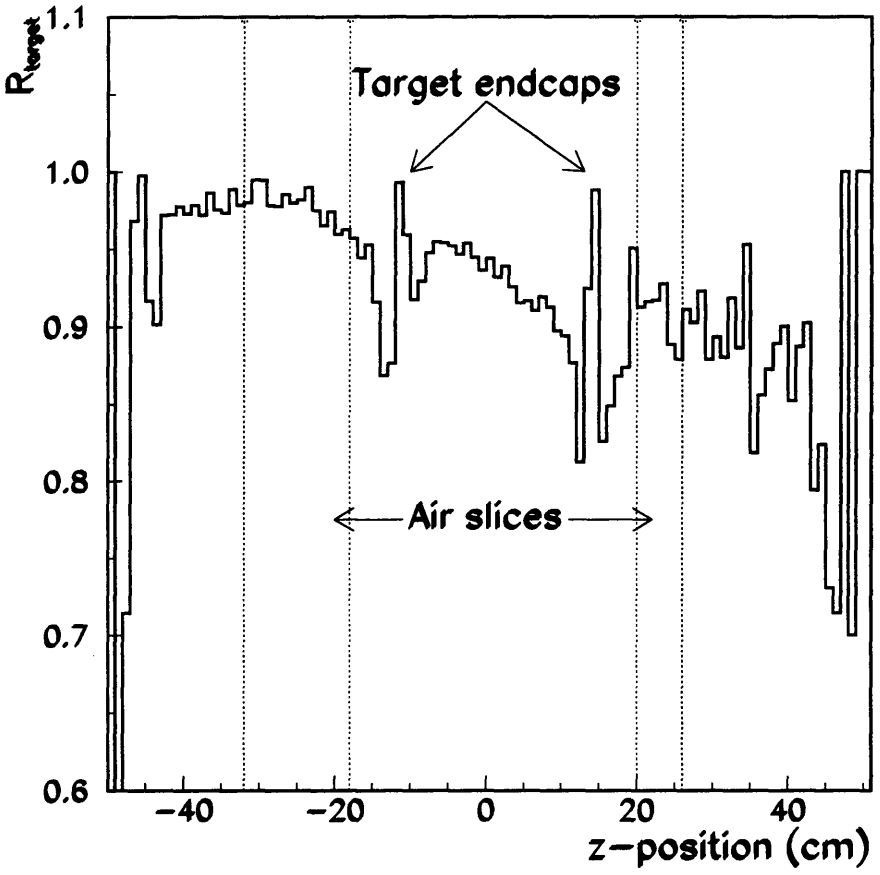

Figure 5-3: This figure shows the regions considered in making the beam missing target correction.

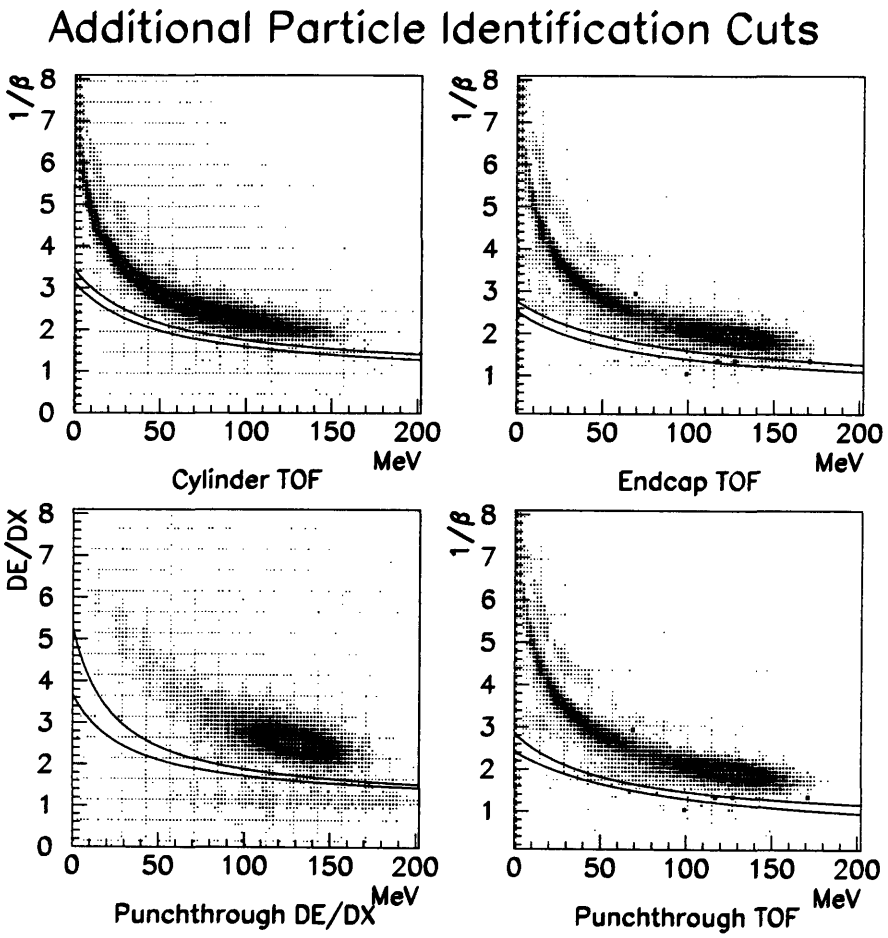

Figure 5-4: Additional particle identification cuts applied to reduce the amount of pion contamination in the sample.

- The particle must have deposited at least 2.5 MeV of light to ensure that noise in the detector is not counted as a valid charged particle.
- The particle must have a reduced time-of-flight of less than 7 ns, which corresponds roughly to a 10 MeV threshold for protons and a 20 MeV threshold for deuterons. This removes the possibility of inclusion of particles from the next beam burst.

Charged particles are passed through the particle identification machinery described in the previous chapter. The conventional charged PID methods are able to remove roughly 95% of the events with charged pions in the final state. Nevertheless, some visible pion contamination remains in the sample.

In order to reduce further the pion contamination, additional PID cuts are added. Additional timing constraints are placed on all charged particles to remove those which are too fast to be protons. Figure 5-4 shows the individual cuts for the three particle classes: pure cylinder, pure endcap, and punchthrough. The additional timing cuts are somewhat looser than the original pion PID cuts. The original and additional timing cuts are shown for comparison. The lower of the two cuts on each graph is the additional timing cut. Punchthrough pion contamination is still clearly visible in the E *vs.* dE/dX endcap plots, so an additional cut is added for this PID method. The result of these additional cuts is that the remaining pion contamination is reduced by more than a factor of two.

5.6 Pion Contamination

To determine the amount of pion contamination which remains, a clean sample of events in which there is a pion in the final state is needed. The quasifree πp cross section on deuterium is used to measure the amount of contamination. Assuming that the neutron is at rest inside the deuteron, one can calculate the energies of two charged particles assuming one knows their angles and identities. Good πp events are chosen by a sharp cut on the energy difference of the sum of the energies of the two particles as calculated by the wire chambers and the incident pion kinetic energies (See Figure 5-5 a)). Cuts are also made requiring that the two particles are back-to-back in ϕ, but not in θ (See Figure 5-6). After these cuts are made, some SCX contamination still remains in the sample. These events are eliminated by cutting on the invariant mass spectrum formed by the two charged particles assuming they are both protons (See Figure 5-5 b)).

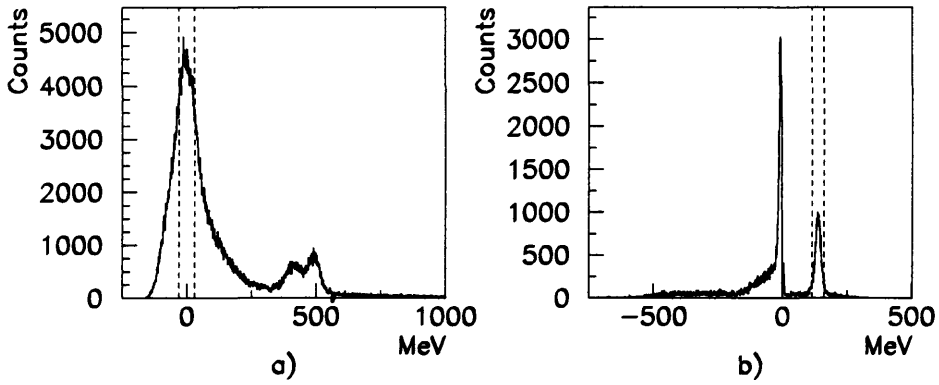

Figure 5-5: a) This figure shows the sharp cut applied to the difference between the sum of the energies of two particles as calculated using only the wire chamber information and the incident pion kinetic energy. It is assumed that particles were a proton and a pion and both permutations are plotted. b) This figure shows the cut applied to the invariant missing mass to exclude SCX contamination from the πp sample.

After one obtains a clean sample of events in which there is a charged pion, these events are passed through the analysis chain. The amount of pion contamination is determined by examining the fraction of events which are misidentified as being part of the absorption cross section. The amount of pion contamination present after all PID methods are used is typically less than 2%. This level of pion contamination is further reduced by the missing mass cuts and missing energy cuts to an insignificant level.

5.7 Estimates of Reaction Losses

The PID cuts also result in a loss of good events due to misidentification of protons, and to a lesser extent deuterons, as pions. This may happen as a result of nuclear reactions in the scintillator causing the particle to fall into the pion band. In order to estimate the reaction losses, a clean sample of events is isolated and then run through the various cuts to determine the number of protons lost in the PID process. The *ppd* absorption channel was chosen for

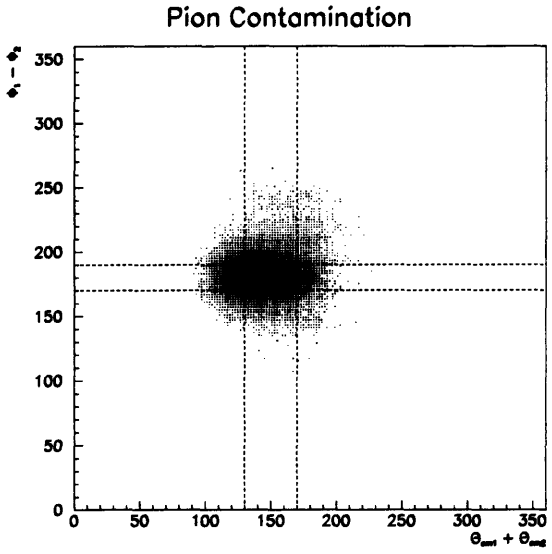

Figure 5-6: This figure shows the cuts which were applied to the θ and ϕ differences between two particles assumed to be protons and calculated in the deuterium center-of-mass system to isolate πp scattering events.

the determination of reaction losses. The use of this reaction channel allows for a simultaneous determination of reaction losses for both protons and deuterons.

The clean sample of events is obtained in the following manner: First, only events containing three charged particles with wire chamber information and coming from the target gas are considered. The three particles are assumed to be 2 protons and a deuteron, and all three particle permutations are attempted. Using the wire chamber information, the energies of the three particles are determined. The two protons are then ordered according to their energies as determined by the wire chambers. Two of the particles, henceforth the control particles, are assumed to have been assigned correctly, and the missing mass of the third or test particle under this assumption is calculated. A sharp cut is applied to the calculated missing mass around the expected value of the test particle. This cut assures that events in which there was a reaction in one of the two control particles are eliminated. All events satisfying the above constraints are then passed through the PID machinery.

The energy of the test particle is determined from the energies of the two control particles. The ratio of the number of events in which the test particle is correctly identified as not being a pion is plotted as a function of the energy of the test particle as determined from the control particles. As can be seen from Figure 5-7) the reaction losses for protons and deuterons are a smoothly varying function of energy. At low energies, almost no protons or deuterons are lost. The maximum loss occurs for highly energetic protons, and is on the order of 15%.

5.8 Losses Due to Wire Chamber Inefficiencies

The failure of one or more particles to register hits in the chambers and the misassociation of hits with particles leads to inefficiencies. To estimate the wire chamber efficiency, a pure sample of absorption events on deuterium or ^{4}He must be isolated without using wire chamber information. This is accomplished by making a cut on the peak of the sum of light deposited by all particles in the detector. The deuterium data is used to assess the wire chamber efficiency for two charged particle absorption events and the ^{4}He data for three charged particle absorption events. The ratio of the number of events in which there is enough information wire chamber information to reconstruct the event to the total number of absorption events in the sample gives an estimate of the wire chamber efficiency. For the two particle events the average efficiency for the four energies is 95% and for three particle events the average efficiency is 98%.

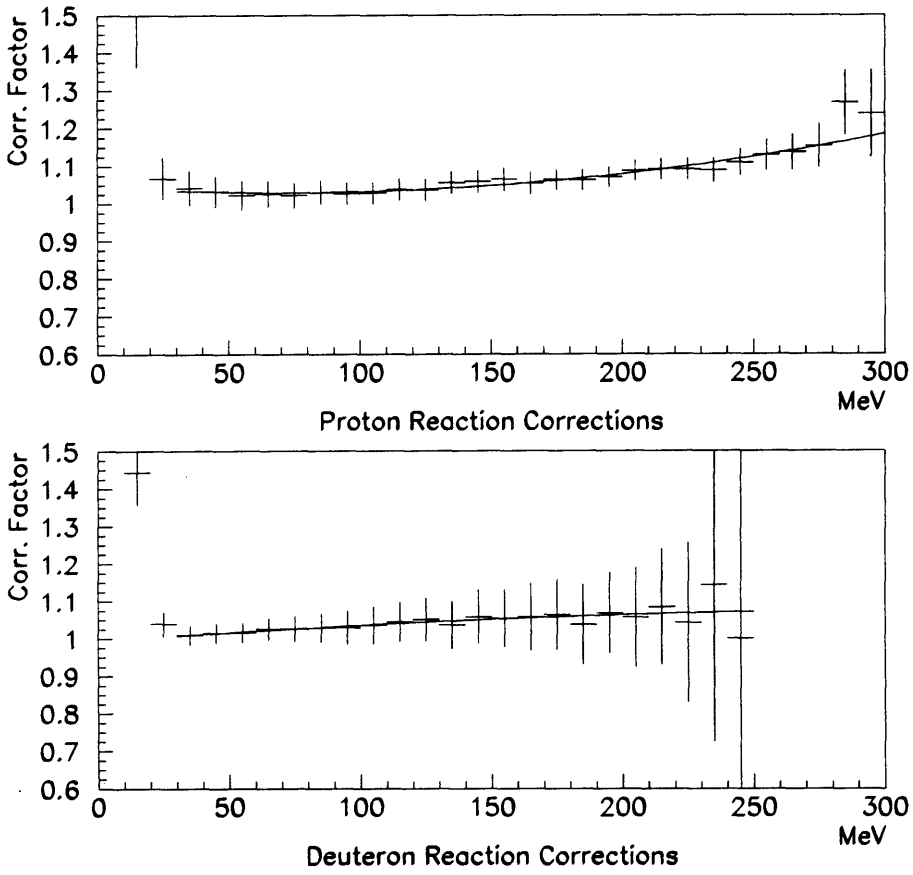

Figure 5-7: The energy dependence of reaction losses for protons and deuterons.

5.9 Neutral Particle Identification

Particles which did not trigger the first ΔE counter which they encountered are identified as neutral particles. In a small number of cases, charged particles did not trigger the ΔE counters, but are identifiable as charged particles because they registered a hit in one of the wire chambers. These particles are re-designated as charged particles, and the time-of-flight information is used to determine whether or not they are pions.

Particle identification is done on genuine neutral particles by using time-of-flight. As can be seen in Figure 5-8 γs are clearly separable from neutrons. The cuts in the γ peaks were made sufficiently tight that contamination from neutrons misidentified as γs was insignificant.

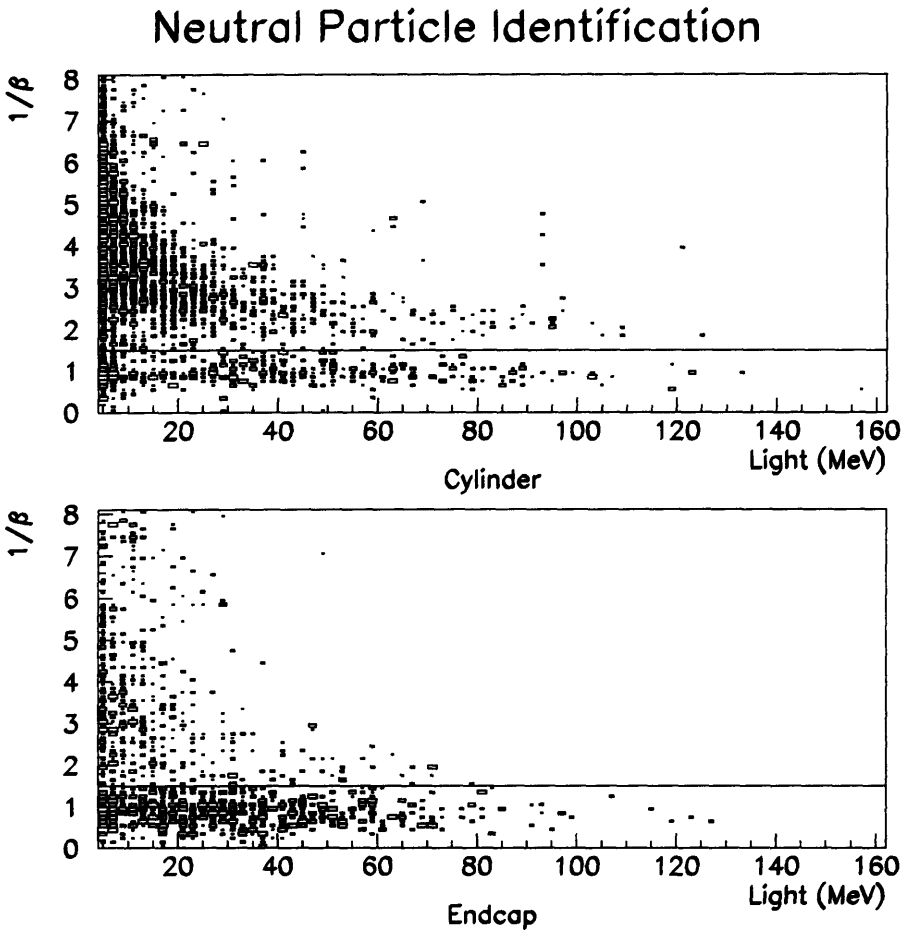

Figure 5-8: Particle identification cuts applied to neutral particles.

Chapter 6

Decomposition into Physical Channels

6.1 Introduction

This chapter discusses the methods used in the decomposition of the total absorption cross section into competing channels. The first sections are devoted to the performance of the Monte Carlo simulation, as the reliability of the simulation is critical to the correct determination of both the decomposition and the total absorption cross section.

In the previous chapter, estimates were made of the wire chamber efficiencies and the losses due to reactions in the scintillator. In this chapter, these estimates are compared to the reaction losses and wire chamber inefficiencies as determined by the Monte Carlo simulation. The reliability of the determination of losses depends on how well the energy loss, multiple scattering, and nuclear reactions are handled by GEANT and on how well the scintillator response and wire chambers are modelled in the simulation. Most of the channels analyzed are kinematically complete so that pion contamination and SCX can be virtually eliminated by the judicious use of missing energy and invariant missing mass cuts.

6.2 Monte Carlo Performance

The general technique employed in the determination of how well the Monte Carlo simulation reproduces the data involves the isolation of a particular set of absorption events from both the

data and Monte Carlo event sample under the same conditions. Once isolated, identical cuts are performed on the data and Monte Carlo samples and the results are compared.

There are two important considerations involved in the replication of the data by the Monte Carlo simulations. The first concerns the integrated response of the detector, which is important in order for the Monte Carlo to reproduce overall normalizations. If the Monte Carlo perfectly simulated the response of the detector, the fractional losses of absorption events due to wire chamber inefficiencies and particle misindentification would be identical to that observed in the data. Unfortunately, the Monte Carlo is not perfect, and hence uncertainties associated with this imperfection arise. The second consideration, which is particularly important for the decomposition into competing channels, is how well the differential response of the detector is handled.

6.2.1 Reaction Corrections

There are two different ways an absorption event may be lost due to a nuclear reaction. The first is if one of the particles falls out of the PID band and is designated a pion. Figure 6-1 shows a comparison of the proton bands from the data and the Monte Carlo simulation. The events were isolated from the deuterium data using only wire chamber information by making a sharp cut on the angular correlation of the two particles. The overall shapes of both the dE/dX and TOF proton bands are well reproduced by the Monte Carlo simulation. The adequacy of the Monte Carlo in reproducing losses due to PID can be assessed in a more quantitative manner by an analysis similar to that performed in the last chapter in estimating the reaction losses. In the last chapter, *ppd* absorption events from ^{4}He were used to calculate the fraction of protons and deuterons which were misidentified as pions as a function of energy. In this case, the probability of misidentifying a proton or a deuteron as any other particle is determined. Figure 6-2 shows a comparison of the misidentification fraction for protons and deuterons as calculated using real data and Monte Carlo produced data. The proton misidentification probabilities are reproduced extremely well by the Monte Carlo. The simulation, however, is less successful in reproducing the deuteron misidentification probabilities. Part of the difference between the data and the Monte Carlo curves for the deuteron losses can be attributed to contamination in the data from the *ppp* channel, which tends to fill in the mid-range area between roughly 50 and 120 MeV. Attempts have been made to reduce the contamination from the *ppp* final state and have shown that the true data curve should lie somewhere in between the data curve plotted and the MC prediction. Nevertheless, even after making such a correction, the simulation still underpredicts the misidentification probability for deuterons. The inability of the simulation

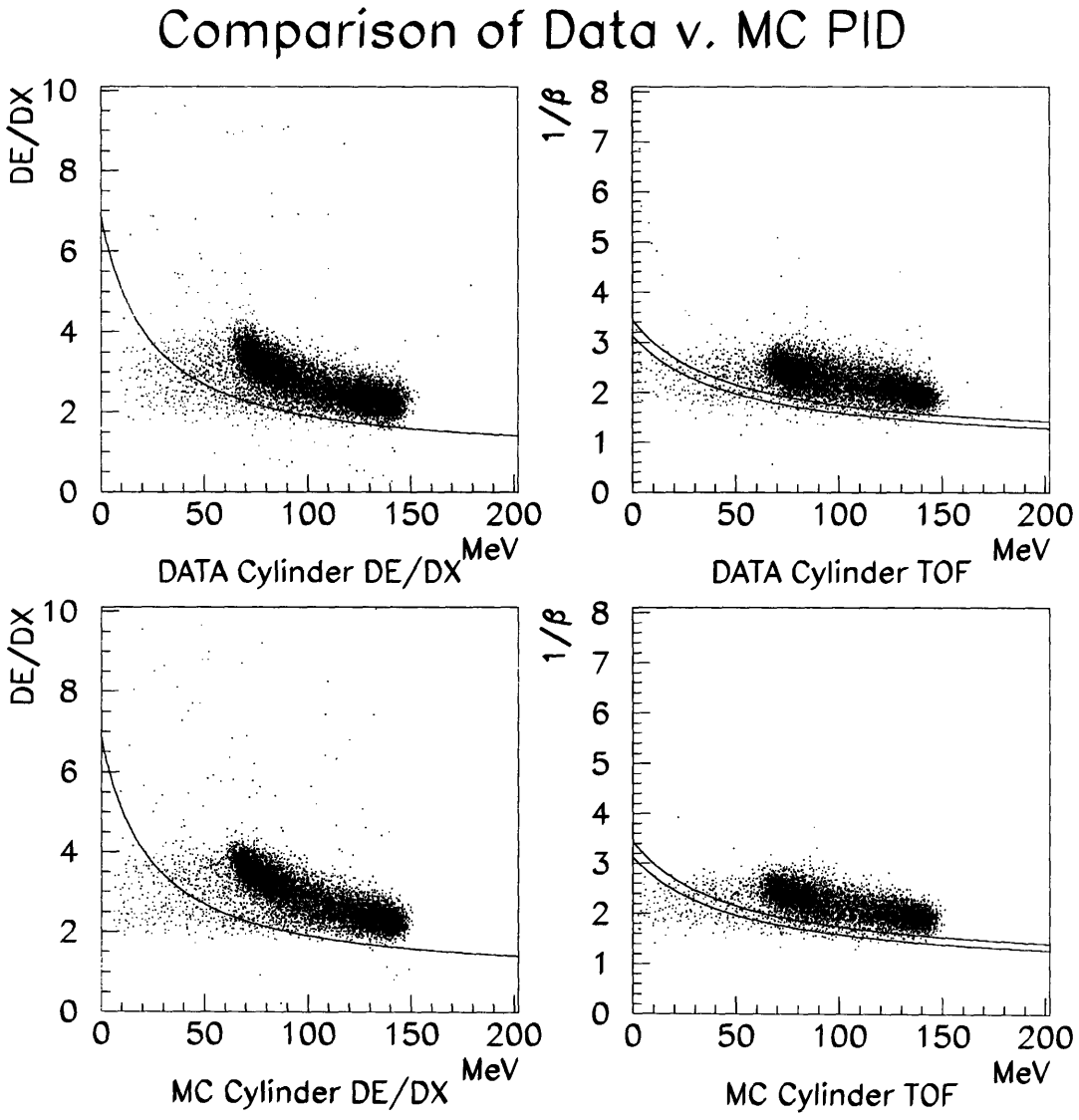

Figure 6-1: A comparison of the cylinder particle identification plots of the data and Monte Carlo.

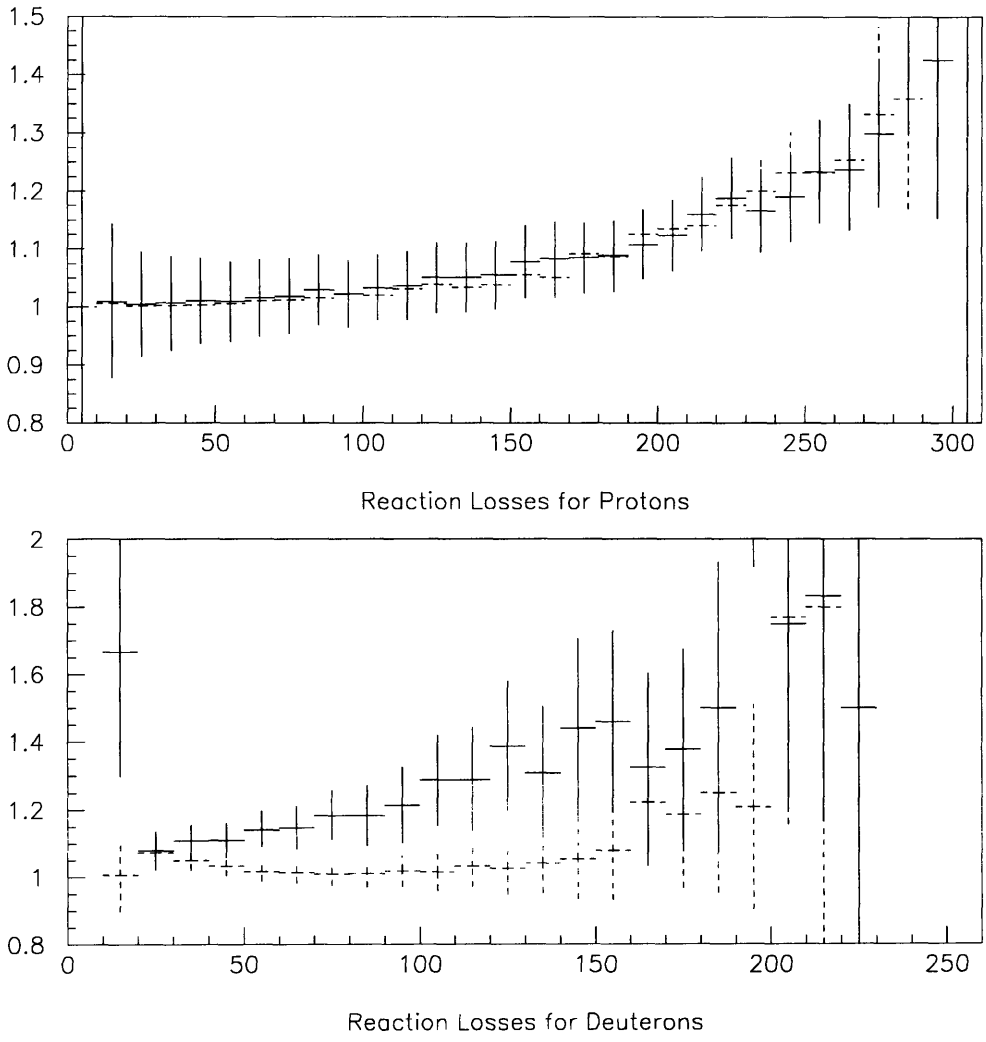

Figure 6-2: A comparison of the corrections for misidentified protons and deuterons as determined from the data (solid markers) and Monte Carlo simulation (dashed markers).

to reproduce the deuteron misidentification probability may be attributable to the fact that deuteron reaction cross sections are much less well known than proton reaction cross sections.

The probability that a deuteron will be misidentified as a pion is much lower than the probability that a proton will be misidentified as a pion. Hence, the dominant factor involved in the normalization uncertainty comes from protons misidentified as pions. From comparison of the integrated misidentified proton curves from the data and the Monte Carlo simulation, the normalization uncertainty due to PID is determined to be $\pm$ 4%.

After particle identification has been done, additional events may be lost due to reactions by cuts on energy dependent quantities such as the total energy deposited in the detector, the missing momentum, and the missing mass. Figure 6-3 shows a comparison of the data with the Monte Carlo for the summed energy of the two protons detected following absorption. The nuclear reaction tail produced by the simulation appears to be a fairly accurate representation of the nuclear reaction losses in the LADS detector. The bottom figure shows the subtraction of the data histogram from the Monte Carlo. Small mismatches in energy calibration and width cause the deviations apparent near the peak value. The data also exhibit a small dip immediately below the peak value which is not reproduced by the Monte Carlo. Figure 6-4 shows a comparison of the missing mass and missing energy calculated from two protons following absorption on deuterium. The agreement between Monte Carlo and data is again quite good. By making somewhat loose cuts on these energy dependent quantities, normalization uncertainties resulting from differences between data and Monte Carlo can be kept below the 2% level.

6.2.2 Wire Chamber Efficiencies

The wire chamber efficiency for a given event depends on the number of particles in the final state and their relative positions in the detector in a complicated manner. As the number of charged particles in the final state increases, the chances that multiple particles register in the same cathode strips on a given chamber increases. If two particles register hits in the same cathode clusters, the cathode cluster is only assigned to one of the two possibilities. The anodes and cathodes of the wire chambers in the LADS detector are modelled in the Monte Carlo simulation so that inefficiencies arising from such effects as multiple particles hitting the same cathode strips are taken into account. The resolutions of the chambers in reconstructing ϕ and z are reproduced well by the Monte Carlo simulation. Figure 6-5 shows comparisons between the data and the Monte Carlo of the difference in ϕ and the sum of θ between two

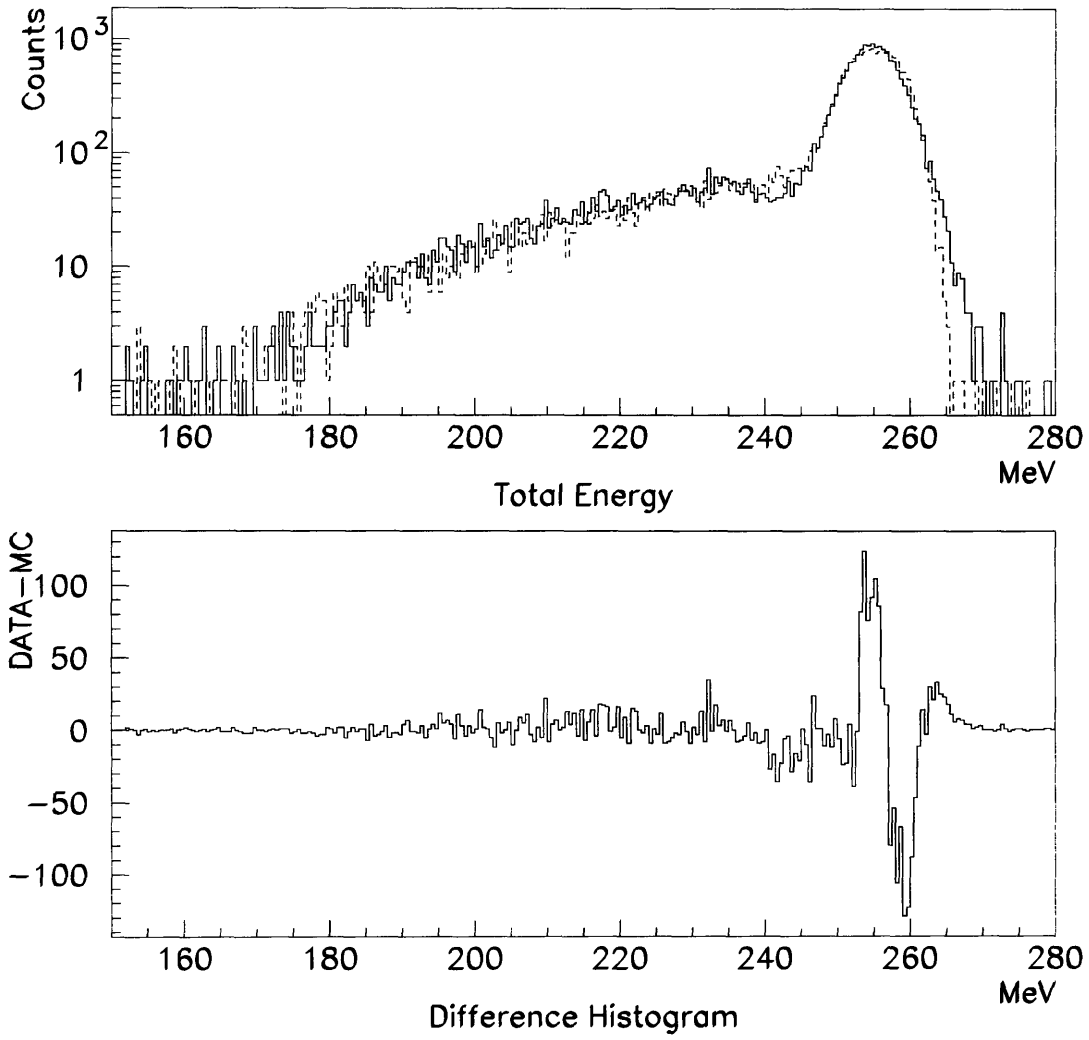

Figure 6-3: The top figure shows a comparison of the the total energy deposited in the detector by two protons following absorption on deuterium. The solid line is the data and the dashed line is the Monte Carlo simulation. The bottom plot shows a subtraction of the Monte Carlo distribution from the data distribution.

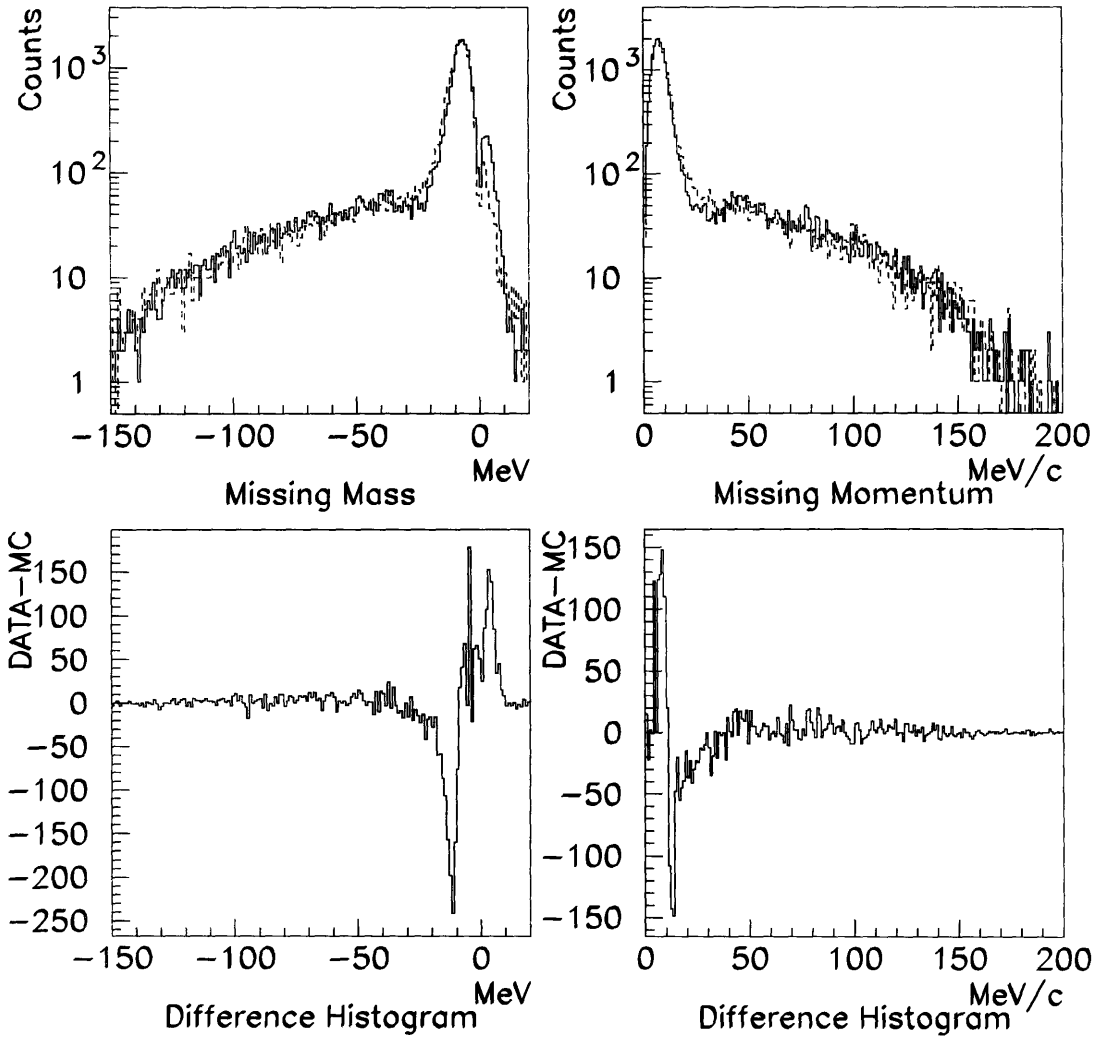

Figure 6-4: The top figures show comparisons of the missing mass and missing momentum distributions of two protons following absorption on deuterium. The solid lines are the data and the dashed lines are the Monte Carlo simulations. The bottom plots show the subtraction of the Monte Carlo distributions from the data distributions.

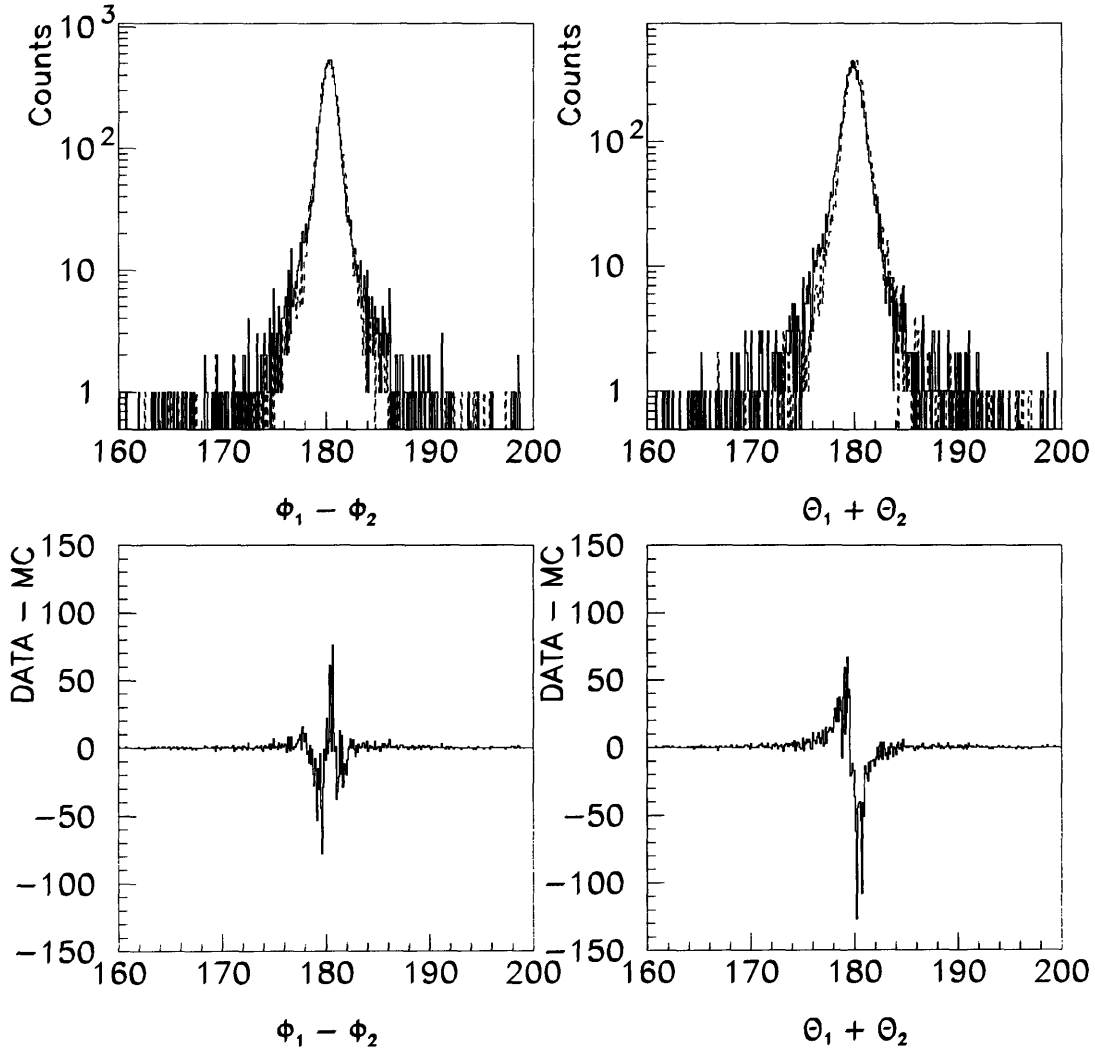

Figure 6-5: A comparison of the distributions of the differences in ϕ and the sum of θ of the two protons following absorption on deuterium in the data and in the Monte Carlo. The solid lines are the data and the dashed lines are the Monte Carlo simulations. The bottom plots show the subtraction of the Monte Carlo distributions from the data distributions.

protons in the CM following absorption on deuterium. The subtraction of the two histograms is also shown.

To assess the normalization uncertainty associated with the modelling of the MWPC reconstruction in the Monte Carlo simulation, absorption events are isolated on deuterium and ^{4}He by making a cut on the sum of light deposited by charged particles in the detector. The same procedure which is applied to the data is applied to the Monte Carlo simulation. The deuterium comparison is used to assess the normalization uncertainty for two charged particle absorption events and the ^{4}He comparison for three charged particle absorption events. In the ^{4}He case, two generators are used to test the reconstruction efficiency: a three-body *ppd* phase space generator and a *ppp* phase space with a spectator neutron generator.

The comparison of the data with Monte Carlo is performed at the four incident pion energies. In all cases, the difference between the data and Monte Carlo determinations of the fraction of absorption events in which there is enough wire chamber information to reconstruct the event is less than 3%. To be somewhat conservative, the normalization uncertainty associated with the simulation of MWPC reconstruction is taken to be 4%.

The adequacy of the simulation for reproducing the differential wire chamber efficiency can be demonstrated by comparing the θ distributions of protons following absorption on deuterium as seen by the detector and as modelled by the simulation (see Figure 6-6).

6.2.3 Neutron Detection Efficiencies

The modeling of neutron efficiencies by the simulation is important for the measurement of absorption final states in which a neutron is detected. Neutron reactions in the Monte Carlo simulation are handled by GEANT. For neutrons under 20 MeV MICAP is used to calculate reaction probabilities, while above this energy the FLUKA section of the code is used. To compare the neutron detection efficiencies in the data and in the simulation, absorption events from ^{4}He in which there are three protons detected are used. From the energy and angular information of the three protons, the expected energy and direction of the neutron is calculated. In the data, events in which there are three protons and a two track vertex from within the target volume are isolated. A tight cut on the missing mass corresponding to the mass of a neutron is applied to ensure that the events under consideration are indeed absorption events in which three protons are detected. Events in which the reconstructed neutron direction is within 30° of a proton are excluded from the sample to avoid final states in which there could have been a soft

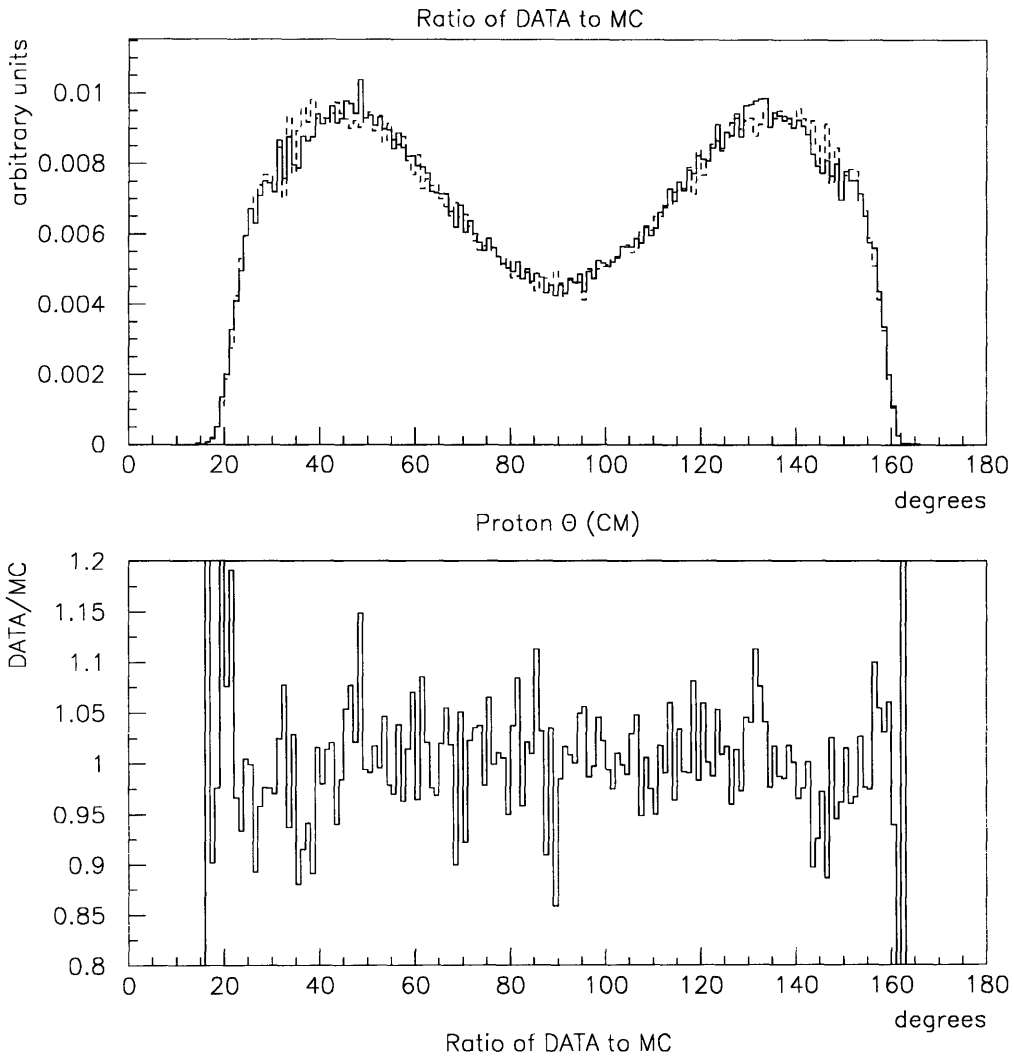

Figure 6-6: A comparison of the CM θ distributions of the two protons following absorption on deuterium. In the top figure, the solid line is the data and the dashed line is the Monte Carlo. The bottom figure shows the data distribution divided by the Monte Carlo distribution.

final state interaction. The number of times a neutron is detected within $\pm$ 15° in ϕ and θ of its expected position is compared to the total number of events in the sample. The ratio of expected neutrons to those detected is the neutron detection efficiency. The same procedure is applied to Monte Carlo simulation, with a sample of events thrown using a pure *pppn* phase space generator and a *ppp* phase space with a spectator *n* generator. Figure 6-7 shows a comparison of the energy and polar angle dependence of the neutron detection efficiencies as measured in the data and the Monte Carlo simulation. The normalization uncertainty associated with using the Monte Carlo simulation for neutron detection can be estimated by integration over the differential efficiency distributions. The normalization uncertainty for neutron detection is taken to be 3%.

6.3 Determination of Absorption Cross Section on Deuterium

The absorption cross section on deuterium can be used to verify that the correction factors and overall normalization can be determined correctly using the Monte Carlo simulation. Absorption events on deuterium were selected by demanding that they have at least a one track vertex, two protons and no pions in the final state. Furthermore, the sum of the energy deposited in the detector is required to be at least 30 MeV above the incident pion kinetic energy, and the protons are required to be within $\pm$10° of back-to-back in θ and ϕ in the center-of-mass system. Empty target subtraction was performed, and the Monte Carlo simulation was used to correct for the missing acceptances. The cross sections which were obtained are shown in Figure 6-8, along with the Ritchie parameterization of the world's data [89].

6.4 Separation of Absorption Yield Into Competing Channels

Pion absorption events are characterized by the fact that there is no pion in the final state. Following the absorption of a pion, there are three distinct final state possibilities, *pppn*, *ppd*, and ^{3}He-*p*. Because of the large threshold for the detection of ^{3}He nuclei with the LADS detector, contributions from this channel are ignored. The contribution from the ^{3}He-*p* final state has been deduced in previous experiments from the measurement of the charge conjugate channel and has been found to be small[56]. Events from the two final states *pppn* and *ppd* can be classified by the numbers and types of charged particles observed in the LADS detector.

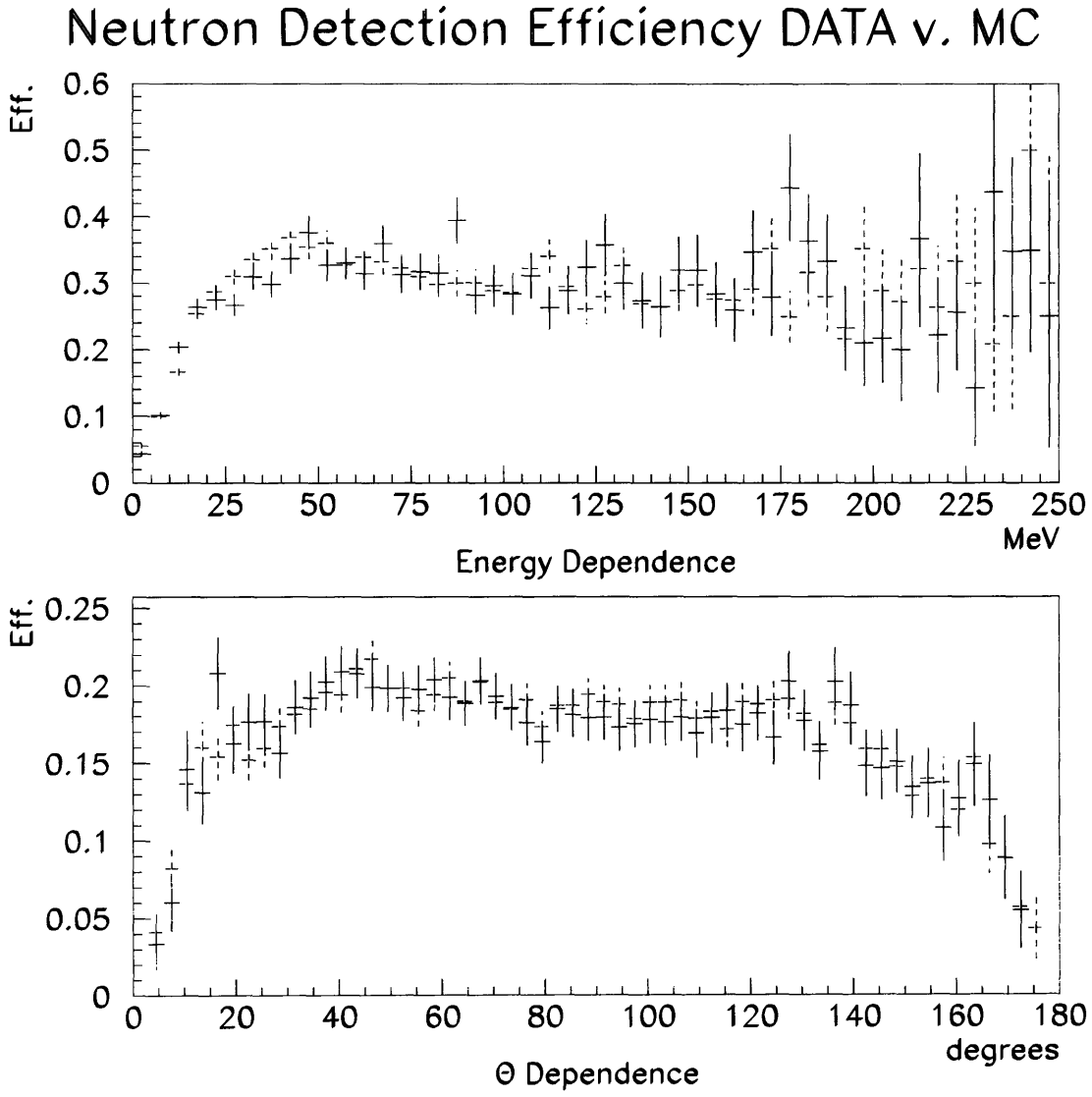

Figure 6-7: A comparison of the neutron detection efficiency as a function of energy and angle as detected by LADS and as modelled in the Monte Carlo simulation. The solid points are the data and the dashed points are the Monte Carlo simulation.

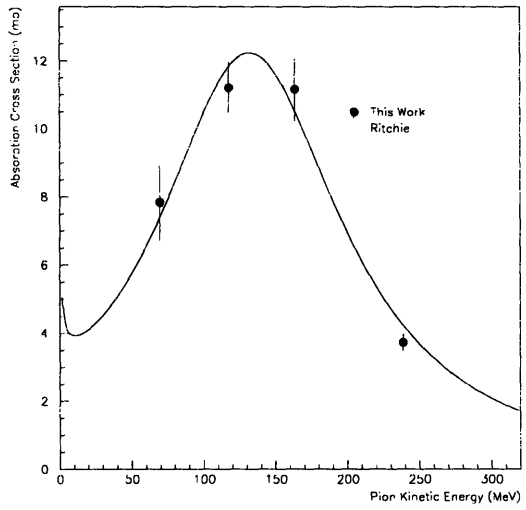

Figure 6-8: The total absorption cross sections on deuterium as measured by this experiment compared to the fit to Ritchie's fit to the world's data [89].

These classification types will be henceforth called charged detector channels. Charged detector channels are classified by the number and type of charged particles in the final state. In all cases except the *pp* case, a cut is made on the missing invariant mass for the charged detector channel to eliminate events in which a particle is misidentified, or in which a substantial amount of reaction loss occurs. In the *pp* case, the missing particles may either be a deuteron or an unbound *pn* pair so a missing invariant mass cut cannot be applied. The charged detector channels important for absorption are *pp*, *ppp*, *pd*, and *ppd*. The total absorption cross section as well as the breakup into physics channels is accomplished by extrapolation of the raw cross sections measured in the charged detector channels over unmeasured regions of phase space.

The physics channels considered in the breakup can be classified by the number of particles which participated in the reaction and the number which were spectators. The characteristic shape of a spectator momentum distribution is a logarithmic fall off with increasing momentum.

The physics channels which are considered in performing the breakup are:

- $(pp)d$ or pn- In this case there are two energetic protons and either a spectator deuteron or an unbound pair of nucleons, p and n, following the absorption. These physics channels

contribute primarily to the *pp* charged detector channel, as the spectator particles usually fall below detector threshold.

- $(ppp)n$- In this physics channel the three protons in the final state are involved in the absorption, while the neutron behaves as a spectator. Events of this type are mainly detected in the *ppp* charged detector channel.

- $(ppn)p$- In this physics channel two protons and a neutron are involved in the absorption, while the other proton behaves as a spectator. Events of this type contribute primarily to the *pp* charged detector channel.

- $(pppn)$- In this physics channel all three protons and the neutron participate substantially in the absorption, and there are no spectators. Events of this type contribute primarily to the *ppp* charged detector channel.

- $(pd)p$ - This final state contains an energetic proton and an energetic deuteron, with the other proton behaving as a spectator. This physical process contributes primarily to the *pd* charged detector channel.

- (ppd)- In this final state, all three particles share substantially the energy and momentum of the absorbed pion. This physical process contributes primarily to the *ppd* charged detector channel.

In order to perform extrapolations over unmeasured phase space regions, the physics channels are approximated in the simplest manner possible which is consistent with the observed distributions. The $(pp)d$ and $(pp)pn$ channels are modelled as QDA with either a spectator deuteron or spectator *pn* pair. The $(pd)p$ channel was modelled as QDA on two protons followed by a pickup, with a spectator proton. The specifics of how this mechanism is modelled will be described in a later section.

The remaining physics channels; $(ppp)n$, $(ppn)p$, $(pppn)$, and (ppd) are represented as simple phase space distributions. The underlying mechanisms behind these multi-body physics channels may be QDA involving additional collisions before or after the absorption, or they could be genuine new absorption processes. Speculation as to the mechanisms behind these multi-body channels will be deferred until the next chapter. Some deviations are seen between the simple phase space distributions and the observed angular distributions. Because of the large solid angle covered by the LADS detector extrapolations over unmeasured regions are small (typically on the order of 3% for three charged particle final states, and 8% for two

charged particle final states.) Therefore, extrapolations over unmeasured angular regions based on phase space assumptions should be relatively insensitive to these differences.

The energy threshold of the LADS detector for the detection of charged particles is largely responsible for the separation of the absorption cross section into the charged detector channels. There is a rough correspondence between the charged detector channels and the physics channels of interest, as spectator particles tend to be below threshold. Hence, the *pp* charged detector channel is dominated by contributions from undisturbed QDA processes, with lesser contributions from other competing channels. The separation into charged detector channels serves to divide phase space into regions in which only a few of the competing physics channels mentioned above contribute greatly. To further enhance this subdivision of phase space and thus further facilitate the decomposition into physics channels, information about neutrons may be used. In the case of the *ppp* charged detector channel, events can be separated by the magnitude of the reconstructed neutron momenta. The (*pppn*) physics channel tends to populate regions of phase space with higher neutron momentum than the (*ppp*)*n* physics channel. Events from the *pp* charged detector channel in which there is a detected neutron are considered to aid in the separation between (*ppn*)*p* and (*pppn*) final states.

Subsets of the charged detector channels which include additional cuts on the data sample to enhance contributions from particular physics channels over others are used for the determination of extrapolations and the breakup. These subsets will henceforth be referred to as observed channels. The observed channels which are considered and the acceptances for the various physics channels as determined from Monte Carlo simulation are shown in Table 6.1. A description of each of the observed channels follows in the next sections of this chapter.

6.5 Observed *pp* channel

The observed *pp* channel consists of events in which there are no pions and only two protons detected in LADS. The major physics channels which contribute to this observed channel are those in which an undisturbed QDA occurred. To enhance the contribution of the QDA mechanisms over the other physics channels, several additional cuts are made. A cut of 250 MeV/c is made on the missing momentum reconstructed from the two protons. Additionally, the sum of the energy of the two protons is required to be roughly 50 MeV greater than the incident pion kinetic energy, and a loose cut on their angular correlation is applied ($\pm$ 40° in θ and ϕ in the CM system of a deuteron at rest in the ^{4}He nucleus and the incident pion.) The only non-QDA

Physics Channel	Energy	Obs.*pp*	Obs.*ppp*	Obs.*pppn*	Obs.*pd*	Obs.*ppd*	Obs.*ppn*
(pp)d	70 MeV	65%	-	-	-	1%	-
	118 MeV	63%	-	-	-	1%	-
	164 MeV	63%	-	-	-	1%	1%
	239 MeV	48%	-	-	-	1%	1%
(pp)pn	70 MeV	46%	4%	-	-	-	2%
	118 MeV	44%	3%	-	-	-	3%
	164 MeV	44%	5%	-	-	-	4%
	239 MeV	27%	6%	-	-	-	5%
(ppp)n	70 MeV	18%	32%	-	-	-	1%
	118 MeV	12%	37%	2%	-	-	2%
	164 MeV	10%	46%	3%	-	-	2%
	239 MeV	6%	42%	4%	-	-	2%
(pppn)	70 MeV	6%	11%	7%	-	-	8%
	118 MeV	3%	11%	13%	-	-	7%
	164 MeV	2%	11%	24%	-	-	7%
	239 MeV	1%	8%	28%	-	-	4%
(pd)p	70 MeV	4%	-	-	54%	7%	-
	118 MeV	1%	-	-	46%	12%	-
	164 MeV	4%	1%	-	35%	16%	-
	239 MeV	1%	-	-	16%	18%	-
(ppd)	70 MeV	9%	1%	-	11%	40%	-
	118 MeV	7%	-	-	8%	47%	-
	164 MeV	6%	4%	-	6%	47%	-
	239 MeV	4%	1%	1%	3%	48%	-
(ppn)p	70 MeV	10%	1%	1%	-	-	13%
	118 MeV	5%	1%	1%	-	-	12%
	164 MeV	5%	1%	3%	-	-	17%
	239 MeV	3%	1%	4%	-	-	15%

Table 6.1: Acceptances of Monte Carlo simulations representing physics channels to observed channels in the LADS detector.

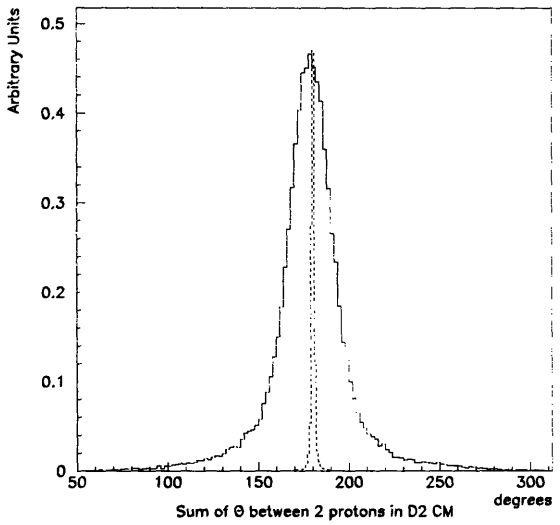

Figure 6-9: A comparison of the width of the angular correlation between two protons following absorption on the deuteron with that resulting from undisturbed QDA on ^{4}He.

physics channel which has a relatively large acceptance, particularly at the lower incident pion kinetic energies is the $(ppp)n$ channel.

Of all of the possible absorption channels, undisturbed QDA is known to contribute the largest fraction to the total. Its features are remarkably similar to absorption on the deuteron. The two energetic protons in the final state after quasifree absorption are roughly back-to-back in the center-of-mass system of a deuteron which is at rest inside the ^{4}He nucleus. The back-to-back peak is much broader in the case of absorption on ^{4}He compared to the deuteron because of the initial momentum of the absorbing pair (see Figure 6-9). The slight shift in the centroid is probably attributable to binding energy effects.

There are two contributing physics channels which can be classified as undisturbed QDA, the process in which the spectator is a deuteron, $(pp)d$, and the process in which the spectators are an unbound pn-pair. To separate the contributions from these competing processes, one must consider the reconstructed invariant mass of the unobserved system. If the spectator was a bound deuteron, and neither of the two detected protons have lost energy due to a nuclear reaction in the scintillator, the reconstructed invariant mass should be the deuteron mass. For the case of an unbound pn-pair, whose missing momentum is less than 250 MeV/c,

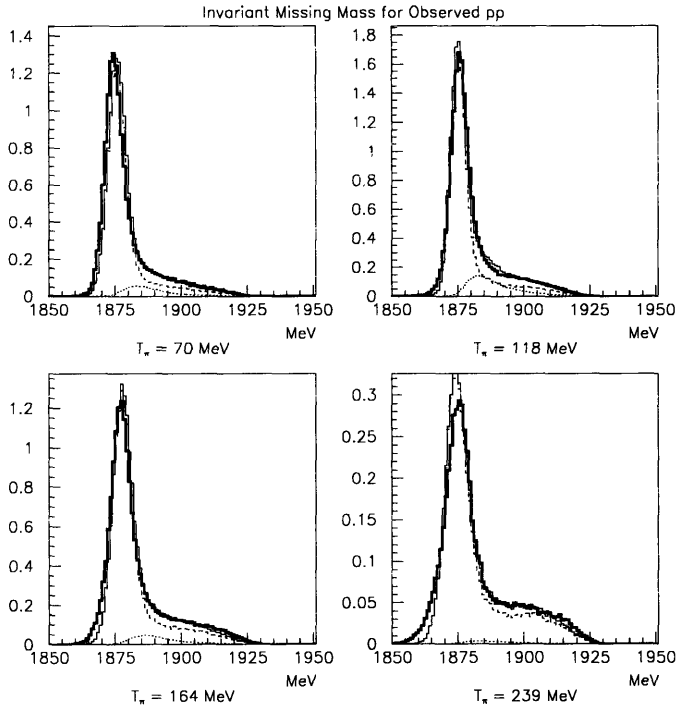

Figure 6-10: The invariant missing mass reconstructed from two observed protons. The dark solid line is the data, the lighter solid line is the simultaneous fit of Monte Carlo simulations. The dashed line is the assigned contribution from QDA with a spectator deuteron and the dotted line is the assigned contribution from QDA with a spectator proton and neutron.

the reconstructed invariant mass will also be peaked, but at a slightly higher value than the deuteron mass. It is difficult to make a separation of the two contributions. Nevertheless, it appears that a large part of the QDA strength can be explained by the model in which the spectator is a bound deuteron (see Figure 6-10). This suggests that when QDA occurs the spectators are preferentially left in a bound state instead of as a free *pn* pair.

The angular distributions of the protons are surprisingly well fit by the QDA Monte Carlo simulations. Figure 6-11 shows the comparison of the data with the distributions obtained from Monte Carlo simulation. At the highest energy, the dip at forward angles, which can also be seen in the Monte Carlo distributions, is due to an inefficiency in the wire chamber reconstruction code which results from specific geometries in which two outgoing particles hit the same set of cathode strips on the outer wire chamber.

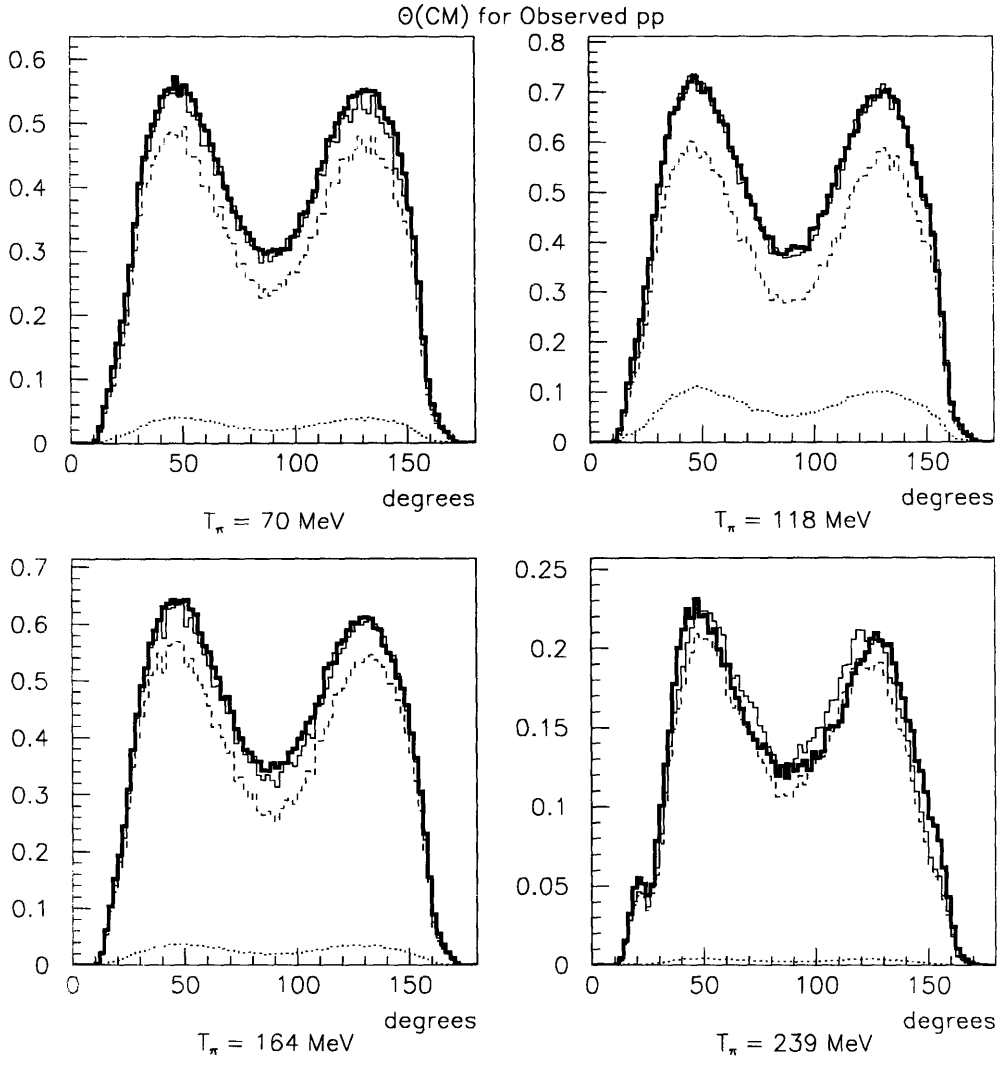

Figure 6-11: The polar angle θ of the two observed protons in the CM system of the incoming pion and a deuteron at rest in the ^{4}He nucleus. The dark solid line is the data, the lighter solid line is the simultaneous fit of Monte Carlo simulations. The dashed line is the assigned contribution from QDA with a spectator deuteron and the dotted line is the assigned contribution from QDA with a spectator proton and neutron.

6.6 Observed *pd* and *ppd* channels

There are two charged detector channels which contain a deuteron in the final state, the *pd* and *ppd* channels. The observed *pd* channel consists of the *pd* charged detector channel with two additional constraints. The first is that the summed energy deposited in the detector by the proton and the deuteron be roughly 35 MeV above the incident pion kinetic energy. The second is that the missing momentum of the undetected proton be less than 200 MeV/c. The missing momentum cut was chosen 50 MeV/c lower than is taken on the observed *pp* channel to define a spectator to eliminate contamination in the data sample which is attributable to $\pi - d$ scattering in which the deuteron was detected and the pion converted in the scintillator. The major physics channel which contributes strength to the observed *pd* channel is $(pd)p$, with contaminations from (ppd) and $(pp)d$. Contributions from the $(pp)d$ channel are suppressed for this observed channel because of the expected logarithmic fall-off of the spectator momentum of the deuteron and the requirement that one and only one proton be detected. The constraint that only one proton be detected, along with the requirement that the momentum of the undetected proton be less than 200 MeV/c suppresses the contribution from (ppd).

Figures 6-12 and 6-13 show the energy and angular spectra of the observed *pd* channel. The proton and deuteron appear to be emitted roughly back-to-back in the CM frame of a deuteron at rest in the ^{4}He nucleus and the incoming pion. The deuteron also appears to be emitted preferentially at backward angles.

In order to calculate an acceptance correction for missing solid angle, the angular distributions should be fairly well approximated. Hence, the simulation which models the physics channel $(pd)p$ should have the preferential backward deuteron emission built into it.

The $(pd)p$ simulator is constructed as follows. First, three-body phase space is thrown and weighted by a single particle proton momentum to simulate the spectator. The CM system in which one of the protons and the deuteron momenta are back-to-back is reconstructed, and the pion momentum in this frame is determined. The event is then weighted by the Ritchie parameterization for absorption on a *pn* pair. The resulting generator produces distributions which are symmetric in the CM system of the proton and the deuteron.

The forward backward asymmetry of the final state is included in the simulation by dividing the observed *pd* proton θ distribution by the distribution obtained from the simulator, and then fitting the divided spectrum by a Legendre polynomial. The value of the Legendre polynomial

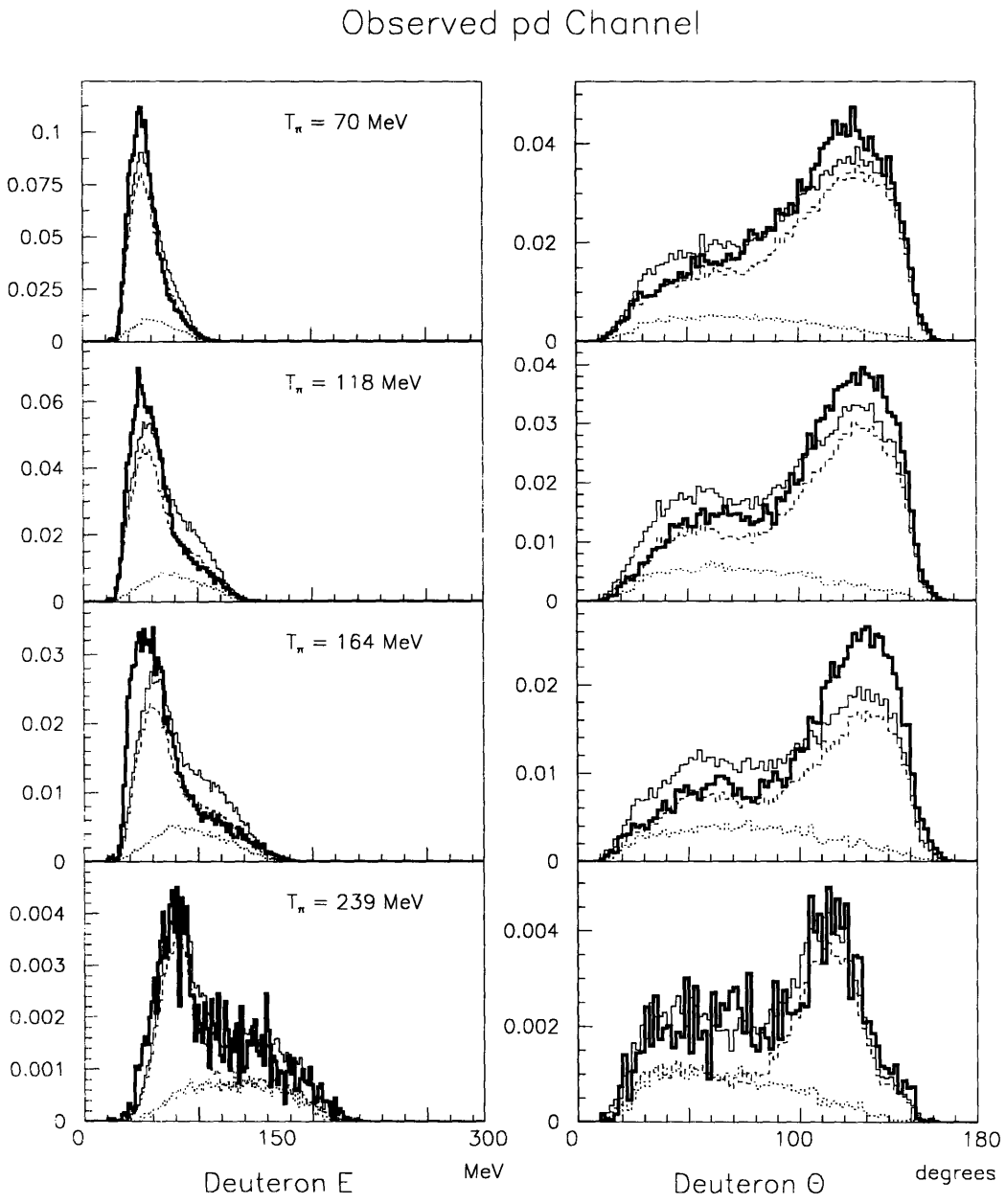

Figure 6-12: The LAB energy and θ distributions of the deuteron for the observed *pd* channel. The dark solid line is the data, the lighter solid line is the simultaneous fit of Monte Carlo simulations. The dashed line is the assigned contribution from the $(pd)p$ channel and the dotted line is the assigned contribution from the (ppd) channel.

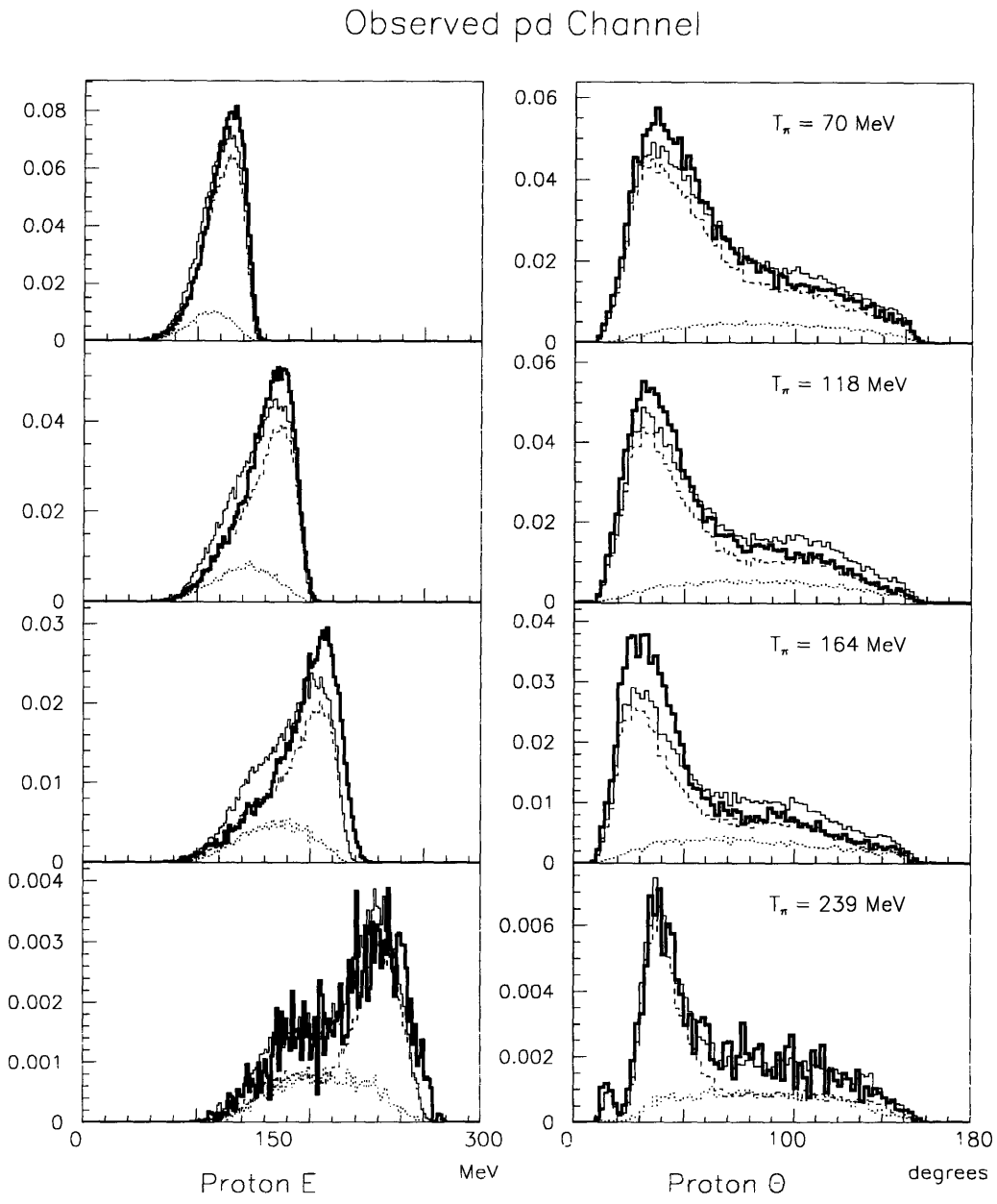

Figure 6-13: The LAB energy and θ distribution of the proton in the observed *pd* channel. The dark solid line is the data, the lighter solid line is the simultaneous fit of Monte Carlo simulations. The dashed line is the assigned contribution from the (*pd*)*p* channel and the dotted line is the assigned contribution from the (*ppd*) channel.

is used to modify the weights of events produced by the generator. The resulting simulator is then taken as the representation of the $(pd)p$ physics channel.

The major source of contamination in the observed pd channel is the (ppd) channel. Since the acceptance for this process is roughly a factor of four smaller than the acceptance for the $(pd)p$ physics channel, the effect of changes in the measured angular distribution of protons due to the (ppd) channel was ignored.

The distributions of the observed pd channel appear to be consistent with absorption on a quasi-deuteron pair, followed by the pickup of a neutron by one of the outgoing protons. The preference for the emission of the deuteron at backward angles can be explained in terms of the difference in momentum mismatch between a neutron with fermi momentum inside a nucleus and either a forward or a backward going proton following absorption.

The observed ppd channel is a subset of the charged detector ppd channel. An additional cut demanding that the sum of the energies of the deuteron and the two protons be roughly 50 MeV above the kinetic energy of the incident pion is applied. There are three physics channels which can have possible contributions to the observed ppd channel: (ppd), $(pd)p$, and $(pp)d$. The $(pd)p$ and $(pp)d$ physics channels are suppressed by the requirement that in order to be included in this observed channel, the spectator had to have been above detector threshold. The agreement of the fit with the angular distributions seems to be fair, but there are large discrepancies in the energy distributions, particularly in the deuteron energy spectra (see Figures 6-14 and 6-15.) The deuteron energies in the data show a peaking at lower energies than the model distributions. In the next chapter possible explanations of this behavior will be explored.

6.7 Observed *ppp* and *pppn* channels

For the ppd charged detector channel, there are four physics channels which have relatively large acceptances: $(pp)pn$, $(ppp)n$, $(ppn)p$, and $(pppn)$. The contributions from the $(pp)pn$ and $(ppn)p$ channels can be reduced by placing an energy threshold on the three detected protons. The contributions from the $(ppp)n$ and $(pppn)$ channels may be enhanced with respect to one another by placing a cut on the reconstructed momentum of the neutron. In the observed ppp channel, three protons must be detected above an energy threshold of 30 MeV, the invariant missing mass must be equal to the mass of a neutron, and the reconstructed momentum of the neutron must be less than 250 MeV/c. For the observed $pppn$ channel, the same energy

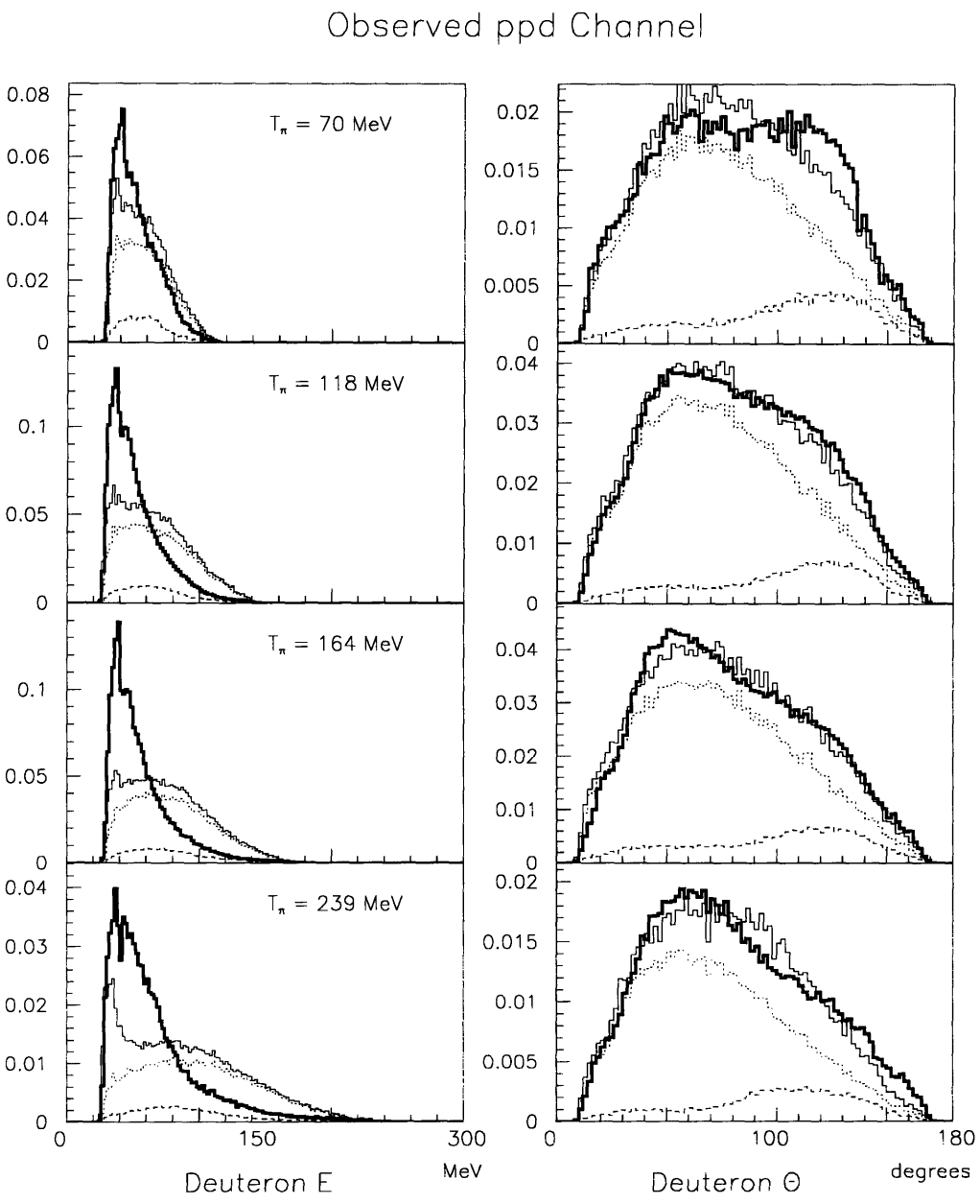

Figure 6-14: The LAB energy and θ distributions of the deuteron for the observed *ppd* channel. The dark solid line is the data, the lighter solid line is the simultaneous fit of Monte Carlo simulations. The dashed line is the assigned contribution from the $(pd)p$ channel and the dotted line is the assigned contribution from the (ppd) channel.

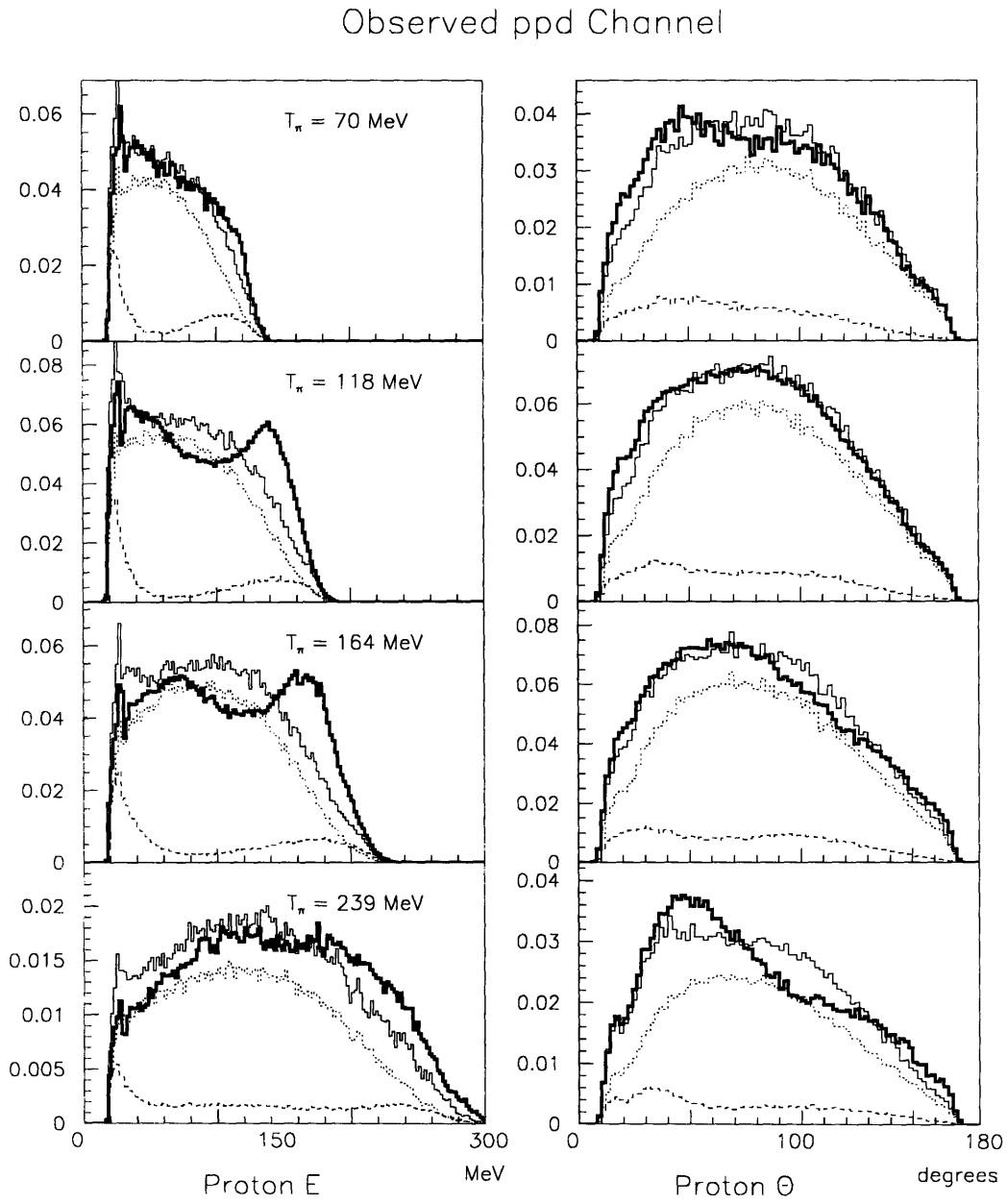

Figure 6-15: The LAB energy and θ distributions of the two protons for the observed *ppd* channel. The dark solid line is the data, the lighter solid line is the simultaneous fit of Monte Carlo simulations. The dashed line is the assigned contribution from the $(pd)p$ channel and the dotted line is the assigned contribution from the (ppd) channel.

thresholds and invariant missing mass cuts are applied, but the reconstructed momentum of the neutron is required to be above 250 MeV/c.

The simple phase space representations of the $(ppp)n$ and $(pppn)$ distributions appear to describe the data rather well. Figure 6-16 shows the LAB energy and θ distributions of the protons in the observed ppp and $pppn$ channels. The primary disagreement between experiment and simulations is evident in the angular distributions. The angular distributions of the data are more forward/backward peaked than the simulated distributions.

6.8 Observed ppn channel

The observed ppn channel consists of events from the pp charged detector in which there was also a neutron detected in the final state and no γs. Using the energy and angular information of the two protons and the angular information of the neutron as measured by the scintillators, the energy of the neutron and the energy and angles of the undetected proton are reconstructed. Thresholds are applied to the two detected protons and the reconstructed neutron energy of 30 MeV. If the momentum of the reconstructed proton is less than 250 MeV/c, then the event is considered a part of the observed ppn channel. The main contributions to the observed ppn channel are from the (ppn), $(pppn)$, and $(pp)pn$ physics channels. At the lowest energy, the contribution from $(ppp)n$ is also rather large.

The fit of the energy and angular distributions of the observed ppn channel is quite good, again with some discrepancies evident in the angular distributions (see Figure 6-17 and 6-18). The sharp jags at forward and backward angles in the neutron θ distributions comes from the fact that the z-position measurement is poorer in the endcap counters than in the cylinder.

6.9 Absorption on $T = 1$ pairs

Absorption on a $T = 1$ pair $(pn)pp$ should result in a highly energetic proton and a neutron detected in LADS. Because of the large pion scattering cross section, events in which there was only one charged particle detected by LADS were prescaled down to enhance the fraction of the data sample in which two and three charged particles were detected. Nevertheless, a

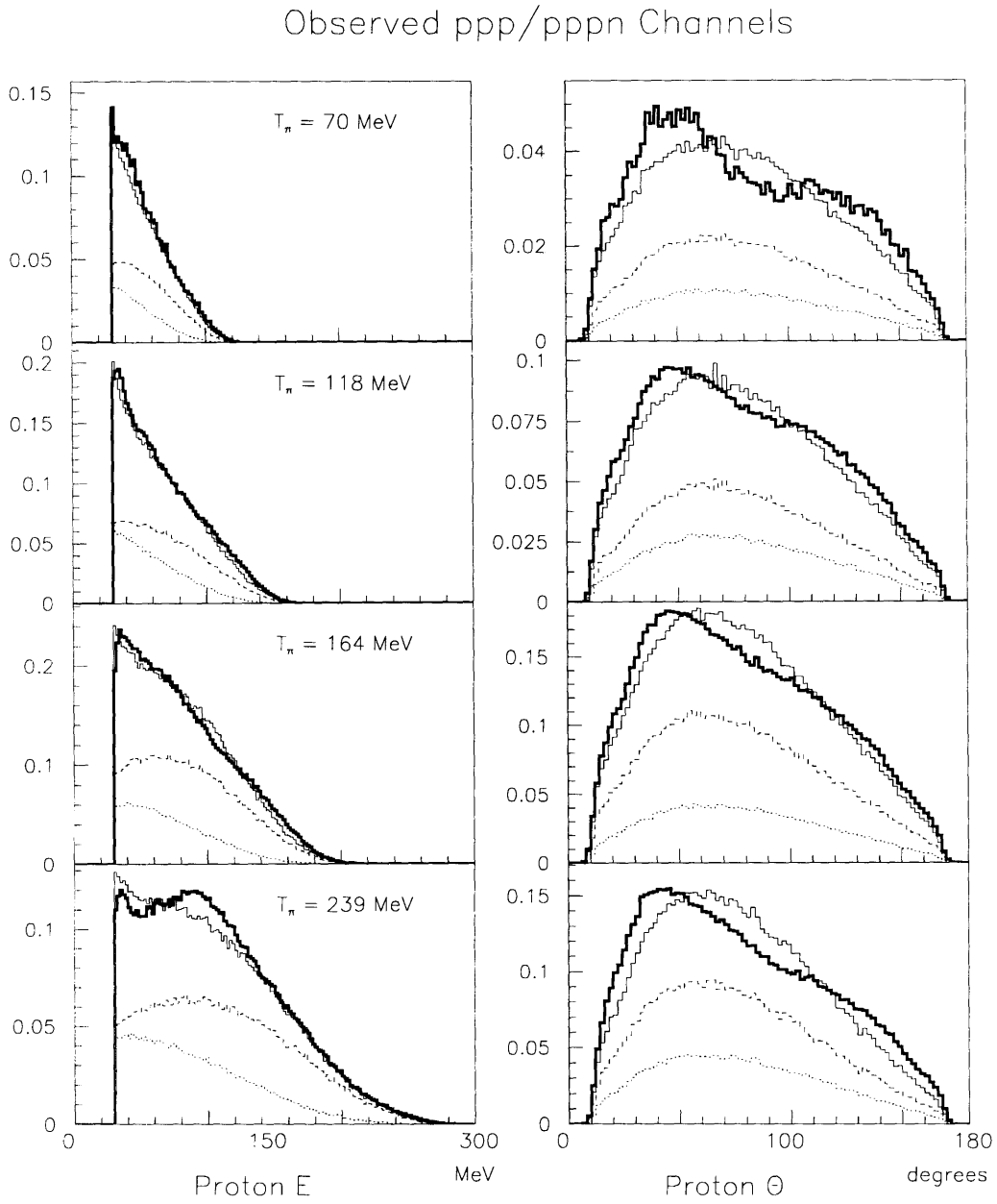

Figure 6-16: The LAB energy and θ distributions of the three protons for the observed *ppp* and *pppn* channels. The dark solid line is the data, the lighter solid line is the simultaneous fit of Monte Carlo simulations. The dashed line is the assigned contribution from the $(ppp)n$ channel and the dotted line is the assigned contribution from the $(pppn)$ channel.

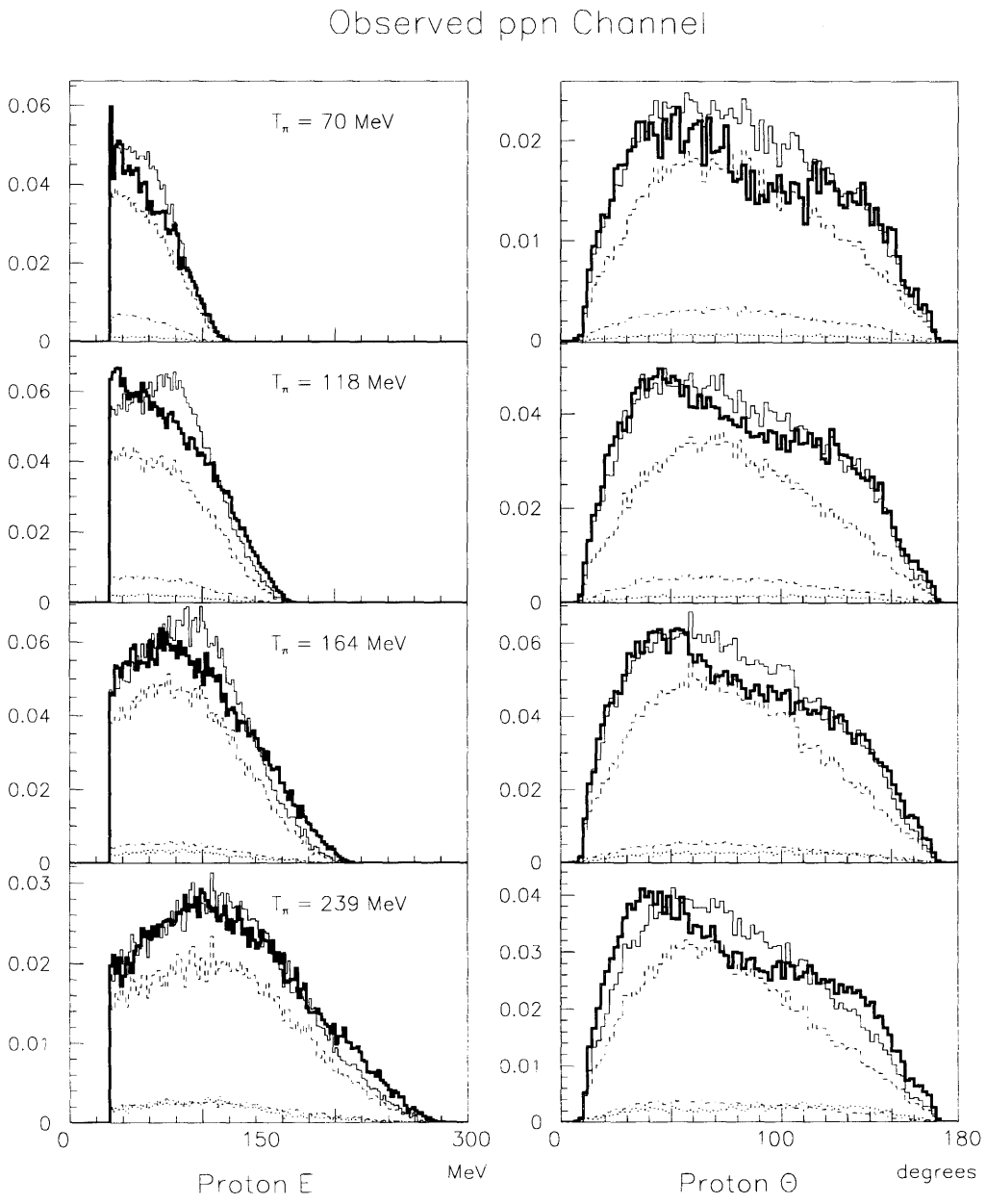

Figure 6-17: The LAB energy and θ distributions of the two protons from the observed *ppn* channel. The dark solid line is the data, the lighter solid line is the simultaneous fit of Monte Carlo simulations. The dashed line is the assigned contribution from the $(ppn)p$ channel, the dotted line from the $(ppp)n$ channel, and the dash-dotted line from the $(pppn)$ channel.

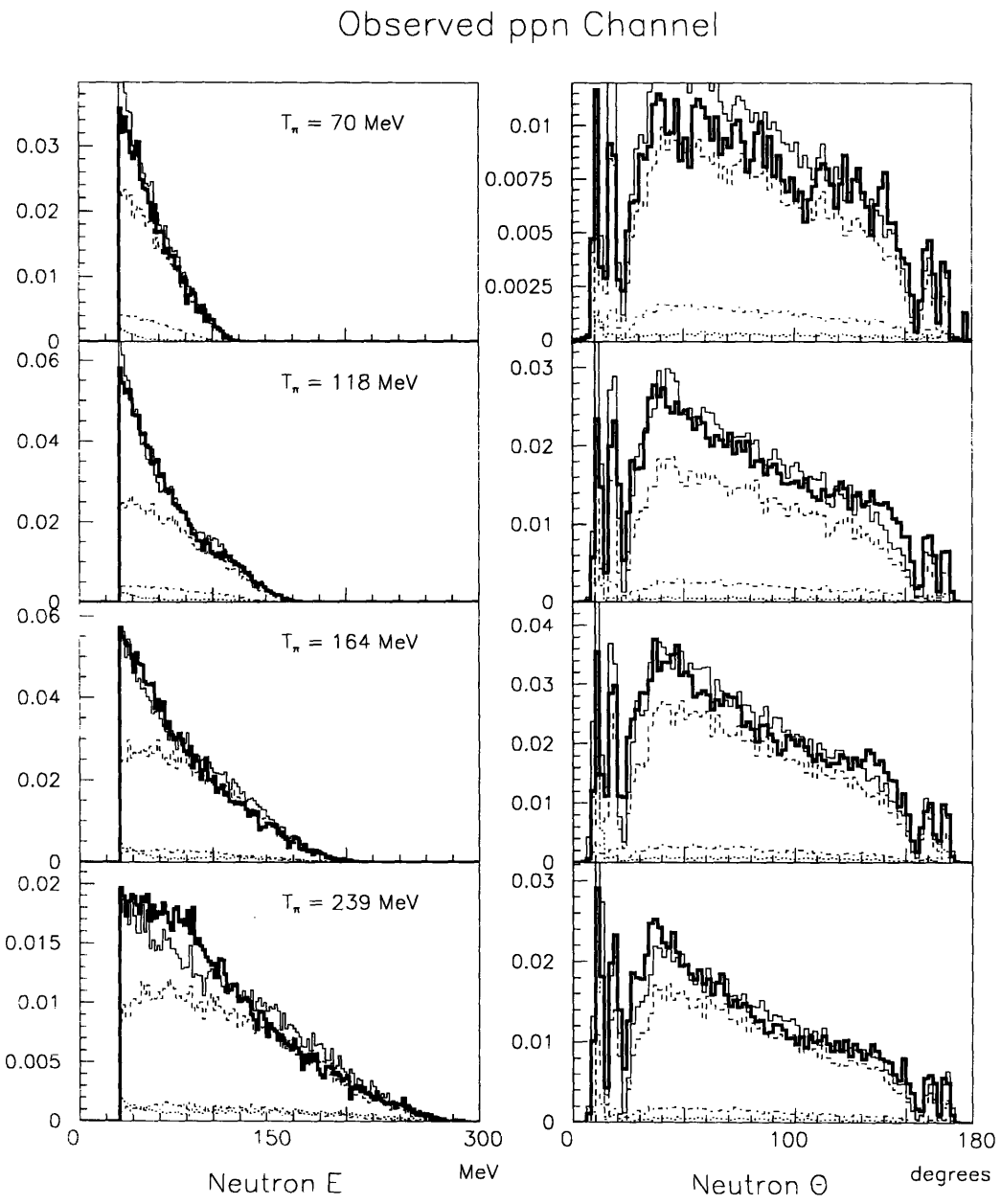

Figure 6-18: The LAB energy and θ distributions of the neutron from the observed *ppn* channel. The dark solid line is the data, the lighter solid line is the simultaneous fit of Monte Carlo simulations. The dashed line is the assigned contribution from the $(ppn)p$ channel, the dotted line from the $(ppp)n$ channel, and the dash-dotted line from the $(pppn)$ channel.

crude estimate of the contribution from the $(pn)pp$ channel can be made. Events are isolated in which there is a proton with energy of at least 70 MeV, a neutron, and no γ. If one neglects the initial momentum of the spectator pair, the energy of the neutron and the momentum vector of the spectator system can be calculated from the energy and angle of the observed proton and the angular information of the neutron as calculated from the TDCs. A cut is made on the missing momentum of the unobserved pair at 300 MeV/c to obtain the observed pn channel. Contributions from all competing absorption channels to the observed pn channel are subtracted. The resulting cross section is corrected assuming that the angular distribution of $T = 1$ absorption is roughly the same as $T = 0$ absorption, and then multiplied by a factor of 3 to take into account in a rough manner the neutron detection efficiency.

6.10 Breakup into physical channels

In order to obtain the total absorption cross section and the breakup into individual channels, one must determine the contributions of each of the physics channels to the cross sections in the observed channels. Histograms of kinematic quantities such as energy and angular distributions of the final state particles in the six observed channels are simultaneously fit with the seven Monte Carlo distributions. The breakup is accomplished using a χ^2-minimization of the form:

$$\chi^2 = \sum_i \frac{(DATA_i - \sum_j p_j \times MC_j)^2}{\sqrt{DATA_i}} \tag{6.1}$$

where the summation over j refers to the seven simulations, and the summation over i refers to the value calculated over each fitted bin. The square root of counts in the denominator of the expression is used to overweight the contribution of bins with more statistics. The free parameters which vary in the minimization are the p_j, which represent the contributions from each simulation. The results for the four energies are shown in Table 6.2.

6.11 Discussion of uncertainties

There are three major sources of uncertainty associated with the determination of the total absorption cross section. The first concerns beam and target normalization, which were discussed in the previous chapter. The second concerns normalization uncertainties associated

Physics Channel	70 MeV	118 MeV	164 MeV	239 MeV
(pp)d/pn	21.7 ± 3.3	30.4 ± 2.3	25.4 ± 2.4	10.4 ± 0.7
(ppn)p	3.6 ± 1.2	6.9 ± 0.7	7.5 ± 0.8	5.0 ± 0.4
(ppp)n	1.2 ± 0.3	2.2 ± 0.2	3.8 ± 0.3	3.4 ± 0.3
(pppn)	1.1 ± 0.4	2.0 ± 0.2	2.1 ± 0.2	2.1 ± 0.2
(pd)p	2.5 ± 0.4	2.4 ± 0.2	1.8 ± 0.2	0.7 ± 0.1
(ppd)	2.1 ± 0.3	3.4 ± 0.3	3.5 ± 0.3	1.3 ± 0.1
T=1 (est.)	1.0 ± 0.5	2.3 ± 1.1	2.2 ± 1.1	1.0 ± 0.5
Total	33.1 ± 5.0	49.5 ± 3.6	46.2 ± 4.1	23.8 ± 1.6

Table 6.2: Breakup of total absorption cross section into physics channels.

with corrections made using the Monte Carlo simulation for the treatment of wire chamber efficiencies and reaction corrections. In the cases of the neutron detected channels, the uncertainty associated with the simulation of neutron detection must also be folded in.

The final uncertainty, which is the most difficult to assess, is associated with the fit procedure used to determine the breakup. To understand the uncertainties associated with the fit procedure, the analysis was conducted with tighter and looser cuts than taken in the standard analysis. Investigations were also conducted to determine the sensitivity of the breakup to the particular sets of histograms used in the fit. The measurement of the total absorption cross section appeared highly insensitive to these changes.

The form of the spectator momentum distribution used was part of the assumption of the models of the absorption processes, and is not included in the assessed uncertainties. The strength of the tail of the spectator momentum does not greatly affect the determination of the total absorption cross section, but is important in the determination of the breakup into reaction channels. To examine the effect of changes in the strength of the spectator tail, the QDA strength was fixed at higher and lower values than the best fit value, and the effect on the multi-nucleon channels was examined. Making the tail larger tended to remove strength from the multi-nucleon channels, with the largest effect on the $(ppn)p$ channel. Similarly, reducing the strength of the tail tended to increase the multi-nucleon strength, again with the largest fractional increase in the $(ppn)p$ channel.

Chapter 7

Differential Distributions and Model Dependent Decomposition

In this chapter, differential distributions for the multi-particle final states are presented, along with a model dependent decomposition of the total absorption cross section. Differential distributions are presented for the observed *ppp*, *ppn*, *pppn*, and *ppd* channels. The distributions for the observed two nucleon final states *pp* and *pd* were presented in the last chapter during the discussion of the breakup into physical channels. The subdivision into physical channels presented in the last chapter was based on the number and type of particles which were believed to have participated in the reaction, and the number and type of spectators. The decomposition of the total absorption cross section into various channels can be considered on several levels (see Figure 7-1). The first level of decomposition is the separation of undisturbed QDA from all other processes. The undisturbed QDA can be further subdivided into a final state in which there is a deuteron as a spectator, $(pp)d$, and a final state in which there is an unbound pn-pair, $(pp)pn$. The non-QDA portion of the cross section can be decomposed into three parts, absorption on a $T = 1$ pair, multi-nucleon processes in which there are four particles in the final state, $\sigma^{\mathrm{pppn}}_{\mathrm{non-QDA}}$, and multi-nucleon processes in which there are three particles in the final state, $\sigma^{\mathrm{ppd}}_{\mathrm{non-QDA}}$. In the decomposition presented in the last chapter, these cross sections were subdivided into $(ppn)p$, $(ppp)n$, $(pppn)$, $(pd)p$, and (ppd) physics channels. No attempt was made to separate these final states by mechanism. In order to proceed further in the decomposition and attribute the multi-nucleon absorption yields to various mechanisms, one needs to include reasonable models of mechanisms which one believes should contribute to the total cross section.

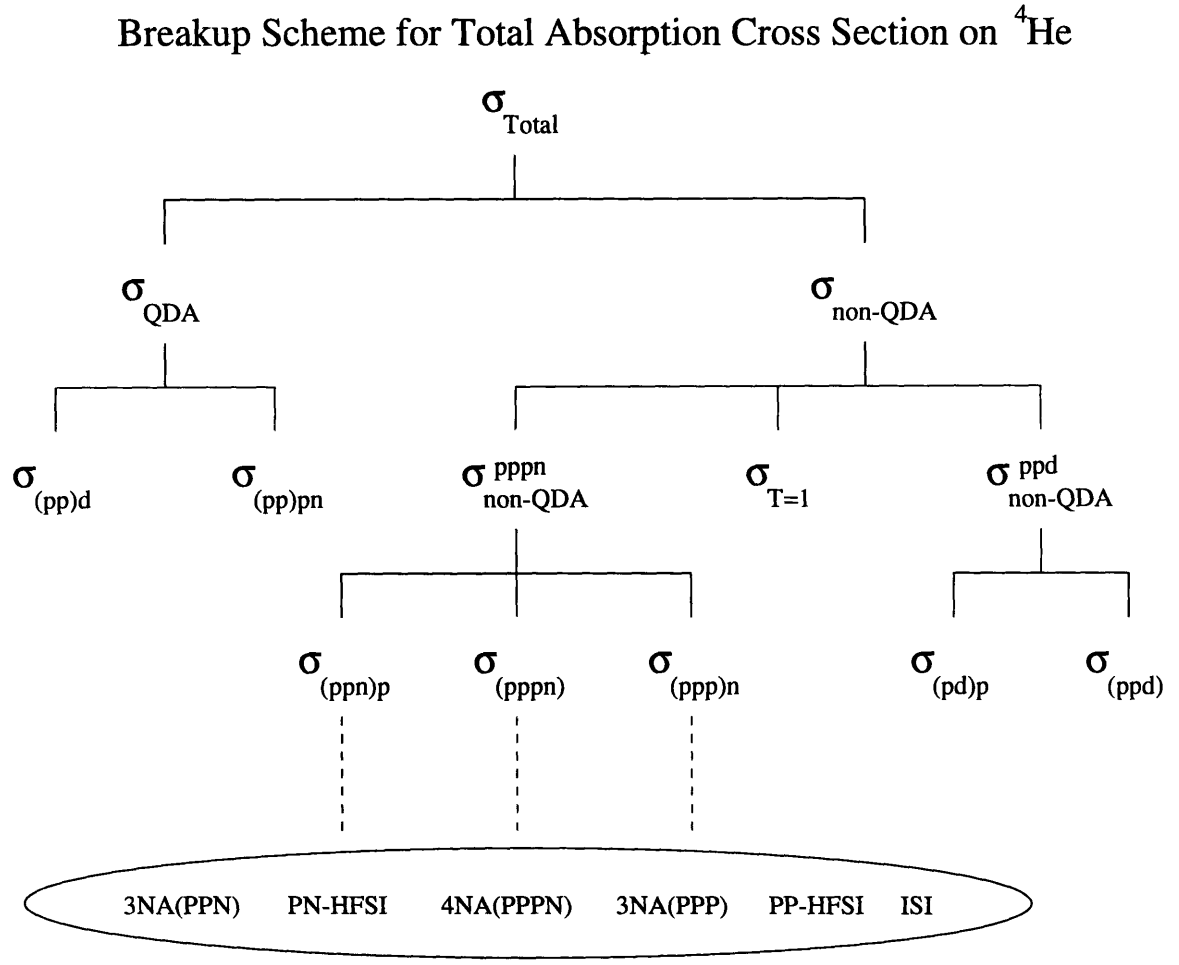

Figure 7-1: A depiction of the way the total absorption cross section on ^{4}He can be decomposed.

ISI Channel	p	p	p	n
$(\pi^+, \mathrm{p} \rightarrow \pi^+, \mathrm{p}) + QFA(\pi^+, \mathrm{pn})$	High	High	Scatter	Fermi
$(\pi^+, \mathrm{n} \rightarrow \pi^+, \mathrm{n}) + QFA(\pi^+, \mathrm{pn})$	High	High	Fermi	Scatter
$(\pi^+, \mathrm{n} \rightarrow \pi^0, \mathrm{p}) + ABS(\pi^0, \mathrm{pp})$	High	High	Fermi	Scatter
$(\pi^+, \mathrm{n} \rightarrow \pi^0, \mathrm{p}) + ABS(\pi^0, \mathrm{pn})$	High	High	Fermi	Scatter
FSI Channel	p	p	p	n
$QFA(\pi^+, \mathrm{pn}) + \mathrm{pp}$	High	Medium	Medium	Fermi
$QFA(\pi^+, \mathrm{pn}) + \mathrm{pn}$	High	Medium	Fermi	Medium

Table 7.1: ISI and FSI channels which were considered for Monte Carlo. The designations assigned to the three protons and the neutrons are to give a rough idea of what the distributions for each channel should look like. "High" means that the nucleon should have nearly half of the available energy. "Scatter" means that the nucleon should look as though it came from an initial state scatter with the incident pion. "Fermi" means that the energy distribution should look like a spectator distribution. "Medium" means that the nucleon should have roughly one quarter of the available energy.

7.1 Processes Included in the Model Dependent Breakup

Two types of multi-step processes are believed to contribute to the total absorption cross section: processes in which there is an initial state interaction followed by absorption (ISI), and processes in which there is a hard final state interaction between nucleons following the absorption. There are three possible scenarios which one might consider when trying to model ISI. They are summarized in Table 7.1. Since $T = 0$ absorption dominates over $T = 1$ absorption in the free case, one expects that if an initial scatter with a nucleon occurs, the dominant absorption process will be $T = 0$ absorption. The scattering off a neutron should be less important by a factor of nine at the resonance because of isospin than an initial scatter from a proton. The charge exchange reaction should be similarly suppressed in comparison to the proton scattering channel by a factor of 4.5. A charge exchange on a neutron would require the absorption of a π^0. There are two possible scenarios which one must consider after charge exchange, an absorption on a *pp*-pair, and absorption on a *pn*-pair. The cross section for the absorption of a π^0 by a *pn* pair is a factor of 2 smaller than the absorption of a π^+ by a *pn*-pair, so this channel may be ignored. The differential distributions of a charge exchange followed by an absorption on a *pp*-pair would be indistinguishable from scattering from a proton and followed by QFA, so this process is not modelled.

There are two kinds of hard final state interactions which can occur, a final state interaction between a proton and a neutron (PN-HFSI), and a final state interaction between two protons (PP-HFSI). Both possibilities are modelled.

Cases in which both an ISI and FSI occurred have been omitted for the sake of simplicity. The contribution from such processes should in any case be quite small for ^{4}He. Soft final state interactions (SFSI) have a tendency to modify final state distributions by enhancing regions in which two nucleons are emitted colinearly. The effect of adding soft final state interactions to various generators was examined, but did not appear to have a measurable effect on the decomposition into different channels.

To simulate one-step absorption processes, pure phase space simulators are modified to include the effects of the pion bringing in angular momentum during the absorption. The process by which this is accomplished will be described in a later section. To obtain better agreement for the observed *ppd* channel, additional modifications are needed. These will also be described in a later section.

7.2 Useful Kinematic Quantities

Before proceeding to present the various differential distributions, kinematic variables which are useful for understanding the multi-particle final states are described briefly. For a three-body final state, there are 5 independent variables, which once specified, completely describe the final state. It is simplest to work in the center-of-mass system of the three outgoing particles. A useful set of variables in describing a three particle final state are the Euler angles (see Figure 7-2). These angles specify the orientation of the plane formed by the outgoing particles in their CM system. The polar angle of the normal of the plane with respect to the beam axis is called the plane angle, ξ. The rotation of the plane about the normal, can be specified by the angle between the momentum of one particle, say the least energetic, and the projection of the beam axis onto the plane of the three particles. This angle will be referred to henceforth as γ_1. The final Euler angle, the azimuthal angle of the normal of the plane, is referred to as β. Because there are no polarizations in the experiment, the angle β is integrated over in this measurement. Hence, a three-body final state can be completely described by four variables.

To completely describe the system one may choose the set of variables $(\xi, \gamma_1, \psi_{min}, \psi_{max})$, where ψ_{min} and ψ_{max} are the minimum and maximum opening angles between the three particles. Alternatively, one could choose the set $(\xi, \gamma_1, E_1, E_2)$. Although both of these variable

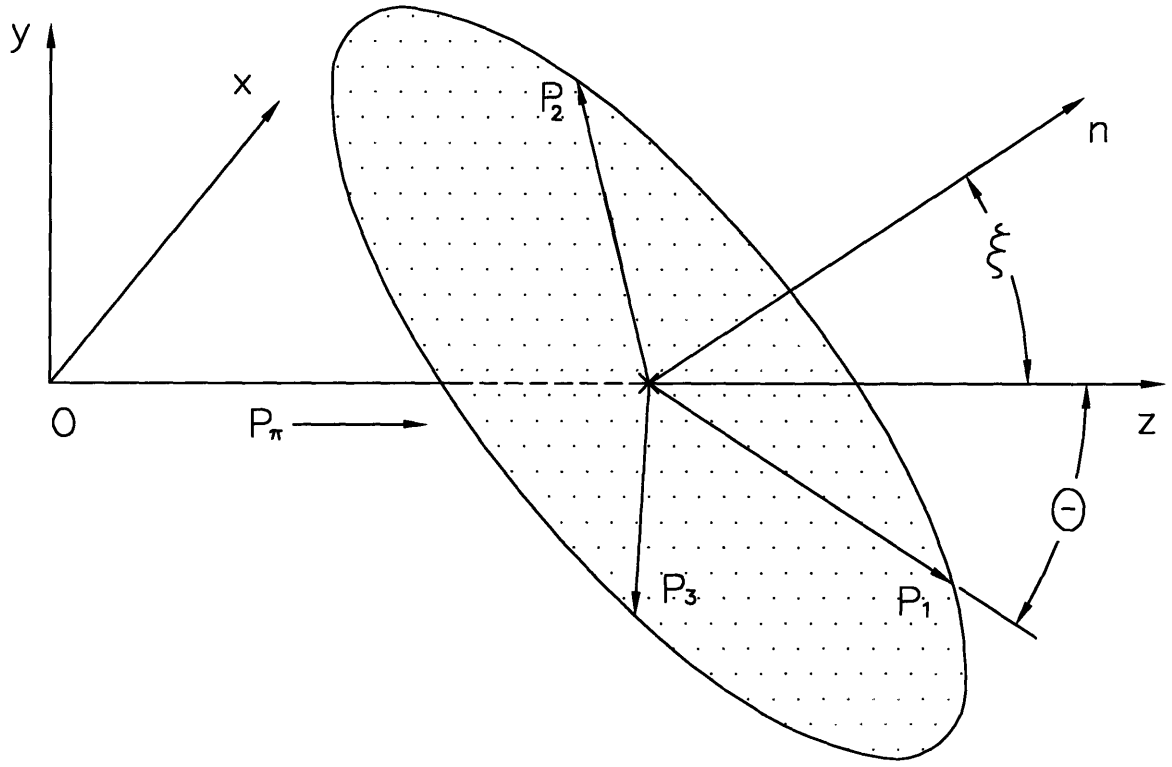

Figure 7-2: A diagram of the Euler angles which can be used in the description of the kinematics of a three-body final state.

sets completely describe the system, other variables may be useful to examine because they display certain features of particular mechanisms prominently.

In the case of a four-body system, three additional variables are needed to completely describe the system. One can again choose to work in the CM frame of three of the four particles and use one of the four-variable sets described above. The remaining three variables can be taken to be the magnitude of the momentum of the fourth particle in the CM frame of the other three particles, the opening angle between the momentum vector and the normal to the plane formed by the other three particles, and the γ angle of the projection of the momentum of the fourth particle on the plane of the other three particles.

A particularly useful quantity for determining whether or not ISI contributes to multi-nucleon absorption is the pseudo-invariant mass squared m_x^2 which was introduced by Salcedo et al. [58]. The pseudo-invariant mass squared is defined as

$$m_{x_{ij}}^2 = (T_i + T_j)^2 - (\vec{p_i} - \vec{p_j})^2 \tag{7.1}$$

where i and j are the indices of two of the final state particles. In the fixed scatterer approximation, the pseudo-invariant mass squared is equal to the square of the mass of the exchange particle which is absorbed regardless of whether or not the particle has had interactions with other particles before the absorption. The initial momentum of the nucleons tend to smear out any features in the pseudo-invariant mass squared distributions. An added complication arises from the fact that the particles are indistinguishable, and hence one cannot tell which pair of particles the absorption took place on. Thus, in the the pseudo-invariant mass squared distributions which are presented, all permutations of particles are plotted.

7.3 The Observed *ppp* Channel

In this section differential distributions from the observed *ppp* channel are presented. In the breakup into physical channels, it was noted that there was fairly good agreement between the pure phase space simulations and the data. The primary discrepancy was visible in the θ distributions of the outgoing protons. Part of the reason for this discrepancy is that the effects of angular momentum have not been included in the phase space simulations. The plane angle distribution is sensitive to the angular momentum content of the final state. To include

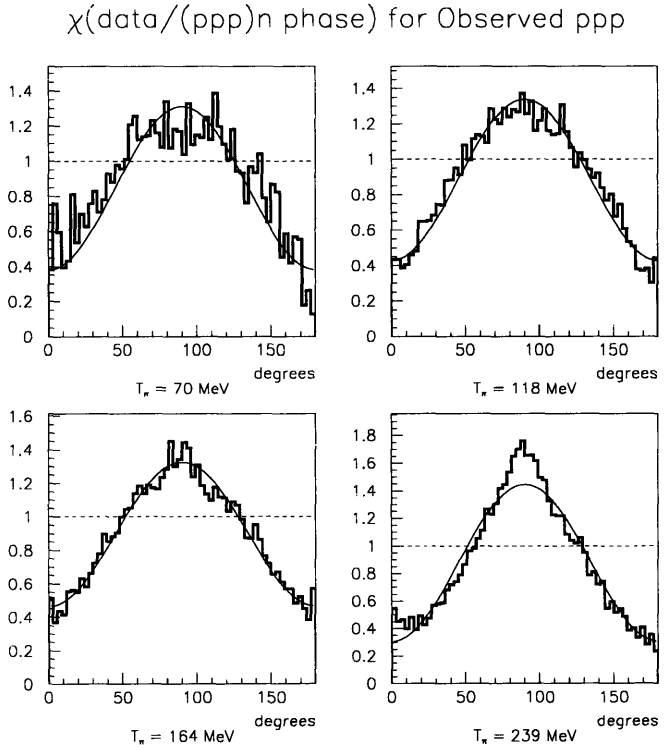

Figure 7-3: This figure shows the deviation of the data distributions from a flat $l = 0$ phase space distribution. If the data were distributed as $l = 0$ phase space, the result of the division by phase space would be a horizontal line.

the angular momentum components, one needs to modify the phase space event generators. This may be accomplished by measuring the angular momentum content of the final state by dividing the data distribution by phase space, and then parametrizing the result using a Legendre polynomial (see Figure 7-3). The phase space events can then be weighted by this parametrization. The explicit inclusion of angular momentum is only necessary in the case of the phase space simulations. It is included implicitly in the two-step ISI and FSI generators through the Ritchie parametrization in the absorption step.

The plane angle in the CM system of the three protons for the observed *ppp* channel is used to measure the angular momentum content of the final state. The observed ξ distribution is divided by the $(ppp)n$ phase space ξ distribution. The resulting simulation is called the 3NA(*ppp*) generator. For the *ppn* generator, the angular momentum content of the final state

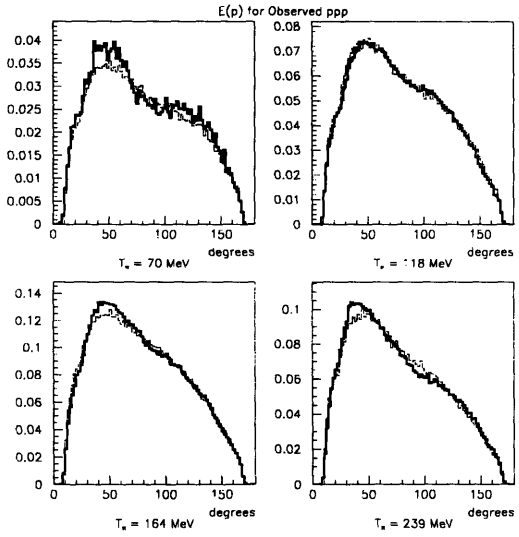

Figure 7-4: The LAB θ of protons in the observed *ppp* and *pppn* channels. The dark solid line is the data distribution and the lighter solid line is the sum of the contributions from all Monte Carlo simulations.

is assumed to be the same as in the *ppp* case, with a neutron replacing one of the protons. The resulting simulation is called the 3NA(*ppn*) generator. For a four-body process, it is not clear how to correctly include the effect of angular momentum, so no correction is included. For the (*ppd*) generator the same prescription is followed using the observed *ppd* channel. Additional modifications are also made in an attempt to match the data distributions more closely. After the inclusion of angular momentum, the θ distributions of the data can be well described by the simulations (see Figure 7-4).

Distributions of the four independent variables for a three-body final state for the observed *ppp* channel are shown in Figure 7-5. Good agreement is in general obtainable for all distributions from the simultaneous fit except the γ distributions. The γ of the lowest energy proton shows peaking in the forward direction which appears to become stronger as the incident pion kinetic energy is increased. The dip in the region of 0° is due to a hole in the acceptance coming from the exit hole for the beam in the downstream endcap. The ISI simulation is the process which most strongly populates the forward regions in γ. The failure to reproduce the shape of the γ_1 distribution in the *ppp* channel suggests a deficiency in the classical ISI simulation.

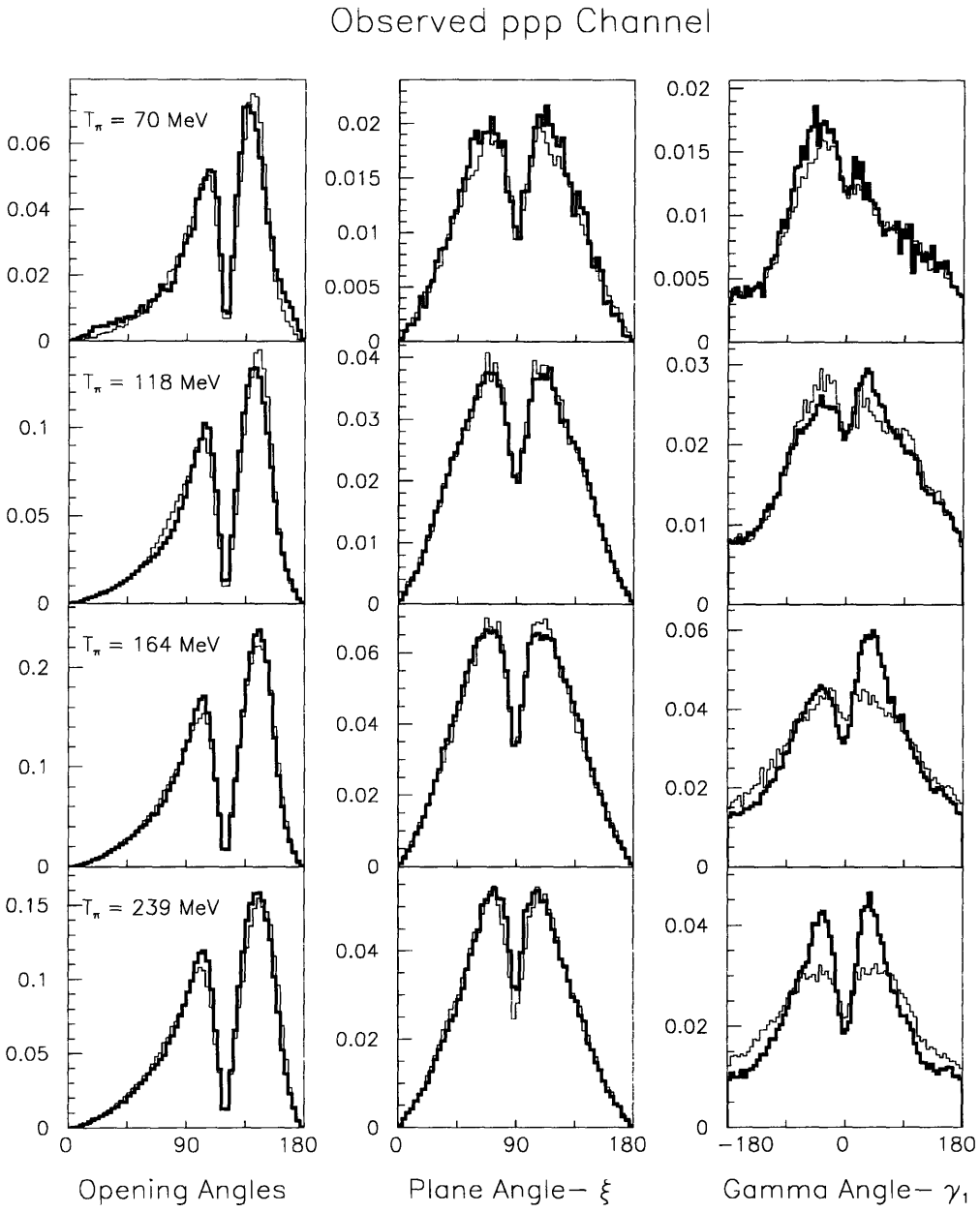

Figure 7-5: This figure shows the four independent variables for the observed *ppp* channel. The first column contains the minimum and maximum opening angles. The second column shows the plane angle, and the last column the γ angle of the least energetic proton. In all cases, the dark solid line indicates the data distribution while the lighter solid line is the sum of the contributions from all Monte Carlo simulations.

The signatures of various processes can be seen by looking at the θ *vs.* momentum distributions of the three protons detected in the observed *ppp* channel. Figure 7-6 shows the data distributions of the θ-p correlation at the four measured energies. An enhancement is clearly visible near the kinematics of free π-p scattering at the highest two energies, suggesting contributions from ISI. Comparisons of the data with various simulations of the θ-p distributions are shown in Figures 7-7 and 7-8 for incident pion kinetic energies of 118 and 239 MeV. In the case of the 118 MeV data, the data distribution shows some similarity to that obtained for the PP-HFSI simulation. It appears that at lower incident pion kinetic energies, the primary contributions to the observed *ppp* channel are the 3NA(*ppp*) and PP-HFSI channels. At 239 MeV, the data distribution does not bear very much similarity to the PP-HFSI distribution but instead appears to be a combination of 3NA(*ppp*) and ISI. Signs of ISI can also be seen in the pseudo-invariant mass squared distributions (see Figure 7-9). A small peak at a value slightly lower than the pion mass, which can only be filled by the ISI type process, is visible at the highest incident pion energy. As the pion energy is decreased, the apparent strength of the process diminishes. At 118 MeV, the peak can no longer be seen.

7.4 The Observed *ppn* Channel

For the observed *ppn* channel as mentioned in the previous chapter, the final state is reconstructed from the energy and angular information of the protons and the angular information of the neutron. In the distributions presented here, the neutron and two protons are not distinguished from one another. Instead they are energy ordered. The best fits to the observed *ppn* channel are displayed in Figure 7-10.

Quite good agreement is seen between the measured distributions and the simulations. In particular, the agreement with the γ_1 angle appears much better than could be obtained for the observed *ppp* channel. In the case of the observed *ppp* channel, the γ_1 distributions appeared to show a peaking behavior at small angles which increased as the incident pion kinetic energy increased. The 70 MeV γ_1 distribution for the observed *ppn* channel looks similar to the observed *ppp* channel. However, as the incident pion kinetic energy rises, the forward peaking evident in γ_1 for the observed *ppp* channel does not appear in the observed *ppn* channel. This observation is consistent with the expectation that in the observed *ppp* channels, at high incident pion energy, one sees contributions from ISI. In the case of the observed *ppn* channel, since the π^+-n scattering cross section is a factor of nine smaller than the π^+-p scattering cross section, contributions from ISI as manifested by a forward going neutron are not seen.

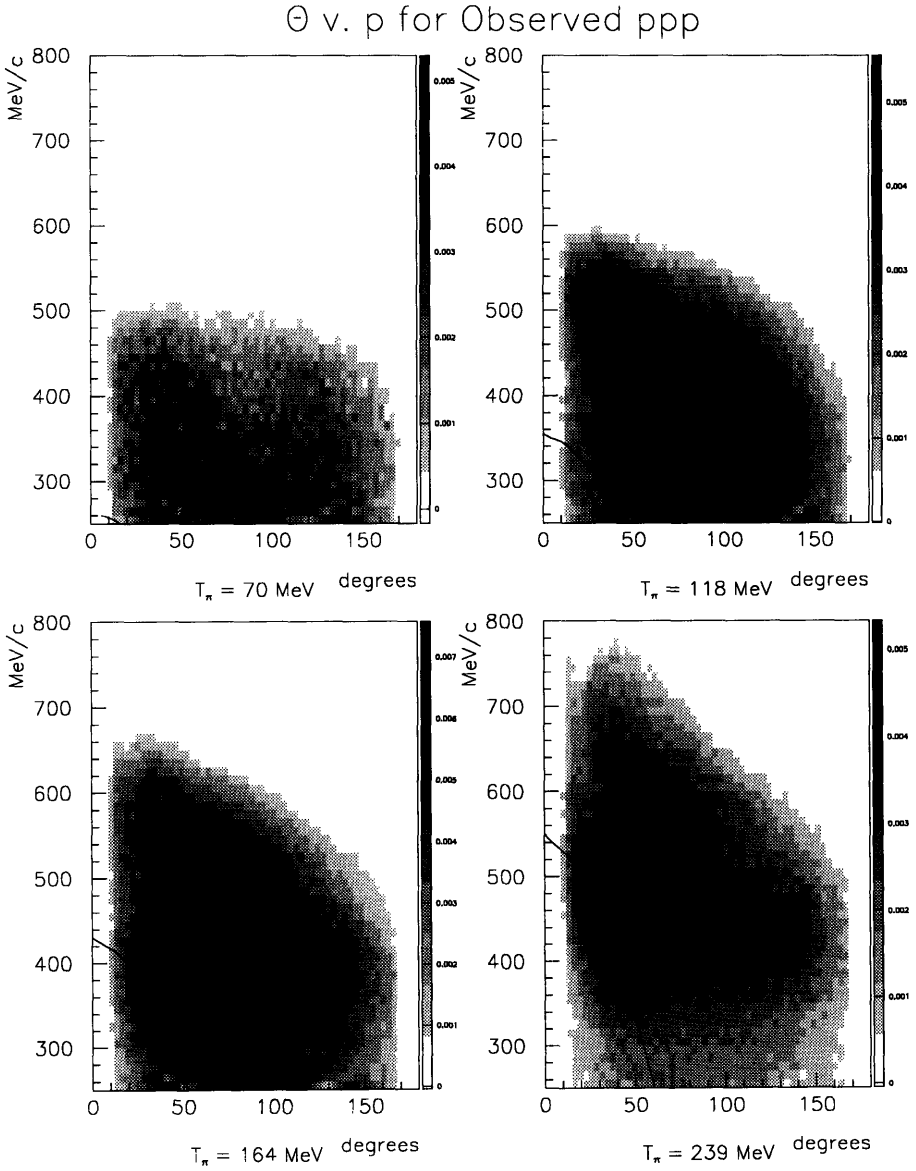

Figure 7-6: The θ-momentum correlation for three protons in the observed *ppp* channel. All three protons are plotted. The solid line indicates the kinematics for π-p scattering.

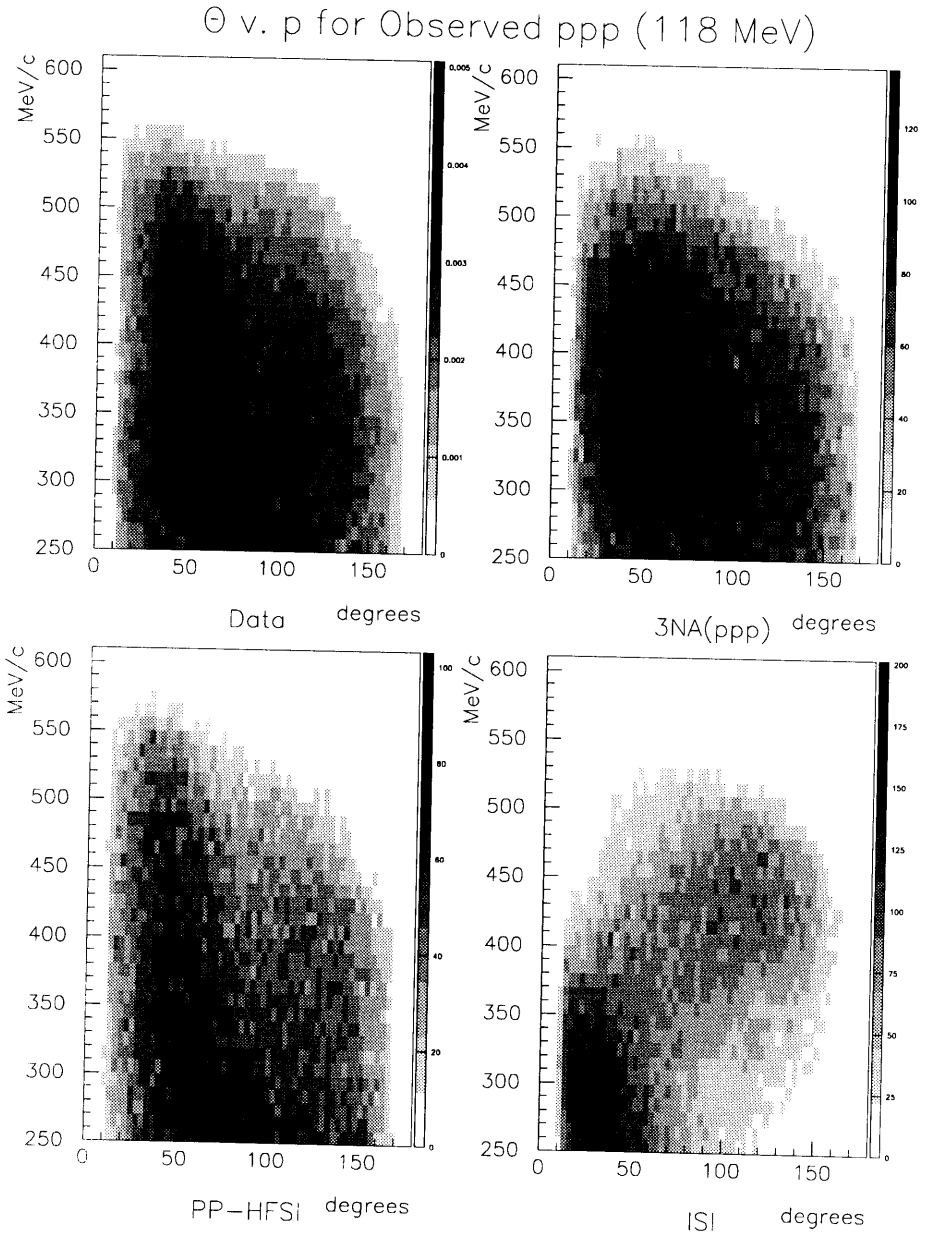

Figure 7-7: A comparison of the θ-momentum correlation for the three protons in the observed *ppp* channel at T_π = 118 MeV. The top left shows the data distribution, the top right the 3NA(*ppp*) distribution, the bottom right the PP-HFSI distribution, and the bottom left the ISI distribution.

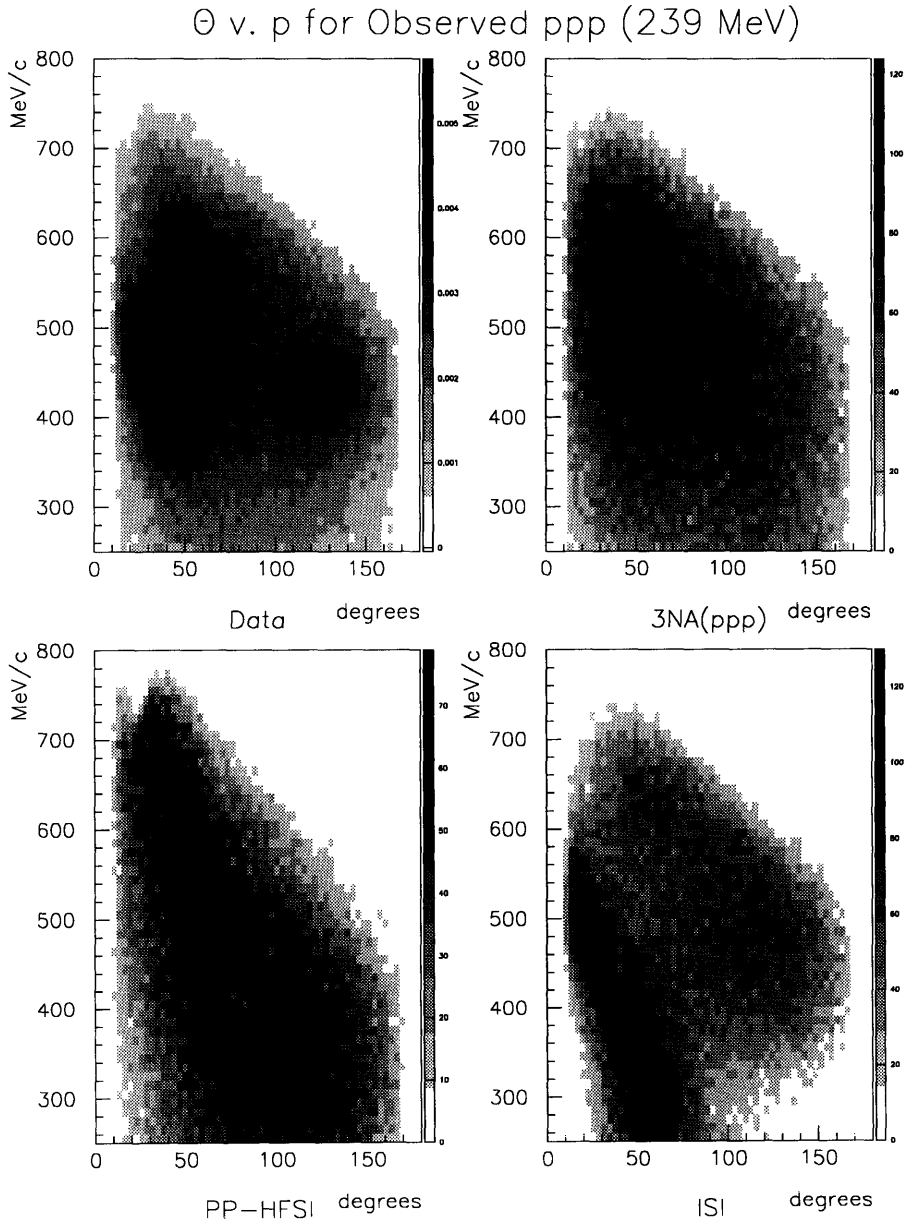

Figure 7-8: A comparison of the θ-momentum correlation for the three protons in the observed *ppp* channel at $T_\pi = 239$ MeV. The top left shows the data distribution, the top right the 3NA(*ppp*) distribution, the bottom right the PP-HFSI distribution, and the bottom left the ISI distribution.

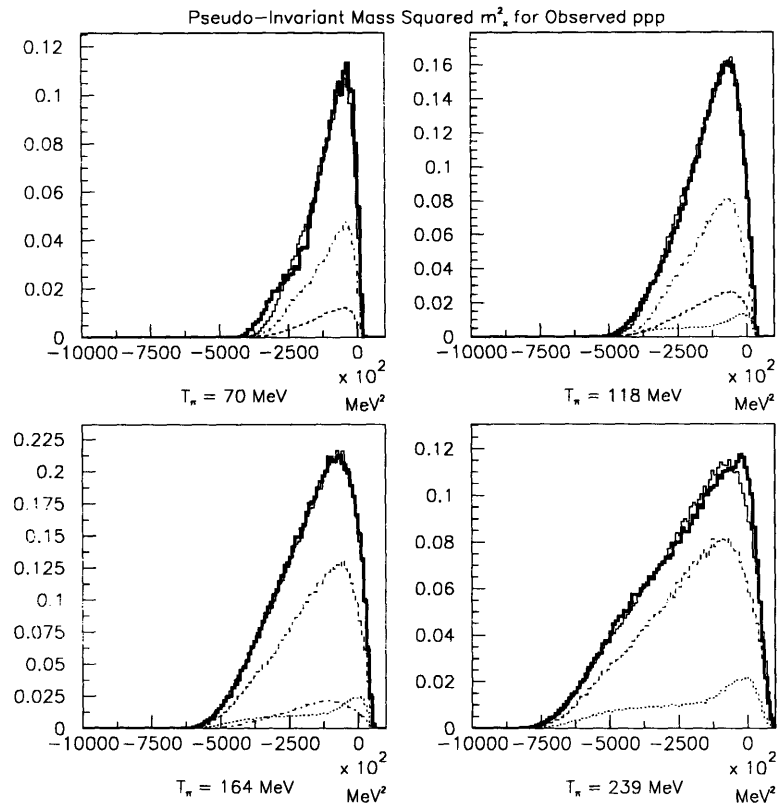

Figure 7-9: The pseudo-invariant mass reconstructed between each pair of protons in the observed *ppp* channel. The dark solid line is the data distribution and the lighter solid line is the sum of the contributions from all Monte Carlo simulations. The dotted line shows the contribution from ISI, the dashed line the contribution from 3NA(*ppp*), and the dash-dotted line the contribution from PP-HFSI.

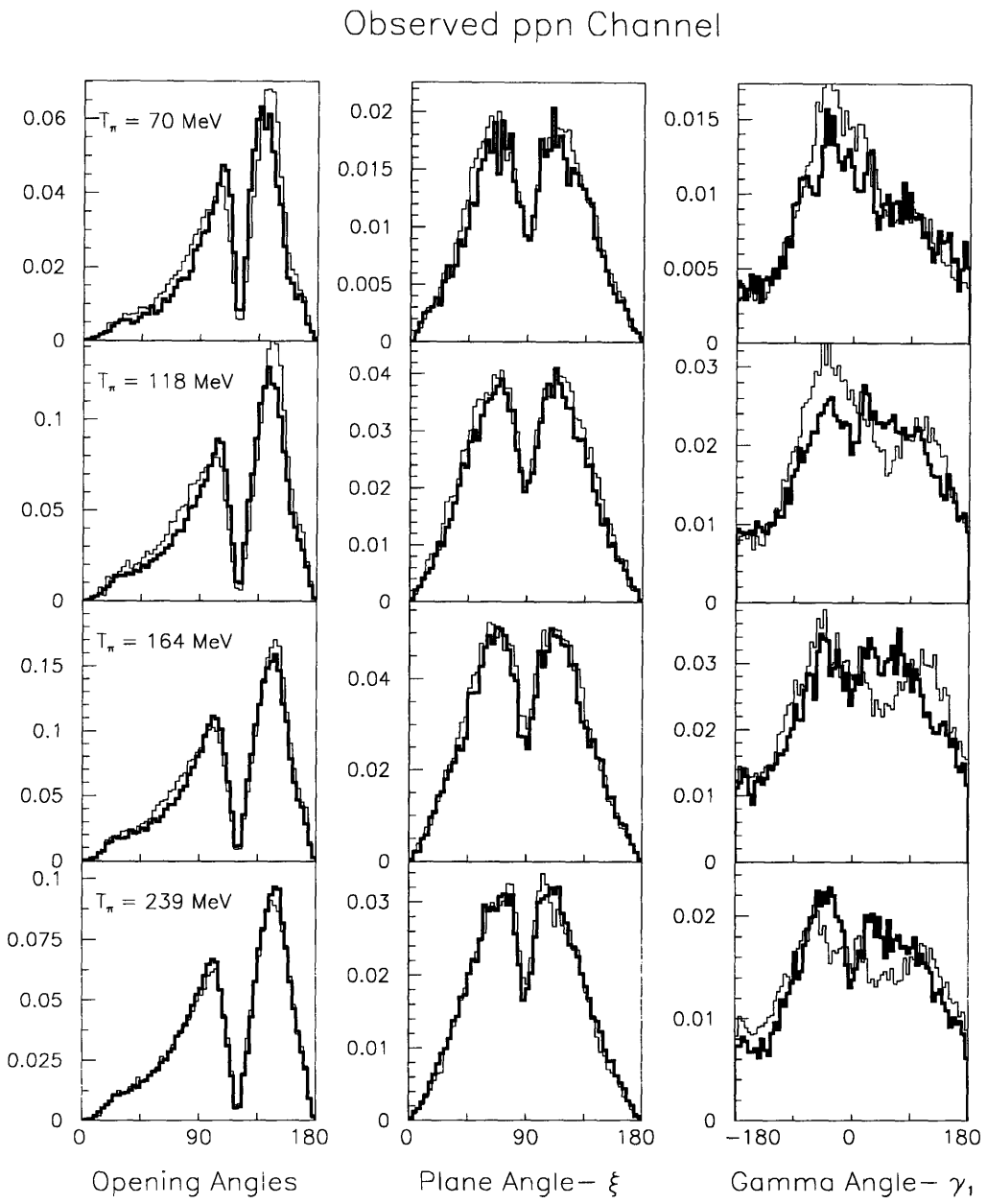

Figure 7-10: This figure shows the four independent variables for the observed *ppn* channel. The first column contains the minimum and maximum opening angles. The second column shows the plane angle, and the last column the γ angle of the least energetic nucleon. In all cases, the dark solid line indicates the data distribution while the lighter solid line is the sum of the contributions from all Monte Carlo simulations.

The θ-momentum correlation for the three final state nucleons in the observed *ppn* channel is plotted in Figure 7-11 at all four incident pion kinetic energies. No strong enhancement is seen in the observed *ppn* distributions at the quasifree scattering kinematics. Figures 7-12 and 7-13 show a comparison of the data with various simulations of the θ-p distributions for incident pion kinetic energies of 118 and 239 MeV for the observed *ppn* channel. The 118 MeV data distribution appears to be primarily composed of contributions from PN-HFSI and 3NA(*ppn*). At 239 MeV, the data distribution looks quite similar to 3NA(*ppn*) and does not bear very much similarity to the hard-FSI distributions.

7.5 The Observed *pppn* Channel

The strength of the observed *pppn* channel is too large to be explainable by either 3NA(*ppp*) or 3NA(*ppn*) because for each of these processes there is typically one low momentum nucleon. The (*pppn*) generator seems to reproduce the distributions of the observed *pppn* channel adequately. No significant deviations from phase space are seen in the observed *pppn* channel. The fit to the set of seven independent variables is displayed in Figures 7-14 and 7-15. The sharp peaking in the opening angle between the neutron and the normal to the reaction plane at 90° is caused by deuterons misidentified as protons. As was mentioned previously, the Monte Carlo simulation underpredicts the probability of misidentification of deuterons as protons.

7.6 The Observed *ppd* Channel

The multi-particle final state which is least well described by a phase space like distribution is the observed *ppd* channel. As was mentioned in the previous chapter, large discrepancies are visible between phase space and the data distributions, particularly in the deuteron energy spectra. The low and high energy proton peaks also cannot be described by the simulations.

In order to obtain better agreement between the models and the data, modifications are made to the (*ppd*) generator. The modifications are a generalization of the modifications made in creating the 3NA(*ppp*) and 3NA(*ppn*) generators. As mentioned previously, for a three-body final state such as *ppd*, four independent variables are needed to completely specify the system. To modify the phase space (*ppd*) generator so that it mimics the observed *ppd* final state, the

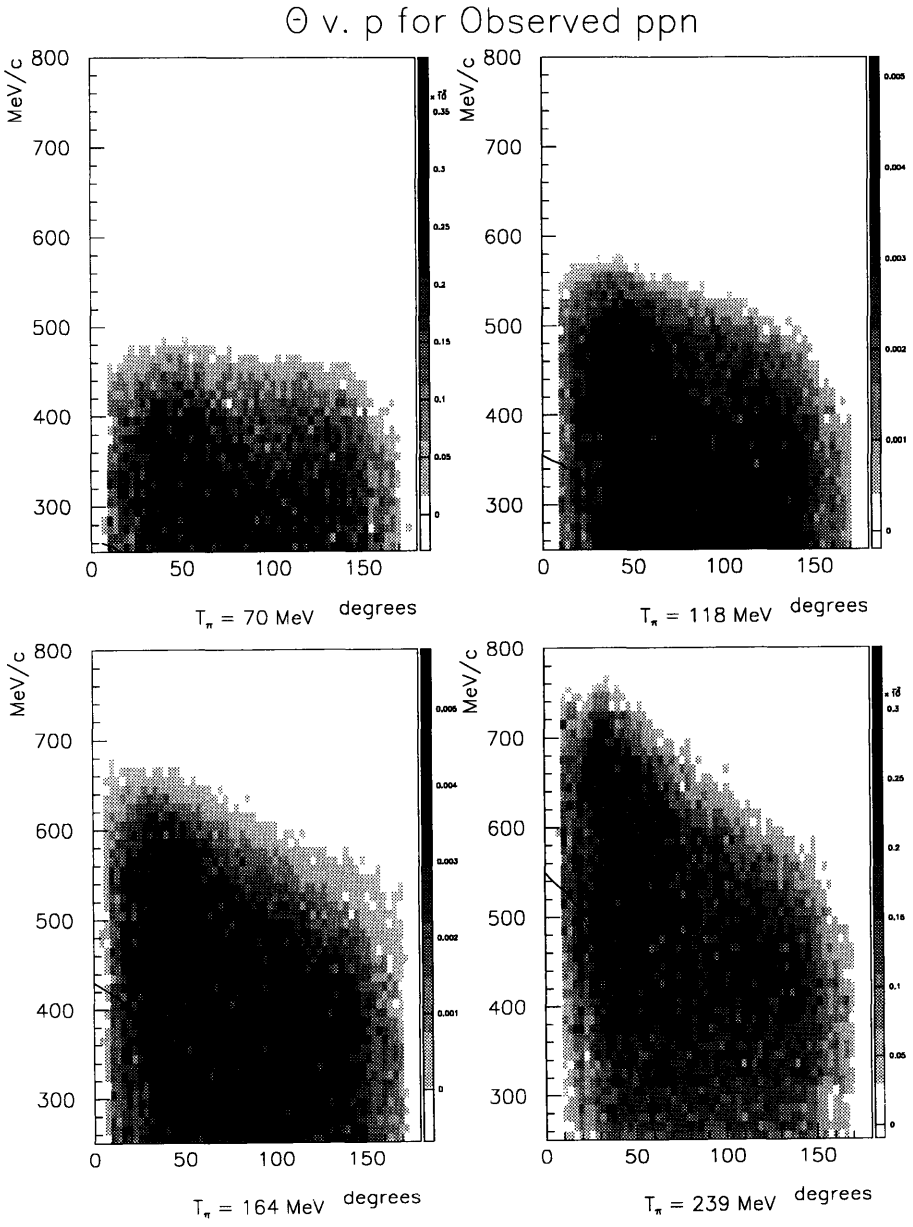

Figure 7-11: The θ-momentum correlation for two protons and the neutron in the observed *ppn* channel. The solid line indicates the kinematics for π-p scattering.

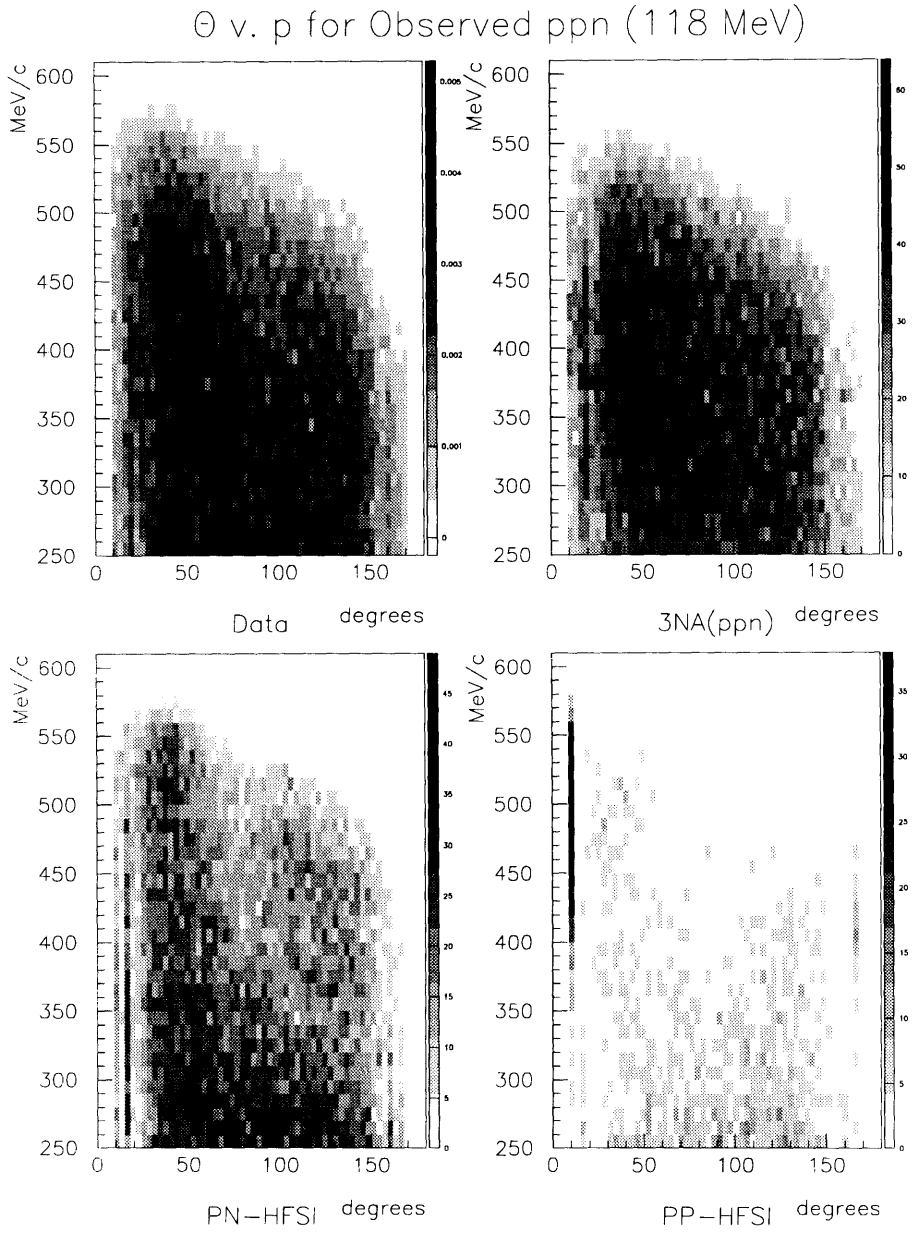

Figure 7-12: A comparison of the θ-momentum correlation for the three nucleons in the observed *ppn* channel at T_π = 118 MeV. The top left shows the data distribution, the top right the 3NA(*ppn*) distribution, the bottom right the PN-HFSI distribution, and the bottom left the PP-HFSI distribution.

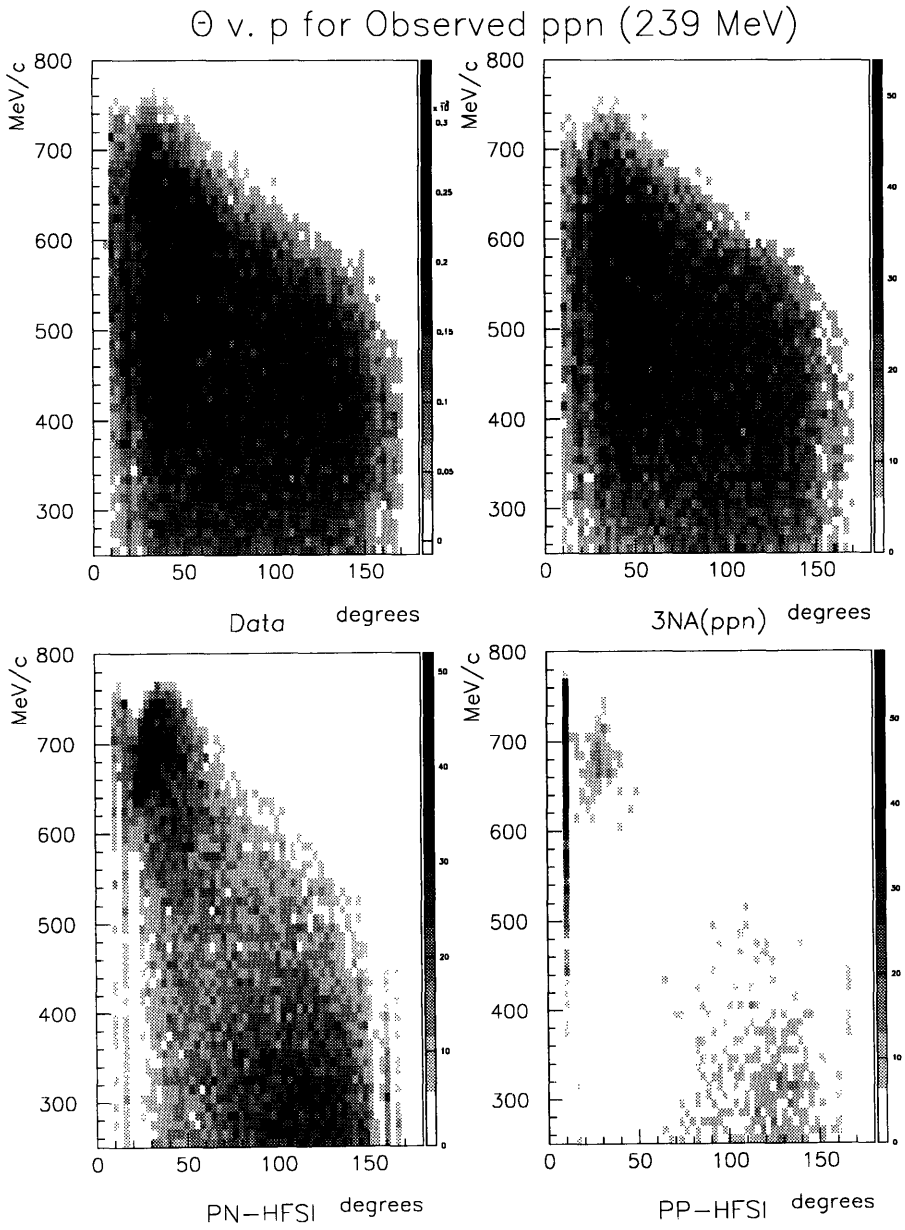

Figure 7-13: A comparison of the θ-momentum correlation for the three nucleons in the observed *ppp* channel at T_π = 239 MeV. The top left shows the data distribution, the top right the 3NA(*ppn*) distribution, the bottom right the PN-HFSI distribution, and the bottom left the PP-HFSI distribution.

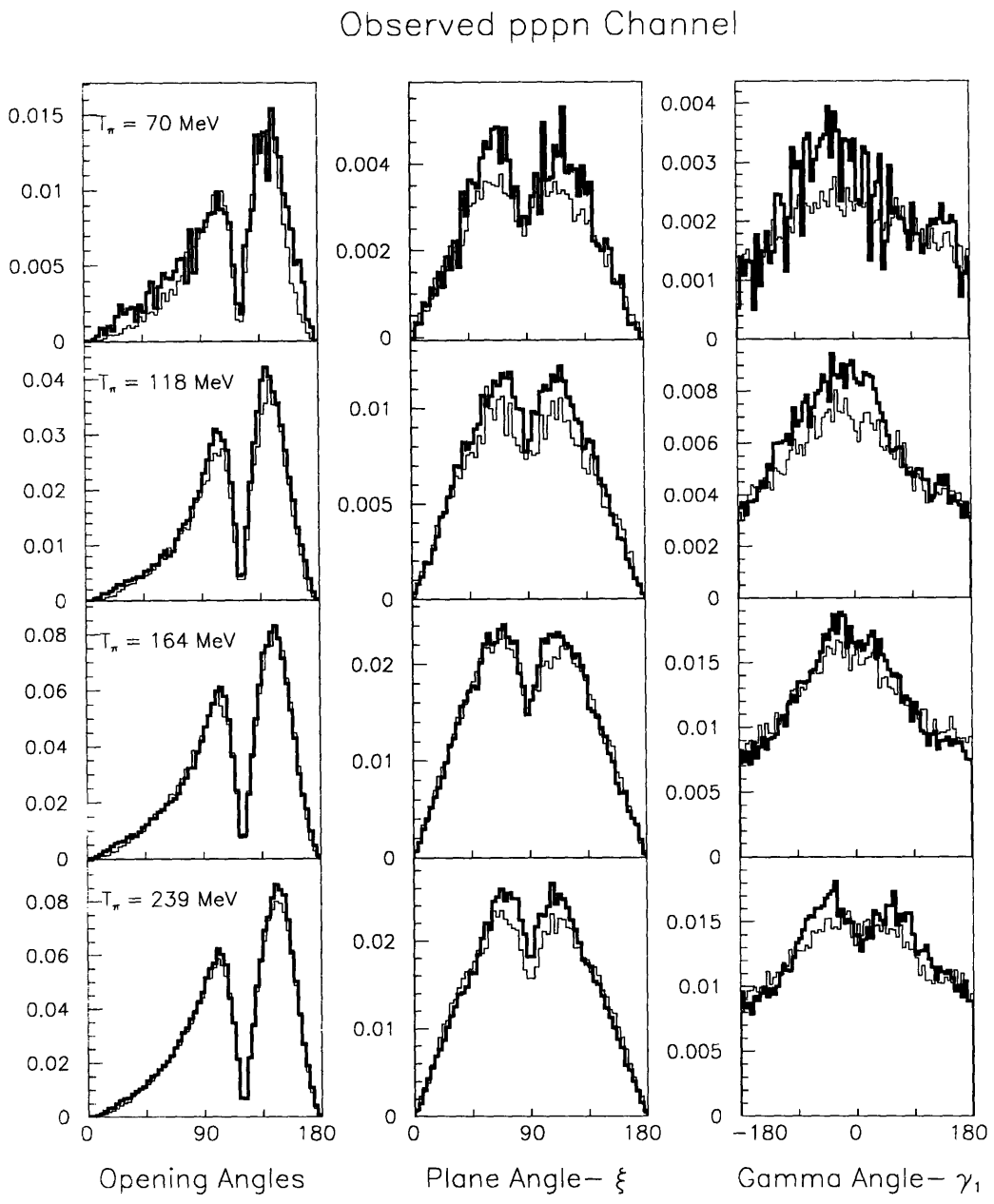

Figure 7-14: This figure shows four of the seven independent variables for a four-body system in the observed *pppn* channel. The first column contains the minimum and maximum opening angles. The second column shows the plane angle, and the last column the γ angle of the least energetic proton. In all cases, the dark solid line indicates the data distribution while the lighter solid line is the sum of the contributions from all Monte Carlo simulations.

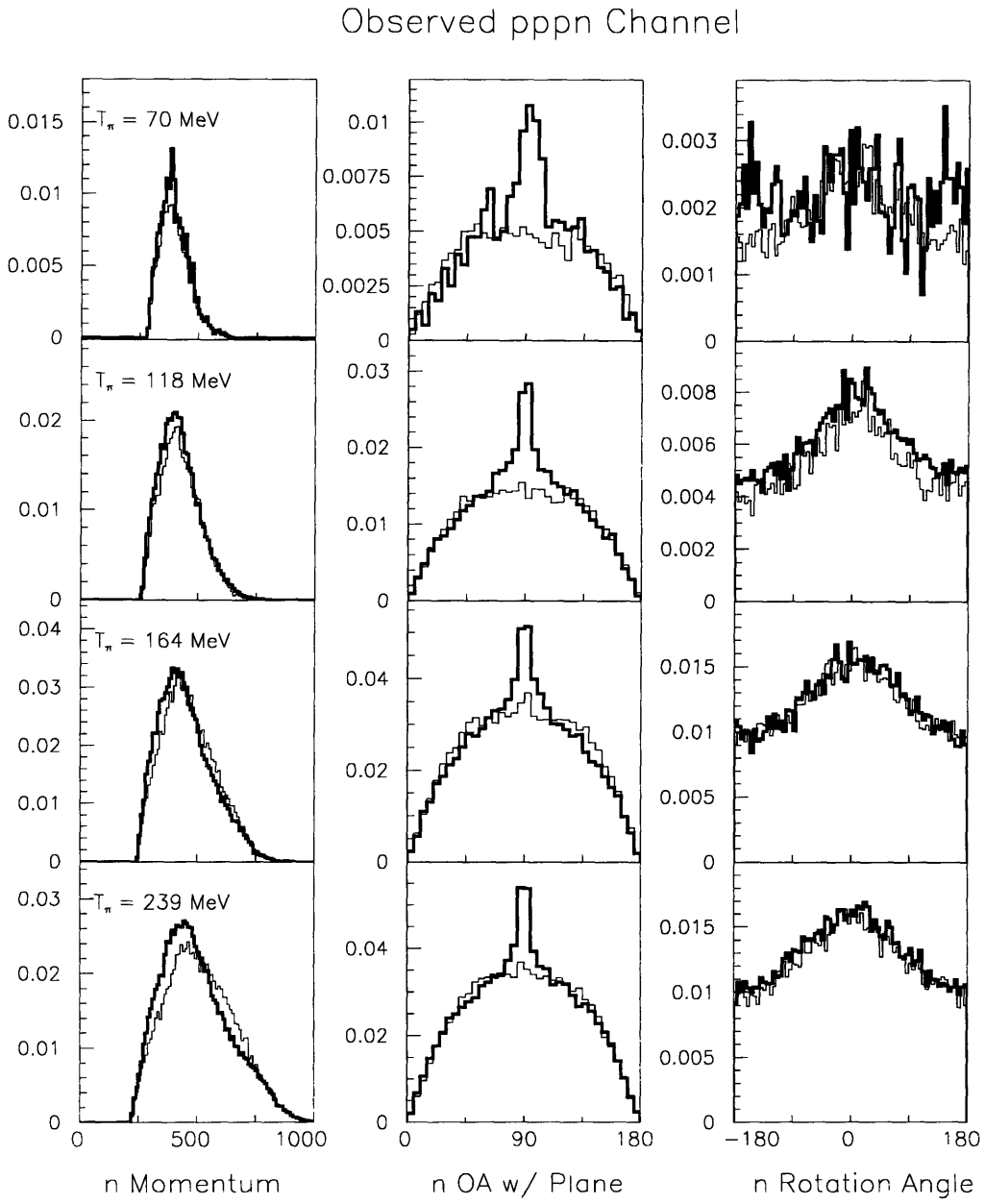

Figure 7-15: This figure shows three of the seven independent variables for the observed *pppn* channel. The first column shows the neutron momentum in the CM system of the other three particles, the second the opening angle between the normal of the plane and the neutron momentum vector, and the third the γ angle of the neutron momentum projection on the plane of the three protons. In all cases, the dark solid line indicates the data distribution while the lighter solid line is the sum of Monte Carlo contributions.

variables ξ, γ_1, and the pair correlations of the energies of the deuteron and the two protons ordered by energy are plotted for the data. In this case γ_1 refers to the γ angle of the least energetic of the two protons. Previously determined contributions from $(pp)d$ QDA and $(pd)p$ processes are subtracted from the data distribution and the resulting distributions are divided by the pure (ppd) phase space distributions.

The ξ angle distribution is fit as was described previously for the 3NA(ppp) generator. Once the plane angle has been modified, as described above, three independent variables remain. The ξ and γ_1 angles of the system are completely orthogonal to one another and to the energies of the particles. The energy distributions are orthogonal to ξ and γ_1 but are not independent of each other because of the total energy constraint of the system. The correlation between two of the energies is strictly speaking required to describe the energy dependence of the reaction correctly.

The γ_1 angle is also parametrized by a polynomial fit. For the energy correlations, not much variation is seen as a function of either the low or high proton energy. Hence, a one dimensional fit of the projection of the deuteron energy is a reasonable first order approximation of the energy correlation of the reaction. The fit functions derived for ξ, γ_1, and the deuteron energy are used to modify the weight of events from the (ppd) phase space generator. This new modified generator will be henceforth referred to as the M(ppd) generator.

The M(ppd) generator represents an improvement over the original phase space (ppd) distribution in terms of overall agreement with the data, but does not provide any insight into the mechanism behind the process. Figures 7-16 and 7-17 show the agreement obtained between data and Monte Carlo simulation in the energy and angular distributions of the protons and deuteron for the observed *ppd* channel using the M(ppd) generator.

The low energy forward peaked behavior of the deuterons in the observed *ppd* channel suggests that an ISI-type reaction may be occurring. A generator was created which simulated an intial scatter of the pion with a proton, and the subsequent pickup of a neutron by the scattered proton, and the absorption of the pion by the remaining *pn*-pair. This simulation was able to reproduce the low energy peaking observed in the deuteron energy distribution and also resulted in the deuteron being emitted preferentially forward. Figures 7-18 and 7-19 show the energy *vs.* θ distributions for the deuteron and the two protons for the observed *ppd* channel at 239 MeV. The M(ppd) generator, by construction, is the most similar to the data. The ISI simulation shows features which are qualitatively similar to the data. These plots suggests that an ISI-type process may be responsible for much of the strength of the observed *ppd* channel.

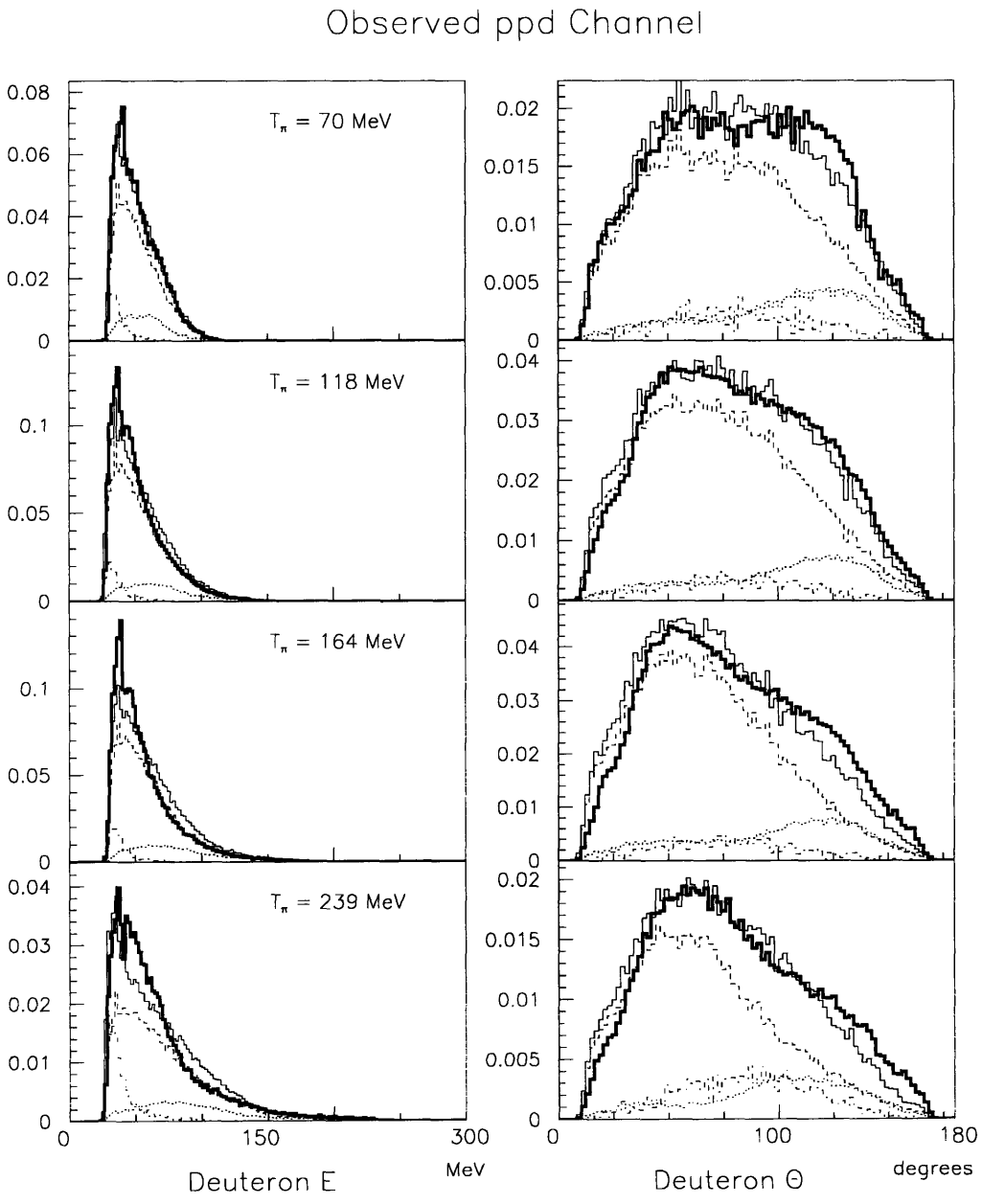

Figure 7-16: The LAB energy and θ distributions of the deuteron for the observed *ppd* channel. The dark solid line is the data, the lighter solid line is the simultaneous fit of Monte Carlo simulations. The dashed line is the assigned contribution from the (*pd*)*p* channel, the dotted line the assigned contribution from the M(*ppd*) channel, and the dash-dotted line the contribution from the (pp)d channel.

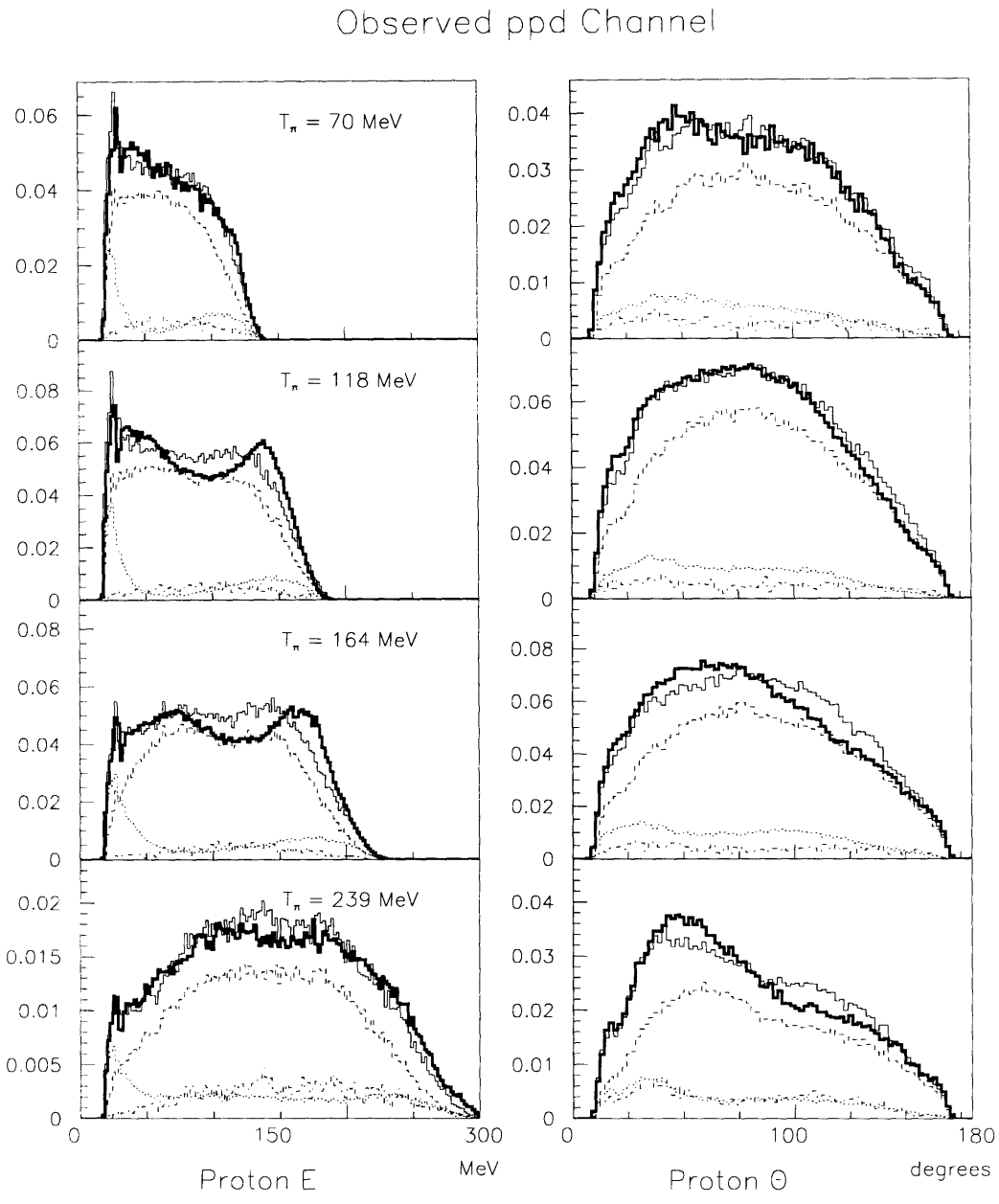

Figure 7-17: The LAB energy and θ distributions of the two protons for the observed *ppd* channel. The dark solid line is the data, the lighter solid line is the simultaneous fit of Monte Carlo simulations. The dashed line is the assigned contribution from the (*pd*)*p* channel, the dotted line the assigned contribution from the M(*ppd*) channel, and the dash-dotted line the contribution from the (pp)d channel.

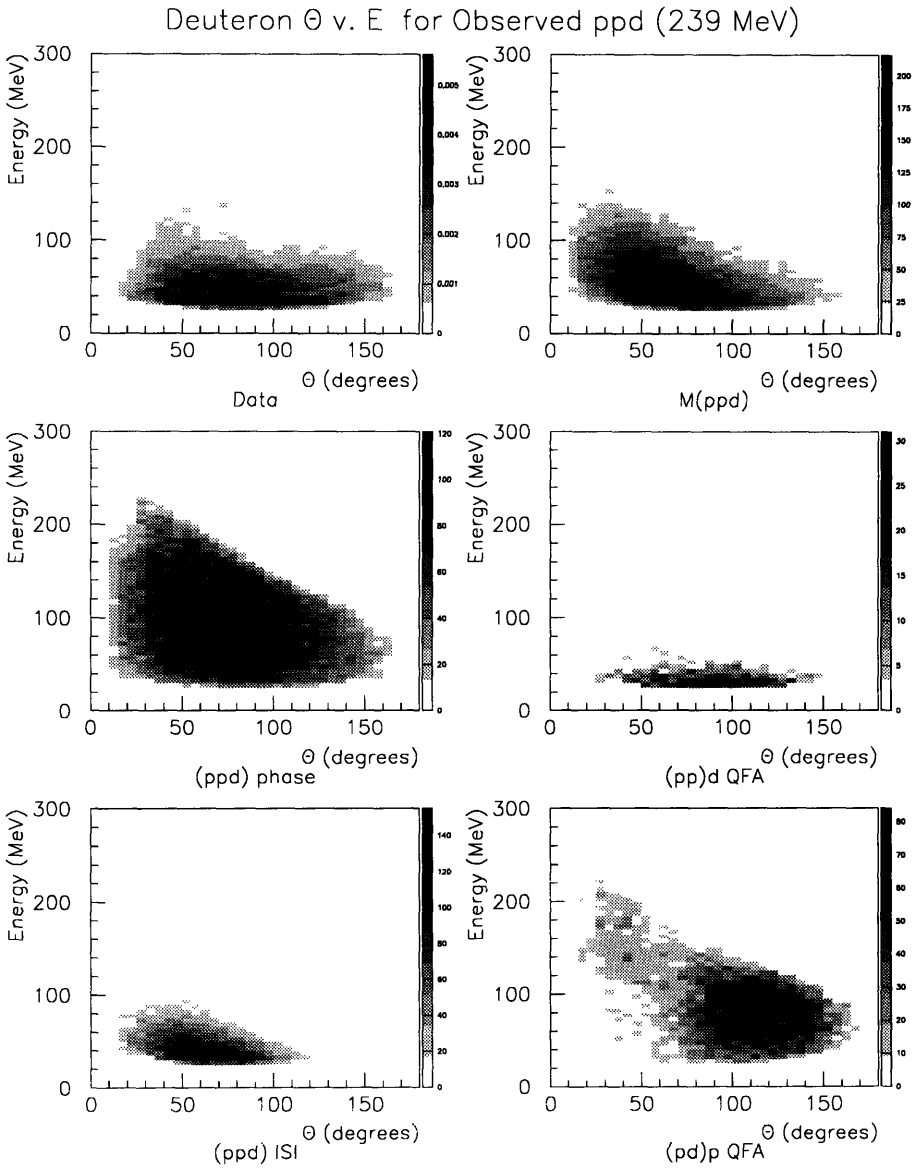

Figure 7-18: A comparison of the LAB E *vs.* θ distributions of the deuteron for the observed *ppd* channel for the data and various models for T_π = 239 MeV.

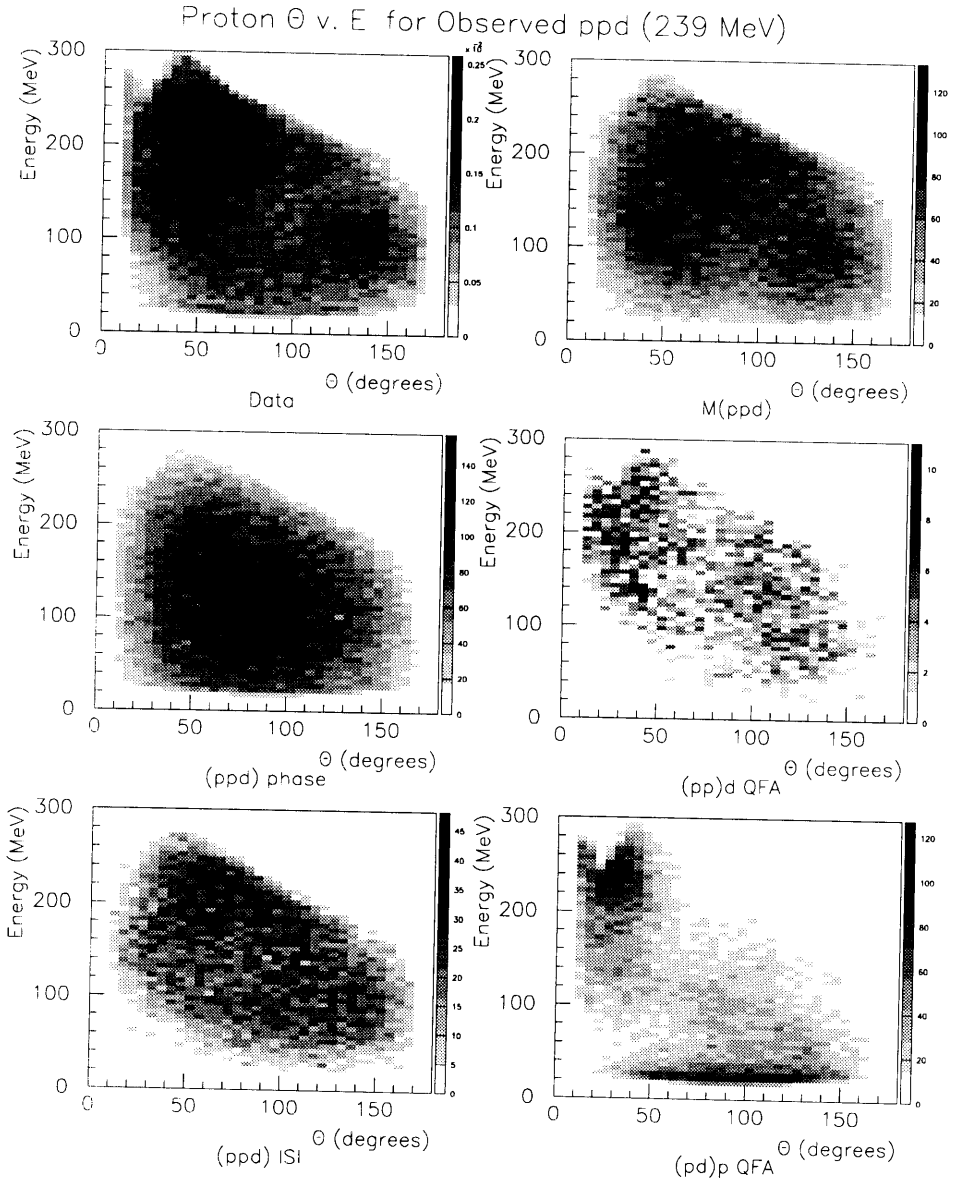

Figure 7-19: A comparison of the LAB E *vs.* θ distributions of the two protons for the observed *ppd* channel for the data and various models for $T_\pi = 239$ MeV.

Model	70 MeV	118 MeV	164 MeV	239 MeV
(pp)d/pn	19.6 ± 2.8	25.5 ± 1.8	22.9 ± 2.0	9.8 ± 0.7
PP-HFSI	1.6 ± 0.8	2.9 ± 2.0	0.7 ± 0.6	0.0
PN-HFSI	5.5 ± 3.1	10.4 ± 3.6	6.5 ± 3.0	1.7 ± 0.4
ISI	0.0	0.4 ± 0.4	0.6 ± 0.5	0.8 ± 0.2
(pd)p	2.5 ± 0.4	2.5 ± 0.2	2.1 ± 0.2	0.8 ± 0.1
M(ppd)	2.4 ± 0.4	4.3 ± 0.3	4.4 ± 0.4	1.6 ± 0.1
3NA(ppn)	0.8 ± 1.2	1.3 ± 1.9	3.9 ± 1.4	4.1 ± 0.3
3NA(ppp)	0.3 ± 0.4	0.6 ± 1.1	3.1 ± 0.8	3.0 ± 0.3
(pppn)	1.3 ± 0.4	1.9 ± 0.3	2.3 ± 0.2	2.1 ± 0.2
T=1 (est.)	0.6 ± 0.3	1.8 ± 0.9	1.6 ± 0.8	0.9 ± 0.4
Total	34.6 ± 5.5	51.7 ± 4.4	48.2± 4.4	24.8 ± 1.8

Table 7.2: Model dependent breakup of the total absorption cross section.

7.7 Model Dependent Breakup

In the simple physical channel breakup, the cross section was decomposed into seven competing channels. In the model dependent breakup, the three-body phase space simulations are replaced by the modified 3NA(*ppp*), 3NA(*ppn*), and M(*ppd*) distributions. Furthermore, an ISI process (ISI) and two hard FSI processes (PN-HFSI and PP-HFSI) are included in the breakup. For the 70 MeV fits, the ISI contribution was fixed to zero as one does not expect a contribution from this process at such a low energy. The results of the model dependent breakup are summarized in Table 7.2.

7.8 Comparison to INC Simulations

In order to determine whether new, coherent, multi-body processes are necessary to explain the strength of observed multi-particle final states one must have an idea of how much strength one should expect from conventional processes. The Intranuclear Cascade (INC) code which has been developed by Gibbs [52] can help answer this question. The INC constructs an initial state nucleus with protons and neutrons in different energy levels. It then fires a pion at the nucleus. Pion nucleus interactions are dealt with using known cross sections for the various free scattering reactions, and an absorption probability is specified to handle the disappearance of the pion.

	Ratio of Observed Channel to *pp*							
	(70 MeV)		(118 MeV)		(164 MeV)		(239 MeV)	
Observed Channel	DATA	INC	DATA	INC	DATA	INC	DATA	INC
pp	1.00	1.00	1.00	1.00	1.00	1.00	1.00	1.00
pd	0.11	0.06	0.07	0.04	0.05	0.03	0.02	0.02
ppd	0.08	0.07	0.11	0.09	0.12	0.09	0.17	0.10
ppp	0.05	0.04	0.07	0.06	0.14	0.11	0.32	0.19
pppn	0.01	0.01	0.02	0.01	0.05	0.04	0.18	0.10
ppn	0.04	0.04	0.07	0.06	0.10	0.09	0.20	0.13

Table 7.3: A comparison of the experimental and INC ratios of observed multi-nucleon cross sections to the observed *pp* cross section.

The nucleon-nucleon interactions are incorporated using the Malfleit-Tjon potentials. Although these are quantum mechanical potentials, they are used classically in the INC. The pion and the nucleons are propagated in small time intervals subject to the pion-nucleon interactions and the effects of the interactions of each individual nucleon with the potential created by the other nucleons. The only absorption mechanism contained in the INC is a two-body quasi-deuteron mechanism. All multi-nucleon effects are the result of either initial state interactions or distortions caused by nucleon-nucleon interactions.

The INC code produces files which are readable by the LADS Monte Carlo. Running the INC produced data files through the Monte Carlo produces an output file which is read by the analyzer, and identical cuts are applied to the data and the INC produced events.

A comparison of the ratio of the multi-nucleon observed channels to the *pp* observed channel is helpful in assessing whether conventional processes lead to enough strength in the multi-nucleon channels. The comparison of ratios of cross sections largely removes uncertainties involved in the normalization of either the data or the INC. Table 7.3 shows a comparison of the ratios of observed multi-nucleon channels to the *pp* observed channel. For all observed channels it appears that the INC predicted ratio is lower than the ratio observed in the data. For all channels except the observed *pd* channel, the closest agreement between INC ratios and the data ratios are obtained at the lowest energy. As the energy increases, the amount by which the INC underpredicts the observed multi-nucleon strengths appears to rise. This suggests that multi-nucleon channels which cannot be explained by conventional processes may be more important at higher incident pion energies.

Chapter 8

Discussion and Conclusions

8.1 Discussion of the total absorption cross section results

In the previous two chapters, the decomposition of the total absorption cross section into competing channels has been presented for ^{4}He at incident pion kinetic energies of 70, 118, 163 and 239 MeV. The total absorption cross sections have also been determined from the sum of these channels. The energy dependence of the total absorption cross section is displayed in Figure 8-1 along with data from previous measurements. The totals quoted here are those extracted from the simple breakup, with the uncertainties increased so that they overlap with the uncertainties obtained from the model dependent breakup. The result of this work at 118 MeV is in good agreement with the measurements of Steinacher *et al.* [56] and of Adimi [57]. It is substantially lower than the measurement of Baumgartner *et al.* [25]. The total cross sections measured here appear to be systematically lower than the estimates of Baumgartner *et al.*. In the Baumgartner *et al.* experiment, the inelastic pion cross section was measured and subtracted from the total cross sections measured by Binon *et al.* [69]. An estimate of the SCX cross section was made and subtracted from the total to obtain the absorption cross section. The SCX cross section has recently been measured by Wang at an incident pion energy of 160 MeV [90] to be roughly 5.5 mb higher than the estimated value used by Baumgartner *et al.* at 170 MeV. If the Baumgartner *et al.* SCX corrections are renormalized by the difference between the measured value of Wang and the SCX estimate, the Baumgartner *et al.* results, although still somewhat high, are in better agreement with the LADS measurement.

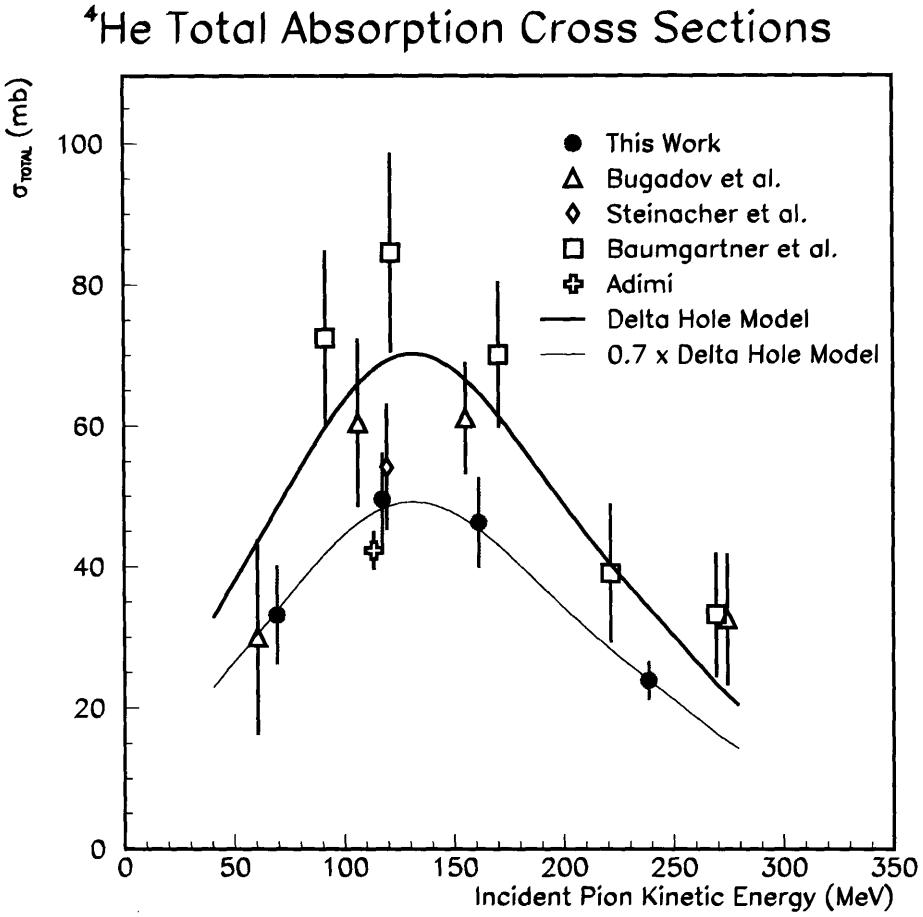

Figure 8-1: Measurements of the total absorption cross section on ^{4}He.

In Figure 8-2, the A dependence of the total absorption cross section at an incident pion kinetic energy of roughly 165 MeV is shown. It had been previously thought that the total absorption cross section increased dramatically from ^{3}He and ^{4}He, signaling the onset of a new absorption process available only in heavy nuclei. The LADS measurements indicate that the rise between ^{3}He and ^{4}He is less sharp than previously indicated. Measurements of total absorption cross sections have recently been performed by Rowntree [80] with the LADS detector on ^{14}N and ^{40}Ar. These measurements indicate that the normalization of the older experiment is roughly 25% too high. The power law of the rise in the cross section from ^{4}He to ^{14}N is $\sim A^{1.0}$, which is substantially steeper than the $\sim A^{.75}$ dependence which is characteristic of the total cross section for heavy nuclei. Such a dramatic rise is hard to understand if one believes that all absorption modes available in heavier nuclei are already open in ^{4}He. Accurate measurements of the total absorption cross section for nuclei with $4 > A > 14$ are clearly needed to make progress in understanding this steep rise.

8.2 Discussion of the breakup into channels

The primary goal of this thesis is to determine the character of the multi-nucleon final states following absorption of a pion. To that end, the cross section was decomposed in two different ways, the first was based on the number and types of participants and spectators in the reaction and the second on a model dependent breakup into channels which are believed to contribute to the cross section. By comparing the results of the two breakups an understanding of the systematics of the decomposition can be gained.

8.2.1 Undisturbed Quasideuteron Absorption

The first observation which can clearly be made is that the undisturbed QDA clearly accounts for the largest fraction of the total absorption cross section. Figure 8-3 shows the total absorption cross sections attributable to undisturbed QDA from the simple model breakup, along with the results from previous measurements.

In the simple model breakup, the percentage of the total absorption cross section attributable to undisturbed QDA falls steadily as a function of energy. The undisturbed QDA percentages of the total absorption cross sections in the simple breakup for 70 MeV, 118 MeV,

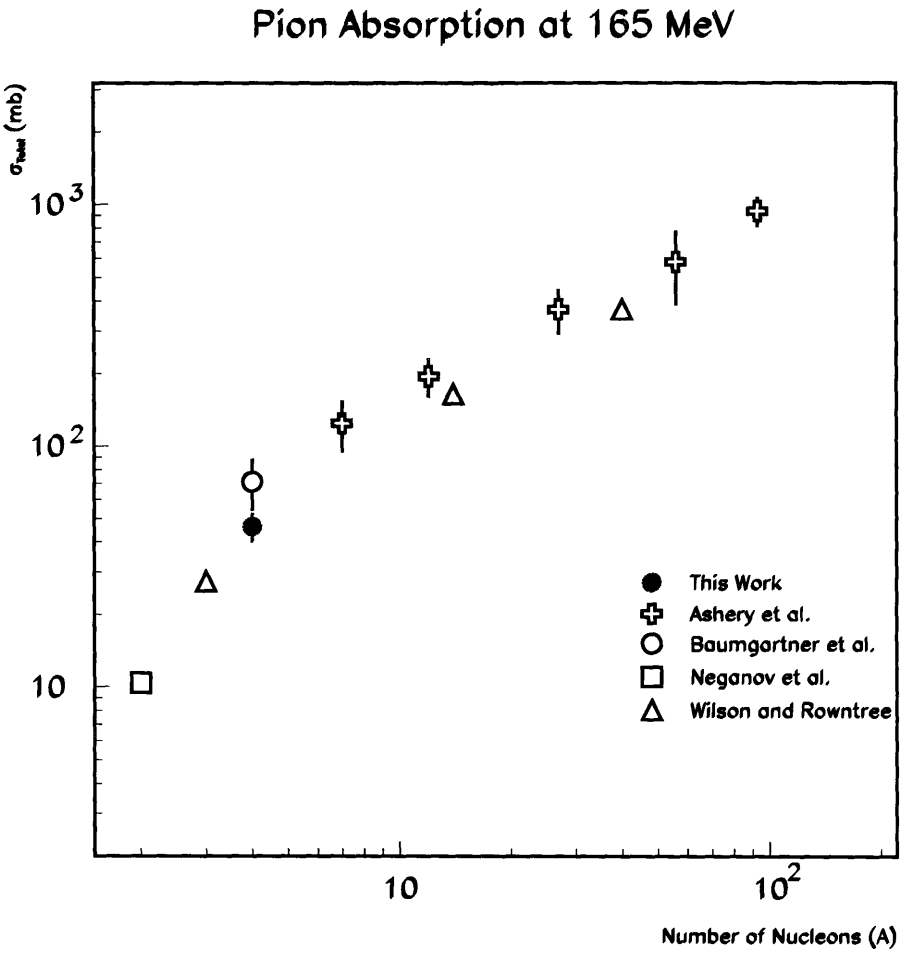

Figure 8-2: The A dependence of the total pion absorption cross section.

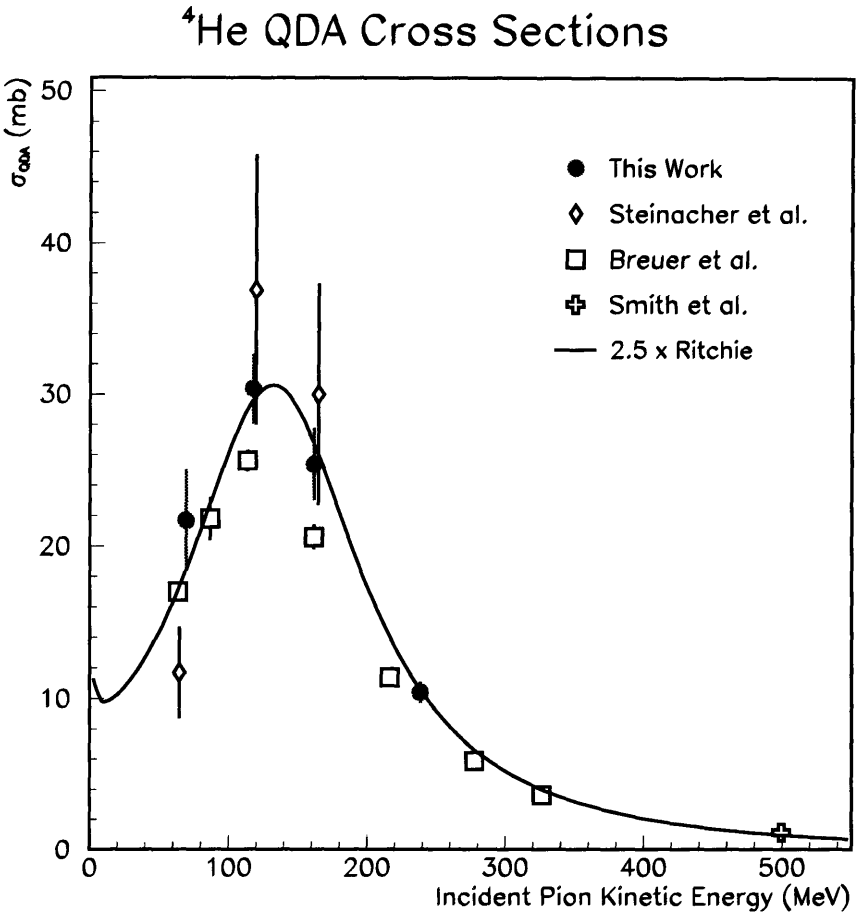

Figure 8-3: Measurements of the QDA strength in pion absorption on ^{4}He.

164 MeV, and 239 MeV are 66%, 61%, 55%, and 44%. In the model dependent breakup, the percentages for undisturbed QDA are systematically lower: 57%, 49%, 48% and 40%. This is attributable to the fact that some of the strength which was attributed in the simple breakup to undisturbed QDA was assigned in the model dependent breakup to two step processes, particularly the HFSI processes. One can conclude that the contribution of QDA to the total absorption cross section falls as a function of energy from roughly two-thirds below the resonance to less than one-half well above the resonance. The fraction of the total cross section which is undisturbed QDA has been measured previously at 114 MeV by Adimi [57], at 120 MeV by Steinacher *et al.* [56] and at a large number of energies by Breuer *et al.* [73]. Figure 8-4 shows a comparison of the measured ratios. It appears that the percentages obtained by Breuer *et al.* are somewhat lower than the current measurement. There are two reasons for this difference. The first is that the amount of undisturbed QDA measured by Breuer *et al.* is systematically lower than the present measurement. The second is that the total cross sections were not reported by Breuer *et al.*, and the previously reported, higher measurements of the total absorption cross section were used to determine the percentage of QDA.

The fall-off of the undisturbed QDA as a function of energy is consistent with absorption results obtained on heavier nuclei, which show a steady decrease as the incident energy rises. The percentage of QDA to the total cross section on ^{3}He appears to behave somewhat differently, as it does not appear to drop off significantly as a function of energy. For ^{3}He at 118 MeV, 164 MeV, and 239 MeV the fraction of QDA to the total absorption cross section has been measured by Wilson [26] to be 78%, 70% and 70%. The difference between ^{3}He and the heavier nuclei can be understood by the fact that in ^{3}He there is only one competing channel which can take absorption strength from the QDA channel, while already in ^{4}He there are many more channels. As the available energy increases in the heavier nuclei, the available phase space for other channels increases and hence more strength is drawn from the QDA channel.

The QDA cross section appears to be roughly 2.5 times the total absorption cross section on deuterium. This is substantially lower than the 3.0 expected from simple isospin scaling arguments. It also appears that the shape of the energy dependence of the QDA cross section is quite similar to the shape of the energy dependence of the absorption cross section on deuterium. This is because the average initial momentum of the absorbing pair is not large enough to substantially broaden the resonance.

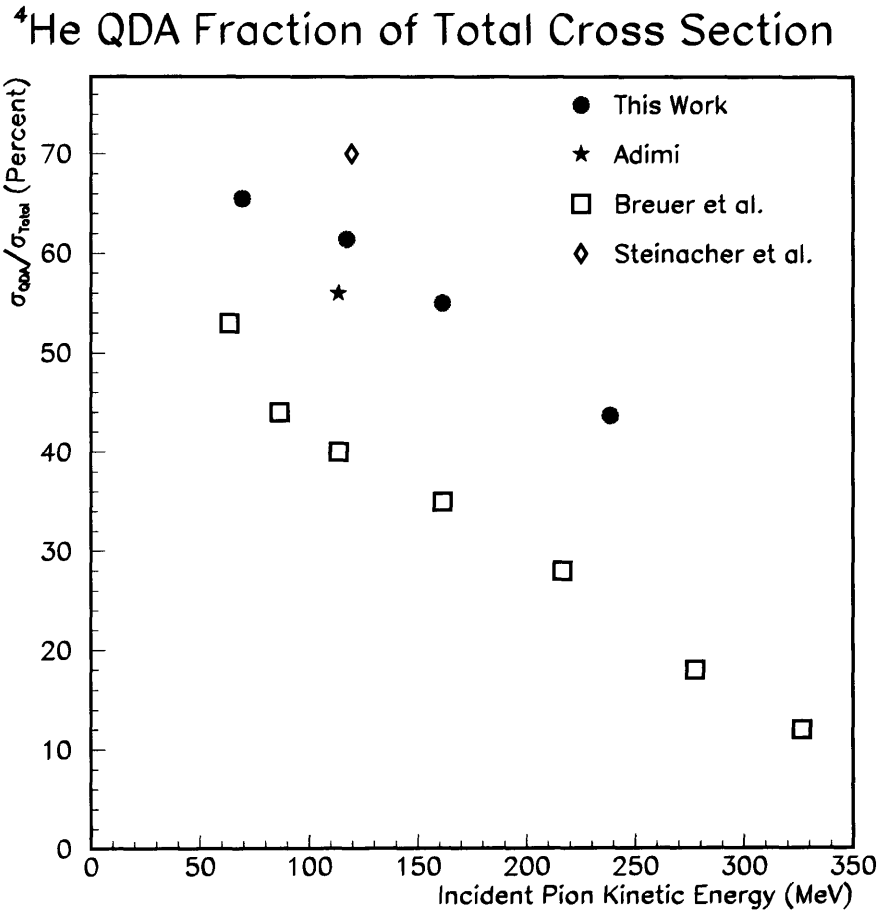

Figure 8-4: Measurements of the fraction of the total absorption cross section which is undisturbed QDA.

8.2.2 Non-QDA Absorption Processes

The non-QDA absorption processes can be subdivided into three-body *ppd* final states and four-body *pppn* final states. There have been two other measurements which have attempted to decompose the multi-nucleon absorption strength on ^{4}He. The amounts attributable to three-body *ppd* final states and four-body *pppn* final states were determined in the measurements of Adimi and Steinacher *et al.* They are shown in Figures 8-5 and 8-6 along with the current measurements for comparison.

Both the simple and model dependent breakups agree that the non-QDA *ppd* final state fraction of the total absorption cross section in ^{4}He falls slightly as a function of energy from roughly 14% at 70 MeV to roughly 8% at 239 MeV. In contrast, the non-QDA *pppn* final state contribution to the total absorption cross section shows a dramatic increase as a function of incident pion kinetic energy. In the simple breakup, the non-QDA *pppn* percentages of the total cross section at 70, 118, 164, and 239 MeV are 18%, 22%, 27% and 44%. In the model dependent breakup, the percentages are higher, at 27%, 34%, 35%, and 47%. Thus the amount of non-QDA *pppn* is a steadily increasing function of energy, and at the highest energy accounts for roughly the same amount of strength as the undisturbed QDA channels. It is also important to note that the non-QDA *pppn* final state is clearly resonating, but the peak of the cross section is shifted upward in comparison to the total cross section, presumably because of the larger phase space available for multi-nucleon processes at higher energies.

8.2.2.1 Deuteron Final States

The $(pd)p$ process, in which there is an energetic proton and an energetic deuteron in the final state is consistent with a two-step pickup type process. The first step of the reaction involves a quasi-deuteron absorption, and after the absorption, one of the outgoing protons picks up a spectator proton, forming a bound deuteron. The backward peaking of the deuteron angular distribution is consistent with pickup as the momentum mismatch between a spectator neutron and forward-going proton following absorption is much larger than between the spectator neutron and a backward-going proton. Hence, it is much easier for a backward-going proton to pick up a neutron than it is for a forward-going neutron. The magnitude of the $(pd)p$ cross section falls steadily with increasing incident pion energy, from roughly 8% of the total absorption cross section at 70 MeV to roughly 3% at 239 MeV, lending support to the assertion that this final state is the result of a two-step pickup process. It is this fall-off which is responsible for

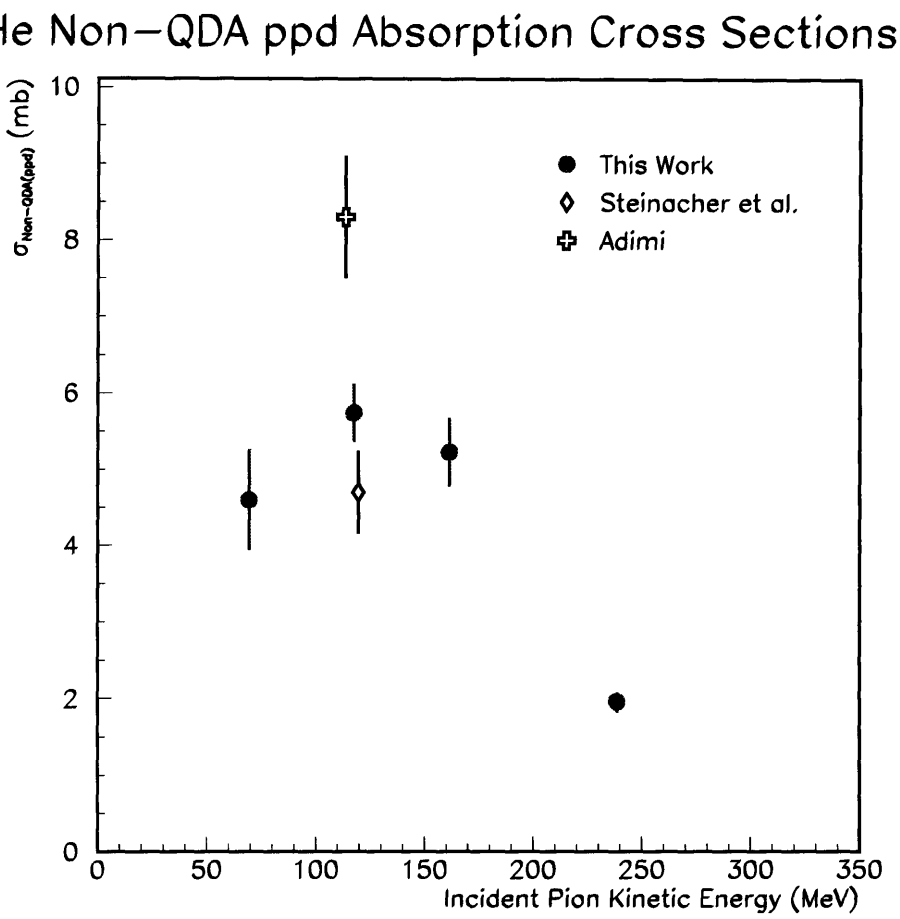

Figure 8-5: Measured energy dependence of the cross section attributable to non-QDA processes leading to the three-body final state *ppd*.

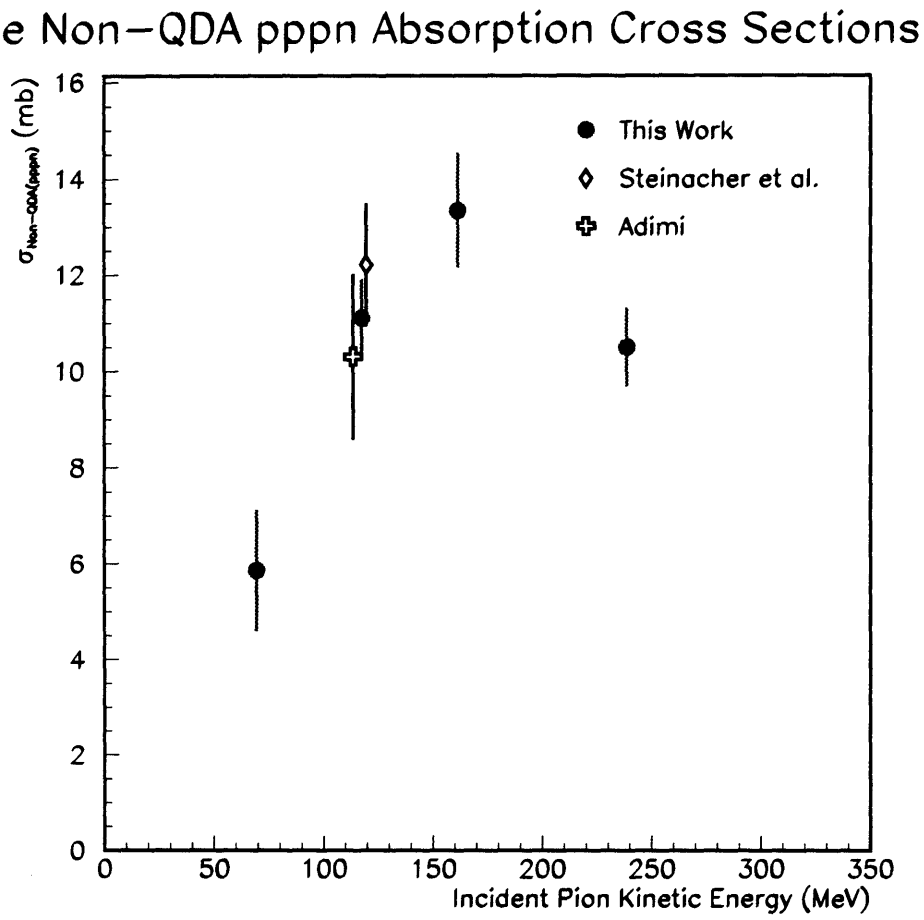

Figure 8-6: Measured energy dependence of the cross section attributable to non-QDA processes leading to the four-body final state *pppn*.

the small decrease in the non-QDA *ppd* percentage of the total absorption cross section as a function of incident pion energy.

The (*ppd*) process remains somewhat more enigmatic. The energy dependence of the cross section shows a broad resonance type behavior, peaking somewhere between 118 MeV and 164 MeV, and accounts for between 5% and 8% of the total absorption cross section. The deuteron energy spectrum is peaked toward lower energies than one would expect from a simple phase space distribution. This difference explains the differences in the extracted magnitudes of the (*ppd*) channel in the simple breakup and the M(*ppd*) value in the model dependent breakup. For the M(*ppd*) generator an attempt is made to model the low energy peaking of the deuteron whereas the (*ppd*) generator has only a simple phase space energy dependence for the deuteron.

The angular distribution of the deuterons appears to be forward peaked. This observation, along with the fact that the energies of the deuterons are rather low, suggests some sort of initial state interaction with a pickup of a neutron and a QDA absorption. The simulation of this process is able to describe the energy and angular spectrum of the final state deuterons but has more difficulty describing the proton distributions. Other possible explanations for the deuteron's energy spectrum being concentrated toward lower energies is that it is the result of an extended spectator momentum distribution, or that QDA absorption tends to pick out portions of the wave function in which the spectator has a high initial momentum. These arguments however are unable to explain the forward peaking of the deuteron angular distribution.

8.2.2.2 Multi-nucleon *pppn* final states

In the simple decomposition of the cross section, the *pppn* non-QDA absorption is divided into three physics channels (*ppp*)*n*, (*ppn*)*p*, and (*pppn*). The four-body (*pppn*) process appears to contribute roughly 2.1 mb to the total absorption cross section at the three higher incident pion kinetic energies. At the lowest energy there probably is not enough energy for the four-body process to contribute substantially. The non-resonance behavior suggests that the four-body absorption mechanism is statistical in nature and not associated with the formation of a Δ in the intermediate state. The smallness of the magnitude of the four-body absorption suggests that four-nucleon absorption mechanisms such as the double-Δ process are unimportant in ^{4}He.

The (*ppp*)*n* channel displays a resonance-like energy dependence, and is peaked at a somewhat higher incident pion kinetic energy than absorption on the deuteron. Its magnitudes at the four energies, 70 MeV, 118 MeV, 164 MeV, and 239 MeV were measured to be 1.2 mb, 2.2

mb, 3.8 mb, and 3.4 mb. The energy dependence of the $(ppp)n$ cross section does not have the same shape as the observed cross sections for this channel in ^{3}He, which have been measured by Wilson [26] at the three higher energies to be 6.0 mb, 7.2 mb, and 3.0 mb. While the cross sections for $(ppp)n$ are higher for ^{3}He than for ^{4}He at 118 MeV and 164 MeV, at the highest energy the cross section is larger for ^{4}He. This difference may be due to the fact that the energy dependence for competitive channels such as pickup processes is such that they tend to remove more strength from the $(ppp)n$ channel at lower energies than at higher energies. Thus, some of the strength of the $(ppp)n$ channel may be diverted into the competing (ppd) channel.

Of the three $pppn$ non-QDA channels, the $(ppn)p$ channel makes the largest contribution to the total absorption cross section. It appears to resonate somewhat strongly, and at an energy slightly lower than the $(ppp)n$ physics channel. The ratios of the $(ppn)p$ to the $(ppp)n$ channel for the energies 70 MeV, 118 MeV, 164 MeV, and 239 MeV are 3.0, 3.1, 2.0, and 1.5. An examination of the model dependent breakup is instructive in understanding the energy dependence of these ratios. In the model dependent breakup, at the lower energies, it appears that contributions from PN-HFSI are important. The PN-HFSI in the model dependent breakup would come mainly from the $(ppn)p$ channel in the simple breakup. As the incident energy rises, the cross section attributed to PN-HFSI falls. Furthermore, the ISI channel begins to contribute at 164 MeV in the model dependent breakup. The ISI channel comes mostly from the $(ppp)n$ channel in the simple breakup. Hence the relative strength of the $(ppp)n$ channel compared to the $(ppn)p$ channel rises as a function of incident pion energy.

8.3 Strength of Genuine Multi-Nucleon Processes

From the model dependent breakup, one may make an estimate of the strength of genuine multi-nucleon processes. The validity of this estimate is inherently limited by the classical nature of the models used to describe the two-step processes such as ISI and HFSI which have been used in the decomposition of the cross section. The ISI and HFSI contributions estimated by this decomposition may only be a part of the cross section, and some of the strength which has been designated as genuine may indeed be attributable to ISI and HFSI-like processes which could not be distinguished from the genuine mechanism for lack of a clear kinematic signature. Nevertheless, the model dependent breakup provides an estimate of the possible genuine multi-nucleon strength. For purposes of discussion, the genuine multi-nucleon strength is associated to the amount of cross section in the 3NA(ppp), 3NA(ppn), and $(pppn)$ channels.

The other *pppn* non-QDA channels are all two-step processes, one of which is a QDA vertex. The (*pd*)*p* and M(*ppd*) channels are also classified as non-genuine for this estimate. The (*pd*)*p* channel appears to be the result of a pickup, and the M(*ppd*) channel has a deuteron energy distribution which is strongly peaked at low energies suggesting that it is either the result of an extended fermi distribution or the result of an intial scatter followed by a pickup and a QDA. Under this definition, the percentages of the total absorption cross section coming from genuine multi-nucleon processes in ^{4}He are 7%, 7%, 19%, and 37% at 70 MeV, 118 MeV, 164 MeV, and 239 MeV. Thus it appears that there is a substantial fraction of the total absorption cross section which remains inexplicable in terms of conventional processes, and this fraction rises as a function of incident pion energy. This observation is corroborated by the inability of the INC calculations to produce enough multi-nucleon strength, particularly at higher incident pion energies.

Whether the strength of multi-nucleon final states following absorption can be explained solely by sequential processes such as ISI and FSI remains an open question. The answer to this question may be found only by a comparison of the measured absorption cross sections to realistic theoretical calculations.

Bibliography

[1] H. Yukawa. "On the Interaction of Elementary Particles," *Proc. Phys. Math. Soc. Japan*, **17**, 48 (1935).

[2] L. H. Ryder. *Quantum Field Theory.* Cambridge University Press, New York, 1985.

[3] M. Rho and D. H. Wilkinson, editors. *Mesons in Nuclei*, chapter 4. North-Holland Publishing Company, 1979.

[4] R. Machleidt, K. Holinde, and C. Elster. "The Bonn Meson-Exchange Model for Nucleon-Nucleon Interaction," *Physics Reports*, **149, No. 1**, 1–89 (1987).

[5] E. J. Moniz. Pion-Nucleus Scattering in the Isobar Formalism. In *Theoretical Methods In Medium-Energy and Heavy-Ion Physics*, pages 603–666. Plenum Press, New York, 1978.

[6] D. H. Perkins. *Introduction to High Energy Physics.* Addison-Wesley, Reading, MA, 1987.

[7] M. Gell-Mann and K. M. Watson. "The Interactions Between π-Mesons and Nucleons," *Annual Review of Nuclear Science*, **4**, 219–270 (1954).

[8] W. Panofsky, R. Aamodt, and J. Hadley. "The Gamma ray spectrum resulting from capture of Negative π-mesons in hydrogen and deuterium," *Physical Review*, **81**, 565 (1951).

[9] D. Ashery, I. Navon, G. Azuelos, H. Walter, H.J.Pfeiffer, and F.W.Schleputz. "True Absorption and scattering of pions on nuclei," *Physical Review*, **C23**, 2173–2185 (1981).

[10] C. H. Q. Ingram. "Pion-Nucleus Interactions," *Nuclear Physics*, **A374**, 319c–357 (1982).

[11] H. Feshbach. *Theoretical nuclear physics : nuclear reactions.* Wiley, New York, 1992.

[12] H. J. Weyer. "Pion absorption in light nuclei," *Physics Reports*, **195**, 295 (1990).

[13] T. Ericson and W. Weise. *Pions and nuclei.* Clarendon Press, Oxford, 1988.

[14] D. Ashery and J. P. Schiffer. "Pion Absorption in Nuclei," *Annual Review of Nuclear and Particle Science*, **36**, 207 (1986).

[15] A. Laptev and I. Strakovsky. *A Collection of Experimental Data for the pp → d Process.* Leningrad Nuclear Physics Institute, Leningrad, 1985.

[16] B. Ritchie. "Parameterization of the total cross section for $\pi d \rightarrow pp$ below 330 MeV," *Physical Review*, **C28**, 926–928 (1983).

[17] J. M. Eisenberg and D. S. Koltun. *Theory of Meson Interactions with Nuclei.* John Wiley and Sons, New York, 1980.

[18] J. A. Niskanen. "The Differential Cross Section and Polarization in p+p → d+π^+," *Nuclear Physics*, **A298**, 417 (1978).

[19] M. Betz and T.-S. H. Lee. "Phenomenological Hamiltonian for pions, nucleons, and Δ isobars: Apllications to the pion-deuteron system," *Physical Review*, **C23**, 375 (1981).

[20] B. Blankleider and I. Afnan. "Relationship between Partial Wave Amplitudes and Polarization Observables in pp → d π^+ and π d → π d," *Nuclear Physics*, **A298**, 499 (1978).

[21] J. Favier, T. Bressani, G. Charpak, L. Massonet, W. Weyerhof, and Č. Zupančić. "The $(\pi^+, 2p)$ reaction in light nuclei," *Nuclear Physics*, **A169**, 540–576 (1971).

[22] H. Jackson, S. Tabor, K. Rehm, J. Schiffer, R. Segel, J. L.L. Rutledge, and M. Yates. "Study of Pion-Absorption Mechanisms in ^{4}He and Other Nuclei," *Physical Review Letters*, **39**, 1601 (1977).

[23] H. Jackson, S. Kaufman, L. Meyer-Schutzmeister, J. Schiffer, S. Tabor, S. Vigdor, J. Worthington, J. L.L. Rutledge, R. Segel, R. Burman, P. Gram, R. Redwine, and M. Yates. "Energetic Charged Particle Yields Induced by Pions on Complex Nuclei," *Physical Review*, **C16**, 730 (1977).

[24] R. McKeown, S. Sanders, J. Schiffer, H. Jackson, M. Paul, J. Specht, E. Stephenson, R. Redwine, and R. Segel. "How many nucleons are involved in pion absorption in nuclei?," *Physical Review Letters*, **44**, 1033–1036 (1980).

[25] M. Baumgartner, H. Gubler, G. Plattner, W. Ramsay, H. Roser, I. Sick, P. Zupranski, J. Egger, and M. Thies. "Inclusive π^4He scattering and the πN interaction in the nuclear medium," *Nuclear Physics*, **A399**, 451–477 (1983).

[26] K. E. Wilson. *Pion Absorption on ^3He.* PhD thesis, Massachusetts Institute of Technology, February 1995.

[27] B. Neganov and L. Parfenov. "Investigation of the $\pi^+ + d \rightarrow 2p$ reaction for 174-307 MeV π^+ mesons," *JETP Sov. Phys.*, **7**, 528 (1958).

[28] D. Gotta, M. Dorr, W. Fetscher, G. Schmidt, H. Ullrich, G. Backenstoss, W. Kowald, I. Schwanner, and H.-J. Weyer. "Kinematically Complete Measurement of the Absorption of Stopped Pions in ^{3}He," *Physics Letters*, **112B**, 129 (1982).

[29] D. Ashery, R. Holt, H. Jackson, J. Schiffer, J. Specht, and K. Stephenson. "Isospin Dependence of Pion Absorption on a Pair of Nucleons," *Physical Review Letters*, **47**, 895 (1981).

[30] G. Backenstoss, M. Izycki, M. Steinacher, P. Weber, H.-J. Weyer, K. V. Weymarn, S. Cierjacks, S. Ljungfelt, U. Mankin, T. Petkovic, G. Schmidt, H. Ullrich, and M. Furic. "Isospin Dependence of Pion Absorption on Nucleon Pairs in 3He," *Physics Letters*, **B222**, 7 (1989).

[31] M. Moinester, D. Gill, J. Vincent, D. Ashery, S. Levenson, J. Alster, A. Altman, J. Lichtenstadt, E. Piasetzky, K. Aniol, R. Johnson, H. Roser, R. Tacik, W. Gyles, B. Barnett, R. Sobie, and H. Gubler. "Isospin Dependence of Pion Absorption on Nucleon Pairs at $T(\pi) = 65$ MeV," *Physical Review Letters*, **52**, 1203 (1984).

[32] A. Altman, D. Ashery, E. Piasetzky, J. Lichtenstadt, A. Yavin, W. Bertl, L. Felawka, H. Walter, R. Powers, R. Winter, and J. Pluym. "Isotopic Effects in the ($pi^{\pm}$,2N) Reactions on ^{1}6O and ^{1}8O," *Physics Letters*, **144B**, 337 (1984).

[33] A. Altman, D. Ashery, E. Piasetzky, J. Lichtenstadt, A. Yavin, W. Bertl, L. Felawka, H. Walter, R. Powers, R. Winter, and J. Pluym. "($\pi^{\pm}$,2N) Reactions at 165 and 245 MeV," *Phys. Rev.*, **C34**, 1757 (1986).

[34] W. J. Burger. *An Experimental Study of Pion Absorption in ^{58}Ni at $T_\pi = 160$ MeV.* PhD thesis, Massachusetts Institute of Technology, June 1985.

[35] W. Burger, E. Beise, S. Gilad, R. Redwine, P. Roos, N. Chant, H. Breuer, G. Ciangaru, J. Silk, G. Blanpied, B. Preedom, B. Ritchie, M. Blecher, K. Gotow, D. Lee, and H. Ziock. "Reaction ^{58}Ni($\pi^+, 2p$) at 160 MeV," *Physical Review Letters*, **57**, 58–61 (1986).

[36] W. Burger, E. Beise, S. Gilad, R. Redwine, P. Roos, N. Chant, H. Breuer, G. Ciangaru, J. Silk, G. Blanpied, B. Preedom, B. Ritchie, M. Blecher, K. Gotow, D. Lee, and H. Ziock. "Reaction ^{58}Ni(π^+, pp) at $T_{\pi+} = 160$ MeV," *Physical Review*, **C41**, 2215–2228 (1990).

[37] R. Schumacher, P. Amaudruz, C. Ingram, U. Sennhauser, H. Breuer, N. Chant, A. Feldman, B. Flanders, F. Khazaie, D. Mack, P. Roos, J. Silk, and G. Kyle. "Exclusive Quasi-Deuteron Absorption of Pions in ^{16}O and ^{1}8O at 116 MeV," *Physical Review*, **C38**, 2205 (1988).

[38] S. Hyman, D. Mack, H. Breuer, N. Chant, F. Khazaie, B. Ritchie, P. Roos, J. Silk, P.-A. Amaudruz, Th.S.Bauer, C.H.Q.Ingram, G. Kyle, D. Renker, R. Schumacher, U. Sennhauser, and W. Burger. "$^{16}O(\pi^+, 2p)$ reaction at 165 MeV," *Physical Review*, **C41**, R409–413 (1990).

[39] D. Mack, P. Roos, H. Breuer, N. Chant, S. Hyman, F. Khazaie, B. Ritchie, J. Silk, G. Kyle, P. Amaudruz, T. Bauer, C. Ingram, D. Renker, R. Schumacher, U. Sennhauser, and W. Burger. "Dominance of the Two-Nucleon Mechanism in 16O(π,pp) at 115 MeV," *Physical Review*, **C45**, 1767 (1992).

[40] R. Ransome, C. Morris, V. Cupps, R. Fergerson, J. McGill, D. Watson, J. Zumbro, B. Ritchie, J. Comfort, J. Tinsley, R. Loveman, S. Dawson, A. Green, P. Gugelot, and C. Moore. "Pion Absorption in Heavy Nuclei," *Physical Review*, **C45**, R509 (1992).

[41] R. Ransome, C. Morris, M. Jones, B. Ritchie, D. Watson, J. McGill, K. Pujara, D. Clayton, I. Brown, P. Campbell, and C. F. Moore. "Pion Absorption in Light Nuclei," *Physical Review*, **C46**, 273 (1992).

[42] G. Harp, K. Chen, G. Friedlander, Z. Fraenkel, and J. Miller. "Intranuclear Cascade Studies of Low-Energy Pion-Induced Nuclear Reactions; Possible Effects of the Finite Lifetime of the (3,3) Isobar," *Physical Review*, **C8**, 581 (1973).

[43] J. N. Ginocchio. "Deep Inelastic Pion-Induced Nuclear Reactions in the Isobar Model," *Physical Review*, **C17**, 195 (1978).

[44] Z. Fraenkel, E. Piasetzky, and G. Kalbermann. "Intranuclear Cascade Calculation of Pion-Nucleus Reactions in the Resonance Region," *Physical Review*, **C26**, 1618 (1982).

[45] J. Hufner and M. Thies. "Pion-Nucleus Scattering and Absorption as a Solution of the Boltzmann Equation," *Physical Review*, **20**, 273 (1979).

[46] J. N. Ginocchio and M. B. Johnson. "Effect of the Pion and DELTA Optical Potential on Deep Inelastic Pion-Nuclear Reactions," *Physical Review*, **C21**, 1056 (1980).

[47] K. Masutani and K. Yazaki. "The pion optical potential and its application to reaction processes," *Nuclear Physics*, **A407**, 309–348 (1983).

[48] Y. Horikawa, M. Thies, and F. Lenz. "The Δ-Nucleus spin-orbit interaction in π-nucleus scattering," *Nuclear Physics*, **A345**, 386–408 (1980).

[49] M. Hirata, F. Lenz, and M. Thies. "Delta-nucleon and pion-nucleus interactions," *Physical Review*, **C28**, 785–810 (1983).

[50] K. Ohta, M. Thies, and T.-S. H. Lee. "Study of the two-nucleon mechanism of pion absorption in nuclei," *Annals of Physics*, **163**, 420–472 (1985).

[51] R. Redwine. "Pion-Induced Nuclear Reactions," *Talk at INS International Symposium on Nuclear Physics at Intermediate Energy, Tokyo* (1988).

[52] W. R. Gibbs. The Intranuclear Cascade. Unpublished, 1994.

[53] M. Thies. "Pion Absorption in Nuclei," *Lecture at Les Houches Winter School on Nuclear Matter and Heavy Ion Collisions* (1989).

[54] F. Lenz. "Strong interaction studies via meson-nucleus reactions," *Progress of Theoretical Physics Supplement*, **91**, 27–59 (1987).

[55] M. Thies. "Pion Nucleus Interactions," *Talk at Twenty-First LAMPF Users Meeting* (1987).

[56] M. Steinacher, G. Backenstoss, M. Izycki, P. Salvisberg, P. Weber, H. Weyer, A. Hoffart, B. Rzehorz, H. Ullrich, M. Džemidžic, M. Furić, and T. Petković. "Pion absorption in flight on ^{4}He," *Nuclear Physics*, **A517**, 413 (1990).

[57] F. Adimi. *Pion Absorption on ^{4}He at 114 MeV.* PhD thesis, University of Maryland, May 1994.

[58] L. Salcedo, E. Oset, and D. Strottman. "Experimental test of three-body pion absorption," *Physics Letters*, **B208**, 339 (1988).

[59] H. Weyer. "Signatures in Pion Absorption," *Talk at International Workshop on Pions in Nuclei, Peniscola* (1991).

[60] T.-S. H. Lee. "Mechanism of ^{3}He(π, pn) reaction," *Physical Review*, **C31**, 2163 (1985).

[61] T. Alteholz, D. Androic, G. Backenstoss, D. Bosnar, H. Breuer, A. Brkovic, H. Dobbeling, T. Dooling, W. Fong, M. Furic, P. Gram, N. Gregory, J. Haas, A. Hoffart, C. Ingram, A. Klein, K. Koch, J. Kohler, B. Kotlinski, M. Kroedel, G. Kyle, A. Lehmann, Z. Lin, G. Mahl, A. Mateos, K. Michaelian, S. Mukhopadhyay, T. Petkovic, R. Redwine, D. Rowntree, R. Schumacher, U. Sennhauser, N. Simicevic, F. Smit, G. van der Steenhoven, D. Tieger, R. Trezeciak, H. Ullrich, M. Wang, M. Wang, H. Weyer, M. Wildi, and K. Wilson. "A Large Solid Angle Study of Pion Absorption in ^{3}He," *Physical Review Letters*, pages 1334–1339 (1994).

[62] L. C. Smith, R. C. Minehart, D. Ashery, E. Piasetsky, M. Moinester, I. Navon, D. Geesaman, J. P. Schiffer, G. Stephans, B. Zeidman, S. Levenson, S. Mukhopadhyay, R. E. Segel, B. Anderson, R. Madey, J. Watson, and R. R. Whitney. "Reaction ^{3}He$(\pi^+, pp)p$ at $T_\pi = 350$ and 500 MeV," *Physical Review*, **C4O**, 1347 (1989).

[63] S. Mukhopadhyay, S. Levenson, R. E. Segel, G. Garino, D. Geesaman, , J. P. Schiffer, G. Stephans, B. Zeidman, E. Ungricht, H. Jackson, R. Kowalczyk, D. Ashery, E. Piasetsky, M. Moinester, I. Navon, L. C. Smith, R. C. Minehart, G. S. Das, R. R. Whitney, R. Mckeown, B. Anderson, R. Madey, and J. Watson. "Pion absorption by ^{3}He at the Δ-resonance energy," *Physical Review*, **C43**, 957 (1991).

[64] K. Aniol, A. Altman, R. Johnson, H. Roser, R. Tacik, U. Wienands, D. Ashery, J. Alster, M. Moinester, E. Piasetzky, D. Gill, and J. Vincent. "Pion absorption on ^{3}He at $T_\pi = 62.5$ and 82.8 MeV," *Physical Review*, **C33**, 1714 (1986).

[65] P. Weber, G. Backenstoss, M. Izycki, R. Powers, P. Salvisberg, M. Steinacher, H. Weyer, S. Cierjacks, A. Hoffart, B. Rzehorz, H. Ullrich, D. Bosnar, M. Furić, T. Petković, and N. Šimičević. "Three-nucleon processes and the total pion absorption cross section in ^{3}He," *Nuclear Physics*, **A534**, 541 (1991).

[66] E. Fowler, W. Fowler, R. Shutt, A. Thorndike, and W. Whittemore. "A diffusion cloud-chamber study of pion interactions in hydrogen and helium," *Physical Review*, **91**, 135–149 (1953).

[67] Y. A. Budagov, R. Ermolov, E. Kushnirenko, and V. Moskalev. "Interaction between 153-MeV Negative Pions and Helium," *Soviet Physics JETP*, **15**, 824–836 (1962).

[68] M. Kozodaev, M. Kulyukin, R. Sulyaev, A. Filippov, and Y. A. Schcherbakov. "Inelastic interactions of pions with helium nuclei at approximately 300 MeV," *Soviet Physics JETP*, **11**, 300–310 (1960).

[69] F. Binon, P. Duteil, M. Gouanere, L. Hugon, J. Jansen, J. Lagnaux, H. Palevsky, J.-P. Peigneux, M. Spighel, and J.-P. Stroot. "Scattering of Negative Pions on Helium," *Nuclear Physics*, **A298**, 499 (1978).

[70] P. Weber, J. McAlister, R. Olszewski, A. Feltham, M. Hanna, R. Johnson, M. Pavan, C. Ponting, F. Rozon, M. Sevior, V. Sossi, D. Vetterli, D. Humphrey, G. Lolos, Z. Papandreou, R. Tacik, D. Ottewell, G. Sheffer, G. Smith, Y. Mardor, and S. May-Tal. "Multinucleon pion absorption in the ^{4}He$(\pi^+, ppp)n$ reaction," *Physical Review*, **C43**, 1553 (1991).

[71] L. Smith, R. Minehart, O. Baker, D. Day, K. Giovanetti, R. Lourie, R. Marshall, B. Milbrath, B. Ritchie, R. Sealock, D. Tedeschi, and S. Thornton. "Pion Absorption in ^{4}He$(\pi^+, pp)p$ Above the Delta Resonance," *Physical Review*, **C48**, R485 (1993).

[72] F. Adimi, H. Breuer, B. Flanders, M. Khandaker, M. Khayat, P. Roos, D. Zhang, T. Bauer, J. Konijn, C. de Laat, G. Kyle, S. Mukhopadhyay, M. Wang, and R. Tacik. "Two nucleon absorption of π^+ in ^{4}He at T_π = 114 and 162 MeV," *Physical Review*, **C45**, 2589 (1992).

[73] H. Breuer, M. Khayat, F. Adimi, B. Flanders, M. Khandaker, P. Roos, D. Zhang, T. Bauer, J. Konijn, C. de Laat, G. Kyle, S. Mukhopadhyay, M. Wang, and R. Tacik. "Excitation function for ^{4}He$(\pi^+, \mathrm{pp})^2$H two-nucleon absorption across the Δ resonance," *Physical Review*, **C49**, R2276 (1994).

[74] E. Oset, Y. Futami, and H. Toki. "Pion Absorption in the Resonance Region," *Nuclear Physics*, **A448**, 597–636 (1986).

[75] G. Brown, H. Toki, W. Weise, and A. Wirzba. "Double-$\Delta(1232)$ formation in pion-nucleus absorption," *Physics Letters*, **B118**, 39 (1982).

[76] A. Mateos and N. Simicevic. "Effect of Isospin on Three Nucleon Pion Absorption in Light Nuclei," *Physical Review*, **C47**, R1842 (1993).

[77] N. Simicevic. "Statistical Model of Three Nucleon Pion Absorption," *Physical Review*, **C50**, 224 (1994).

[78] N. Simicevic and A. Mateos. "Angular Distributions following three-nucleon pion absorption," *Physical Review*, **C51**, 797 (1995).

[79] A Large Solid Angle Detector for Studies of Pion Absorption. In preparation.

[80] D. C. Rowntree. *The A-Dependence of Pion Absorption in the Energy Region of the $\Delta(1232)$ Resonance.* PhD thesis, Massachusetts Institute of Technology, June 1995.

[81] J. Albanese, J. Arvieux, E. Boschitz, R. Corfu, J. Egger, P. Gretillat, C. Ingram, C. Lunke, E. Pedroni, C. Perrin, J. Piffaretti, L. Pflug, E. Schwarz, C. Wiedner, and J. Zichy. "The SIN high resolution pion channel and spectrometer," *Nuclear Instruments and Methods*, **158**, 363 (1978).

[82] Swiss Institute of Nuclear Science. *SIN Users Handbook 1981*, 1981.

[83] Dornier Ltd., P.O. Box 1420, D-88039 Friedrichshafen, Germany.

[84] N. Gregory. *Pion Single Charge Exchange on the Deuteron.* MSc thesis, Massachusetts Institute of Technology, in preparation.

[85] Bicron Corporation, 12345 Kinsman Road, Newbury, Ohio 44065, USA.

[86] Lecroy Corporation, 700 Chestnut Ridge Road, Chestnut Ridge, New York 10977, USA.

[87] GEANT, Detector Description and Simulation Tool. CERN Program Library Long Writeup W5013.

[88] L'Air liquide (Firm). *Encyclopedie des Gaz*, pages 6–7, 799–800, 992 and 999. Elsevier, Amsterdam and New York, 1976.

[89] B. Ritchie. "Parameterization of the total and differential cross sections for $\pi d \rightarrow pp$ below 1 GeV," *Physical Review*, **C49**, 533–536 (1991).

[90] M. Y. Wang. *Inclusive Pion Single Charge Exchange in ^{4}He in the Δ-Resonance Region.* PhD thesis, Massachusetts Institute of Technology, August 1994.